Evaluation of the Hydro-Thermodynamic Soil Vegetation Scheme and implementation of a new numerical scheme

A

THESIS

Presented to the Faculty of the University of Alaska Fairbanks

in Partial Fulfillment of the Requirements

for the Degree of

Master of Science

By

Balachandrudu Narapusetty, M.S.

Fairbanks, Alaska

August 2005

Abstract

The Hydro-Thermodynamic Soil-Vegetation Scheme (HTSVS) coupled in a two-way mode with the PennState/National Center for Atmospheric Research (NCAR) Mesoscale Meteorological Model generation 5 (MM5), has been subjected to evaluation for a 5 day typical snow-melt period using BALTic sea Experiment Meteorological Data Centre's soil temperature, snow depth, and precipitation datasets. The HTSVS-MM5 evaluation investigates the coupled system's sensitivity to two cloud models and two radiation models with their cross effects presented along with skill scores for snow depth changes. It satisfactorily predicts the soil temperature diurnal course cycles, changes in the snow depths, accumulated precipitations.

HTSVS's soil model has been further tested and evaluated in an offline mode for the advanced numerical treatment for the Partial Differential Equations (PDEs) using soil temperature datasets from three sites at Council, Alaska. Galerkin Weak Finite Element (GWFE) method is used to test and evaluate for the numerical treatment of PDEs and compared the predictions against the existing Crank-Nicholson finite differences (CNFD) scheme. GWFE solutions exhibit a remarkable soil temperature predictability, better capture the temperature peaks, non-diffuse and non-oscillatory solutions for relatively high convection regimes, while CNFD performs comparably well in the diffusion dominated regimes with lower computational burden.

Table of Contents

Abstract iii

Table of Contents iv

List of Figures vii

List of tables ix

Introduction 10

REFERENCES 17

Chapter 1 24

Evaluation of snow depth and soil temperatures predicted by the Hydro- Thermodynamic Soil-Vegetation Scheme (HTSVS) coupled with the PennState/NCAR Mesoscale Meteorological Model (MM5) 24

1.1 Abstract 24

1.2 Introduction 25

1.3 Experimental design 28

1.3.1) Brief Description of HTSVS 28

1.3.2) The atmospheric model and simulations 29

1.3.3) Model domain 30

1.3.4) Synoptic situation 31

1.3.5) Initialization 32

1.3.6) Datasets 33

1.3.7) Analysis 33

1.4 Results and discussions 36

1.4.1) General remarks 36

1.4.2) Atmospheric near-surface quantities 38

1.4.3) Snow depths 41

1.4.3.1) TOTAL Change in SNOW DEPTH 42

1.4.3.2) INCREASE IN SNOW DEPTH 43

1.4.3.3) DECREASE IN SNOW DEPTH 45

1.4.4) Soil temperature 47

1.4.4.1) Diurnal course 49

1.5 Conclusions 49

1.6 Acknowledgements 51

1.7 REFERENCES 52

1.8 Figure captions 62

1.9 Table captions 64

Chapter 2 90

Implementation of a Galerkin Weak Finite Element scheme for the soil model of the Hydro-Thermodynamics Soil Vegetation Scheme (HTSVS) 90

2.1 Abstract 90

2.2 Introduction 91

2.3 Method 94

2.3.1) Short description of the soil model 94

2.3.2) Original numerical scheme 95

2.3.3) Proposed numerical scheme 97

2.4 Experimental design 101

2.4.1) Site and data description 101

2.4.2) Simulations 102

2.4.3) Analysis 103

2.5 Results and discussions 104

2.5.1) General remarks 104

2.5.2) CNFD Vs. observations 104

2.5.3) GWFE Vs. observations 105

2.5.4) Performance evaluation of CNFD and GWFE 106

2.6 Conclusions 107

2.7 Acknowledgements 109

2.8 REFERENCES 110

2.9 Table captions 115

2.10 Figure captions 116

List of Figures

Chapter 1

Figure 1. Terrain data as used in the model and schematic view of model domain location as well as location of snow sites 65

Figure 2. Comparison of terminal velocity as obtained by the Schultz and Reisner scheme at various snow-mixing ratios. 66

Figure 3. Comparison of observed (gray dots) and predicted (contour lines) 120h accumulated precipitation given as water equivalent (mm) 67

Figure 4. Comparison of (a) sea level pressure distribution (hPa), (b) surface air temperature distribution (K), and (c) specific humidity (g/kg) as obtained for RL (solid lines) and from reanalysis (dashed lines) on April 26 0000UT 71

Figure 5. Temporal evolution of RMSE. 74

Figure 6. Comparison of simulated and observed snow depth as obtained for RL. 76

Figure 7. Temporal evolution of RMSE and average absolute difference in simulated and observed snow depth as obtained by the four simulations. 77

Figure 8. Event scores of CSD determined over the entire episode 78

Figure 9. BIAS and accuracy 82

Figure 10. Temporal decrease of snow depth by compaction and settling only as obtained for various initial snow densities of a 2m thick snow pack. 83

Figure 11. Comparison of simulated and observed daily averaged soil temperatures as obtained with RL..... 84

Figure 12. Comparison of simulated and observed diurnal pattern of soil temperatures averaged over all 20 German stations. 85

Chapter 2

Figure 1. Comparison of simulated and observed soil temperature RMSEs using CNFD and GWFE schemes as obtained for various sites. 121

Figure 2. Averaged cell Peclet values …….124

Figure 3. Comparison of simulated and observed soil temperatures for H99 ……127

Figure 4. Comparison of simulated and observed soil temperatures for R02F ..……130

Figure 5. Soil temperatures obtained using CNFD and GWFE for R00T 5th layer 133

Figure 6. Simulation results for R01T 3rd layer show soil temperatures ……....134

Figure 7. Soil temperatures obtained using CNFD and GWFE for R01TN ...……....135

Figure 8. Soil water content (m^3/m^3) as obtained with H99 ……...139

List of tables

Chapter 1

Table 1. Summary of the parameterization and initialization methods used in the different simulations of this study. 87

Table 2. Soil characteristics assumed in our study. 88

Table 3. RMSE as obtained for the various simulations. 89

Chapter 2

Table 1. Soil physical parameters used in our study. ...…….117

Table 2. Duration of the simulations for different episodes along with the information of representative depths ……...118

Table 3. CPU time in seconds as obtained with CNFD and GWFE simulations …..….120

Introduction

The earth's surface is the only physical boundary in atmospheric models (e.g. numerical weather prediction models (NWPs), climate models) and it is typically described by a Land Surface Model (LSM). These LSMs serve to determine both the energy and water fluxes at the earth's surface (e.g. Dickinson et al., 1993; Robock et al., 1995; Huang et al., 1996). Research questions, like for instance examining the atmospheric response to land-use changes, require simulating the soil and surface conditions with high accuracy. LSMs provide fluxes of sensible and latent heat, momentum and water vapor across the land-atmosphere interface, as essentially required by both climatologists and meteorologists (e.g., Sellers et al., 1986; Bonan 1994; Robock et al., 1997). In recent years, many LSMs have been developed to simulate soil and surface variables (e.g., Bonan, 1998; Levis et al., 1996; Robock et al., 1995). Soil hydraulic conditions, for instance, are affected by snow depths, for which snow depth can influence freezing of soil water (e.g., Flerchinger, 1991). Designing an efficient LSM, capable of accurately simulating the soil moisture and associated soil and surface state variables, is an active research goal, because of the importance for such LSMs (e.g., Robock et al., 1997).

Slater et al. (1998), for instance, concluded from offline simulations that snow water-equivalent and snow density could be simulated reasonably well in general circulation models (GCMs) by introducing a snow parameterization of intermediate complexity. Kongoli and Bland (2000), when evaluating the Atmospheric-Land EXchange (ALEX) model offline at four sites by 13 years of data on snow accumulation,

ablation and snowmelt found the typical performance to be 0.02m, 0.85, 0.04m for average bias, average correlation, and average absolute departure of snow depth, respectively. The maximum average annual misclassified liquid precipitation was found to be 0.048m, and the maximum underestimation of snow accumulation for any site was 0.3m. Though the model underestimated the accumulated snow for some time during the simulation, on average, bias, absolute departure and, root mean square errors were 20mm, 40mm and 51mm, respectively.

Various intercomparison studies of LSMs for the offline evaluations (e.g. Chen et al., 1997; Wood et al., 1998) suggest that there exist no prominent differences of the functionality among various physically advanced LSMs. All these and other studies evidence that LSMs usually work appropriate when driven by observed meteorological data, i.e. run offline. The major errors that can propagate are associated with measurement errors, uncertainty in initial values and empirical parameters, and the assumptions made in the parameterizations, boundary conditions and numerical discretization of partial differential equations (PDEs).

Offline evaluation of LSMs means that they were driven by observed meteorological data, and simulated soil and snow conditions as well as surface fluxes were compared to the respective observations (e.g. Lou et al., 2003; Schlosser et al., 2000; Mölders et al., 2003a, b). If an LSM is coupled with an NWP or a climate model, additional uncertainty and error sources will become involved. Then the LSM is forced by simulated meteorological conditions that are subject to incorrect simulations of the forcing model, among other things, caused by erroneous or unknown initial conditions,

boundary conditions, inaccurate model assumptions, or the choice of inappropriate empirical parameters not only in the LSM, but also in the driving model. False predictions by the driving model may propagate to incorrect prediction in the state variables and fluxes predicted by the LSM, and lead to wrong forecasts of meteorological quantities that again affect the performance of the LSM. Furthermore, typically no site-specific empirical parameters are available at the resolution of the driving models for which errors in simulated soil and surface conditions may result.

NWPs, for instance, the PennState/NCAR Mesoscale Meteorological Model generation 5 (MM5; Dudhia, 1993; Grell et al., 1994) is used to typically predict 5 days of weather predictions in a short-term weather forecasts. Therefore efficient feedback between an LSM and an NWP is a prime concern for the efficient forecasts. This need underscores the importance of the evaluation of an LSM when coupled to an NWP, and an effective way to examine the efficiency of this coupling is to evaluate the coupled model in simulating the earth's surface variables such as soil temperature, moisture, soil heat and moisture fluxes, forecasting snow depth, and precipitation.

In first part of the thesis the Hydro-Thermodynamic Soil-Vegetation Scheme (HTSVS; Kramm, 1995; Kramm et al., 1994, 1996; Mölders et al., 2003a, b) - MM5 coupled model has been evaluated by BALTic sea Experiment (BALTEX) datasets to examine the coupled model performance in simulating soil temperature, snow depth, and precipitation values (e.g. Narapusetty and Mölders, 2005). The soil model of HTSVS makes use of the principles of linear thermodynamics of irreversible processes, including the Richards-equation (e.g., Kramm et al., 1996) and takes into account the effect of

seasonally frozen soil (e.g., Mölders et al., 2003a). This model also considers the Ludwig-Soret and Dufour effects, which have been found important during freezing/thawing and snowmelt (e.g., Mölders and Walsh 2004). A detailed description of the parameterized algebraic equation sets, as well as the PDEs governing physical processes in HTSVS for soil temperature, volumetric water content, including phase transition processes and water extraction by roots is given by Mölders et al. (2003a). These PDEs are solved using Crank-Nicholson based Finite Differences (CNFD) numerical scheme, in conjunction with Gauss-Seidel iterating technique (e.g., Kramm, 1995). Evaluation studies showed that HTSVS successfully predicted various atmospheric variables in short term simulations (e.g., Kramm 1995; Mölders, 2000). Mölders et al. (2003a, b) revealed the effective applicability of HTSVS on the long term for the water budget quantities as well as soil temperatures with respect to frozen ground. Mölders and Walsh (2004) applied HTSVS with embedded soil-frost-module coupled with MM5 to estimate the influence of soil frost and snow cover on weather in Alaska. In the HTSVS-MM5 evaluation using the BALTEX datasets, Narapusetty and Mölders (2005) performed sensitivity studies for the coupled system for two different cloud microphysical schemes, namely, the Schultz (1995) and Reisner et al. (1998) schemes, and two radiation schemes, namely, the Community Climate Model version 2 (CCM2; Briegleb, 1992) and the so-called CLOUD radiation scheme(Stephens, 1978, 1984; Garand, 1983). Forecast skills to evaluate the snow depth predictions are calculated in accordance with Anthes (1983) and Anthes et al. (1989).

As pointed out above, the equations presented in the soil model of HTSVS are coupled, nonlinear in time and involves multiple variables. Applying HTSVS for Arctic regions means that there exist a lot of discontinuities in the soil with respect to frozen ground and liquid water, note that soil ice and liquid water may coexist. These discontinuities play a crucial role in predicting the variables for a long term investigations. The freezing time typically shows a strong diurnal cycle in the active layer. The interface frozen ground versus unfrozen ground means a steep discontinuity with respect to soil liquid water content and soil water fluxes. Because of these discontinuities in the soil state, soil variables are to be treated more accurately.

If such discontinuities occur, solving the PDEs associate with HTSVS's soil model by using the CNFD may be a limitation due to the approach's diffusive nature. For relatively high cell Peclet number regimes, CNFD may show spurious oscillations, and phase shift from the observed values, and thus should be replaced with a computationally advanced scheme to over come this situation (e.g. Donea and Huerta, 2003). It has to be examined whether such limitations occur in Arctic or sub Arctic regions. Here efficient simulation of feedbacks between the soil and the atmosphere are desirable, especially in permafrost soils in the light of possible global warming, as significant quantities of carbon and methane exist in permafrost soils (e.g. Post et al., 1982; Romonovsky and Osterkamp, 1997). In high-latitude wetlands, the microbial methane formation in permafrost soils demands efficient capture of freeze-thaw cycles as the microbial activity is enhanced by an immoderate temperature and moisture gradients (e.g., Christensen et al., 1995; Wagner et al., 2003).

To this end a new numerical approach is to be treated in HTSVS that is able to capture the discontinuities associated with the freezing line and to correctly capture phase shifts, and which better approximates the various terms presented by the PDEs of HTSVS's soil model. By choosing an advanced numerical algorithm for governing equations, one would increase the resolution of the predictions; on the other hand the new computational algorithm should also maintain the local conservation, monotonic and non-oscillatory properties (e.g. Lin et al., 2004).

To capture the discontinuities or shock fronts like they occur in temporally frozen ground, a numerical method is required, which gives sharp resolution at the discontinuities, and at the same time provides high order approximations for smooth regions with the above mentioned properties. As the soil layers of a typical Arctic or sub Arctic regions are marked with moderate values of typical cell Peclet numbers, we propose to use Galerkin Weak Finite Element Method (GWFE; e.g. Crandall, 1956; Finlayson 1972; Oden 1972; Fletcher, 1984; Johnson, 1987; Smith and Griffiths, 1988). Particularly in a regime, where soil layers are dominated by high advection dominated flows, for example cell Peclet numbers have the values beyond 5, one can use streamline-upwind/Petrov-Galerkin (e.g. Hughes et al., 1987; Brooks and Hughes, 1982), Galerkin/least-squares (e.g. Hughes and Hulbert, 1988; Shakib 1988; Hughes et al., 1989). In these stabilization methods, the finite element (FE) interpolation functions are discontinuous in time and hence prompt to solve for one time-space slab each time, so requires more computational burden (e.g. Tezduyar, 1992).

By considering the balance between computational efficiency and quality in approximating solution variables, the GWFE is used to solve the PDEs in the soil model of HTSVS. The scheme's performance over CNFD's performance is evaluated using the root mean square errors (RMSEs) of soil temperatures, extracted from the datasets of three observational sites around Council, Alaska, with varying soil and vegetation types for various seasons in the years 1999, 2000, 2001 and 2002. The second part of the thesis presents the new numerical scheme, its evaluation both with respect to observations as well as in comparison to the CNFD scheme. The last chapter gives some overall conclusions and lines out what has to be done in the future.

REFERENCES

Anthes, R. A., 1983: Regional models of the atmosphere in middle latitudes. *Mon. Wea. Rev*., **111,** 1306-1335.

Anthes, R.A., Y.H. Kuo, E.Y. Hsie, S. Low-Nam, and T.W. Bettge, 1989: Estimation of skill and uncertainty in regional numerical models. *Quart. J. Roy. Meteorol. Soc*., **111,** 763-806.

Bonan, G. B., 1994: Comparison of two land surface process models using prescribed forcings. *J. Geophys. Res*., **99,** 25803-25818.

Bonan, G. B., 1998: The Land Surface Climatology of the NCAR Land Surface Model Coupled to the NCAR Community Climate Model. *J. Climate*., **11,** 1307-1326.

Briegleb, B. P., 1992: Delta-Eddington approximation for solar radiation in the NCAR community climate model. *J. Geophys. Res*., **97**, 7603-7612.

Brooks, A. N., and T. J. R. Hughes, 1982: Streamline-upwind/Petrov-Galerkin formulations for convection dominated flows with particular emphasis on incompressible Navier-Stokes equations. *Comput. Meth. Appl. Mech. Eng.,* **32,** 199-259.

Chen, T.H., A. Henderson-Sellers, P.C.D. Milly, A.J. Pitman, A.C.M. Beljaars, J. Polcher, F. Abramopoulos, A. Boone, S. Chang, F. Chen, Y. Dai, C.E. Desborough, R. E. Dickinson, L. Dümenil, M. Ek, J.R. Garratt, N. Gedney, Y.M. Gusev, J. Kim, R. Koster, E.A. Kowalczyk, K. Laval, J. Lean, D. Lettenmaier, X. Liang, J.-F. Mahfouf, H.-T. Mengelkamp, K. Mitchell, O.N. Nasonova, J. Noilhan, A. Robock, C. Rosenzweig, J. Schaake, C. A. Schlosser, J.-P. Schulz, Y. Shao, A.B. Shmakin, D.L. Verseghy, P. Wetzel, E.F. Wood, Y. Xue, Z.-L. Yang, and Q. Zeng, 1997: Cabauw

experimental results from the Project for Intercomparison of Land-Surface Parameterization Schemes. *J. Climate*., **10**, 1194-1215.

Christensen, T. R., S. Jonasson, T. V. Callaghan, and M Havström, 1995: Spatial variation in high-latitude methane flux along a transect across Siberian and European tundra environments. *J. Geophys. Res.,* **100,** 21035-21045.

Crandall, S. H., 1956: Engineering Analysis. McGraw-Hill, New York.

Dickinson RE, Henderson-sellers A, Kennedy PJ (1993) Biosphere Atmosphere Transfer Scheme (BATS) version 1e as coupled to the NCAR Community Climate Model. NCAR Technical Note, NCAR/TN-378 + STR

Donea, J., and A. Huerta, 2003: Finite element Methods for Flow Problems. John Wiley & Sons *Ltd*.

Dudhia, J., 1993: A non-hydrostatic version of the Penn State NCAR mesoscale model: validation tests and simulation of an Atlantic cyclone and cold front. *Mon. Wea. Rev*., **121,** 1493-1513.

Finlayson, B. A., 1972: The Method of Weighted Residuals and Variational Principles. Academic Press, New York and London

Flerchinger, G. N., 1991: Sensitivity of soil freezing simulated by the SHAW model. *Trans. ASAE*., **34 (6),** 2381-2389.

Fletcher, C. A. J., 1984: Computational Galerkin Methods. Springer-Verlag New York *Inc.*

Garand, L., 1983: Some improvements and complements to the infrared emissivity algorithm including a parameterization of the absorption in the continuum region. *J. Atmos. Sci.*, **40**, 230-244.

Grell, G., J. Dudhia, and D. Stauffer, 1994: A description of the Fifth-Generation Penn State/NCAR Mesoscale Model (MM5) NC Kramm, G., 1995: *Zum Austauch von Ozon und reaktiven stickstoffverbindungen zwischen Atmospheare und Biosphäre*. Frankfurt, Maraun-Verlag, p 268.

Huang J, Van Den Dool HM, Georgakakos KP(1996). Analysis of Model-Calculated Soil Moisture over the United States(1931-1993) and Applications to Long-Range Temperature Forecasts, J Climate 9: 1350-1362

Hughes, T.J.R., L.P. Franca, and M. Mallet, 1987: A new finite element formulation for computational fluid dynamics: VI. Convergence analysis of the generalized SUPG formulation for linear time-dependent multi-dimensional advective-diffusive systems, *Comp. Methods Appl. Mech. Eng.,* **63,** 173-189.

Hughes, T.J.R., and G. M. Hulbert, 1988: Space-time finite element methods for elastodynamics: Formulations and error estimates, *Comp. Methods Appl. Mech. Eng.,* **66**, 339-363.

Hughes, T.J.R., L.P. Franca, and G.M. Hulbert, 1989: A new finite element formulation for computational fluid dynamics: VIII The Galerkin/least squares method for advective-diffusive equations, *Comp. Methods Appl. Mech. Eng.,* **73,** 173-189.

Johnson, A., 1987: Numerical solution of partial differential equations by the finite element method. Cambridge University Press.

Kongoli, C.E., and W.L. Bland, 2000: Long-term snow depth simulations using a modified atmosphere-land exchange model. *Agric. For. Meteorol*., **104,** 273-287.

Kramm, G., and F. Herbert, 1994: Ein numerisches Modell zur Deposition von Schadstoffen in der bodennahen Luftschicht. In: Reuter, H. (Ed.) , Probleme der Umwelt- und Medizinmeteorologie im Gebirge , Symposium Rauris/Österreich, 23.-25. September 1983, *Zentralanstalt f. Meteorologie u. Geodynamik, Wien*., **288,** 22-38 pp. (in German)

Kramm, G., 1995: *Zum Austauch von Ozon und reaktiven stickstoffverbindungen zwischen Atmospheare und Biosphäre*. Frankfurt, Maraun-Verlag, p 268.

Kramm, G., N. Beier, T. Foken, H. Müller, P. Schroeder, and W. Seiler, 1996: A SVAT scheme for NO, NO_2, and O_3 – model description. *Meteorol. Atmos. Phys*., **61,** 89-106.

AR/TN. 398 + STR.

Levis, S., M. Coe, and J. A. Foley, 1996: Hydrologic budget of a land surface model: A global application. *J. Geophys. Res*., **101(D12),** 16 921-16 930.

Lin S.J., Atlas R., and K. S. Yeh, 2004: Global Weather Prediction and High-End Computing at Nasa. *Comput. Sci. & Eng.* **6,** 29-35.

Lou, L., A. Robock, K.Y. Vinnakov, C.A. Schlosser, A.G. Slater, A. Boone, H. Braden, P. Cox, P. De Rosnay, R.E. Dickinson, Y. Dai, Q. Duan, P. Etchevers, A. Henderson-Sellers, N. Gedney, Y.M. Gusev, F. Habets, J. Kim, E. Kowalczyk, K. Mitchell, O.N. Nasonova, J. Nilhan, A.J. Pitman, J. Schaake, A.B. Shmakin, T.G. Smirnova, P. Wetzel, Y. Xue, Z.-L. Yang, and Q.-C. Zeng, 2003: Effects of frozen soil on soil

temperature, spring infiltration, and runoff: Results from the PILPS 2(d) experiment at Valdai, Russia. *J. Hydrometeorol*., **4,** 334-351.

Mölders, N., 2000: HTSVS – A new land-surface scheme for MM5. In *The tenth PSU/NCAR Mesoscale model users' workshop*., 33-35 (available from NCAR, P.O. Box 3000, Boulder, CO 80307, USA or http://www.mmm.ucar.edu/mm5/mm5.html).

Mölders, N., U. Haferkorn, J. Döring, and G. Kramm, 2003a: Long-term investigations on the water budget quantities predicted by the hydro-thermodynamic soil vegetation scheme (HTSVS) – Part I: Description of the model and impact of long-wave radiation, roots, snow and soil frost. *Meteorol. Atmos. Phys*., **84,** 15-135.

Mölders, N., U. Haferkorn, J. Döring, and G. Kramm, 2003b: Long-term investigations on the water budget quantities predicted by the hydro-thermodynamic soil vegetation scheme (HTSVS) – Part II: Evaluation, sensitivity, and uncertainty. *Meteorol. Atmos. Phys*., **84,** 137-156.

Mölders, N., and J.E. Walsh, 2004: Atmospheric response to soil frost and snow in Alaska in March. *Theor. Appl. Climatol*., **77,** 77-115.

Narapusetty, B., and Mölders, N., 2005: Evaluation of snow depth and soil temperatures predicted by the Hydro Thermodynamic Soil Vegetation Scheme (HTSVS) coupled with the PennState/NCAR Mesoscale Meteorological Model version 5 (MM5). *J. App. Meteorol.* (*in press*)

Oden, J. T., 1972: Finite elements of nonlinear continua. McGraw-Hill, New York

Post, W. M., W. R. Emanuel, P. J. Zinke, and A. G. Stangenberger, 1982: Soil carbon pools and world life zones. *Nature,* **298,** 156-159.

Reisner, J., R.J. Rasmussen, and T. Bruintjes, 1998: Explicit forecasting of supercooled liquid water in winter storms using the MM5 mesoscale model. *Quart. J. Roy. Meteorol. Soc*., **124B,** 1071-1107.

Robock A, Konstantin YV, C. Adam S, Nina A S, Yongkang X (1995) Use of midlatitude soil moisture and meteorological observations to validate soil moisture simulations with biosphere and bucket models. J Climate 8: 15-35

Robock A, Vinnikov KY, Schlosser CA (1997) Evaluation of land-surface parameterization schemes using observations. J Climate 10: 377-379

Romanovsky, V. E., and T. E. Osterkamp, 1997: Thawing of the Active Layer on the Coastal Plain of the Alaskan Arctic. *Permafrost and Periglacial Processes,* **8,** 1-22.

Schlosser, C.A., A.G. Slater, A. Robock, A.J. Pitman, Y.V. Konstantin, A. Henderson-Sellers, N.A. Speranskaya, and K. Mitchell, 2000: Simulation of a Boreal Grassland Hydrology at Valdai, Russia. PLPS Phase 2(d), *Mon. Wea. Rev*., **128**, 301-321.

Schultz, P., 1995: On explicit cloud physics parameterization for operational numerical weather prediction. *Mon. Wea. Rev*., **123,** 3321-3343.

Sellers, P., Y. Mintz, Y. Sud, and A. Dalcher, 1986: A simple Biosphere (SiB) for use within General Circulation Models. *J. Atmos. Sci.*, **43,** 505-531

Shakib, F., 1988: Finite element analysis of the compressible Euler and Navier-Stokes equations. *Ph.D. Thesis*, Stanford University.

Slater, A. G., A. J. Pitman, and C. E. Desborough 1998: The validation of a snow parameterization designed for use in general circulation models. *Int. J. Climatol*., **18,** 595-617.

Smith I. M., and D. V. Griffiths, 1988: PROGRAMMING THE FINITE ELEMENT METHOD, Second Edition. John Wiley & Sons *Ltd.*

Stephens, G.L., 1978: Radiation profiles in extended water clouds, Part II. Parameterization schemes. *J. Atmos.Sci.,* **35,** 2123-2132.

Stephens, G.L., 1984: The parameterization of radiation for numerical weather predication and climate models. *Mon. Wea. Rev.,* **114,** 1330-1339.

Tezduyar, T.E., 1992: Stabilized Finite Element Formulations for Incompressible Flow Computations, *Adv. in Appl. Mech.*, **28**,1-44.

Wagner, D., S. Kobabe, E. M. Pfeiffer, and H. W. Hubberten, 2003: Microbial controls on methane fluxes from a polygonal tundra of the Lena Delta, Northeast Siberia. *Permafrost and Periglacial Processes,* **14,** 173-185.

Wood, E.F., D.P. Lettenmaier, X. Liang, D. Lohmann, A. Boone, S. Chang, F. Chen, Y. Dai, R.E. Dickinson, Q. Duan, M. Ek, Y.M. Gusev, F. Habets, P. Iraanejad, R. Koster, K.E. Mitchel, O.N. Nasonova, J. Noilhan, J. Schaake, A. Schlosser, Y. Shao, A.B. Shmakin, D. Verseghy, K. Warrach, P. Wetzel, Y. Xue, Z.-L. Yang, and Q.-C. Zeng, 1998: The Project for Intercomparison of Land-surface Parameterization Schemes (PILPS) Phase 2(c) Red-Arkansas river basis experiment: 1. Experiment description and summary intercomparisons. *Global and Planetary Change*, **19**, 115-135.

Chapter 1

Evaluation of snow depth and soil temperatures predicted by the Hydro-Thermodynamic Soil-Vegetation Scheme (HTSVS) coupled with the PennState/NCAR Mesoscale Meteorological Model (MM5) *

1.1 Abstract

The Hydro-Thermodynamic Soil-Vegetation Scheme (HTSVS) coupled in a two-way mode with the PennState/National Center for Atmospheric Research (NCAR) Mesoscale Meteorological Model generation 5 (MM5) is evaluated for a typical snow-melt episode in the Baltic region by means of observations at 25 soil temperature, 355 snow depth and 344 precipitation sites having in total 1000, 1775, and 1720 measurements, respectively. The performance with respect to predicted near-surface meteorological fields is evaluated using reanalysis data.

Snow depth depends on snow metamorphism, sublimation and snowfall. Since in the coupled model these processes are affected by the predicted surface radiation fluxes and cloud and precipitation processes, we perform sensitivity studies with two different cloud microphysical schemes and/or radiation schemes. Skill scores are calculated as a quality measure for the coupled model's performance for a typical forecast range of 120h for a typical spring (snowmelt) weather situation in the Baltic region. Discrepancies between predicted and observed snow depth changes relate to the coupling. Enhanced water supply to the atmosphere, which results from water that was assumed to be open in

---

* Narapusetty, B. and N. Mölders, 2005. Journal of Applied Meteorology (in press)

MM5 but was actually ice-covered in nature, finally leads to an overestimation of snowfall (input to HTSVS) and changes in snow depth (output). The resolution-dependent discrepancies between the terrain height in the model and real world also lead to snowfall where none occurred.

For heavy snowfall the performance of the coupled model with respect to predicted snow depth changes becomes nearly independent of the choice of the cloud microphysical and radiation schemes. As compared to observed changes in snow depth, the coupled model simulation using the Schultz (1995) scheme in conjunction with the Community Climate Model version 2 (CCM2) radiation scheme predicts snow depth changes less than 2.5mm considerably better than the other combinations tested. For thick snow packs accuracy of snow depth decrease due to metamorphism strongly depends on the initial value of snow density.

The coupled model acceptably captures the soil temperature diurnal cycles, the observed soil temperature increase with time and behavior with depth. Generally, discrepancies between simulated and observed soil temperatures decrease with soil depth. Simulations performed with the so-called CLOUD radiation scheme capture soil temperature minima and maxima better than do simulations performed with the CCM2 scheme.

1.2 Introduction

In numerical weather prediction (NWP) and climate models, typically a land surface model (LSM) determines the temperature and moisture states and heat and moisture fluxes within the soil, canopy and/or snow as well as the fluxes of sensible and

latent heat and momentum at the land-atmosphere interface (e.g. Sellers et al., 1986; Bonan, 1994; Robock et al., 1997). These LSMs have been developed using the best of our scientific knowledge and great effort has been spent in evaluating them (e.g. Henderson-Sellers et al., 1993, 1995; Chen et al., 1997; Yang et al., 1997; Wood et al., 1998; Schlosser et al., 2000; Lou et al., 2003; Mölders et al., 2003a, b). Usually these evaluations have been performed offline, i.e. the LSMs were driven by observed meteorological data. These studies evidenced that LSMs usually work appropriately when run in an offline mode. The major propagating errors are associated with measurement errors, uncertainty in initial values and empirical parameters, and the assumptions made in parameterization, boundary conditions and numerical discretization.

If an LSM is coupled with an NWP or climate model, the simulated meteorological forcing conditions will be an error source. The forcing can be wrong due to, among other things, erroneous or unknown initial conditions, boundary conditions, discretization, grid resolution, inaccurate model assumptions, or choice of inappropriate empirical parameters (e.g. Anthes et al., 1989; Zhong et al., 2005). Obviously, these false forcing conditions may propagate to incorrect prediction of the state variables and fluxes by the LSM again affecting the forecasts of meteorological quantities. Furthermore, typically no site-specific empirical parameters are available at the resolution of NWP or climate models resulting in erroneous predictions of soil and surface conditions.

For the reasons outlined above, the performance of an LSM decreases as compared to offline simulation when it is coupled to another model. Based on five months of area-averaged observations, Chen et al. (1996), for instance, found that in an

offline mode the Oregon State University LSM (OSULSM) correctly captures the diurnal cycle in surface-heat flux and differences in simulated and observed skin temperature could be as high as 5K. Chen and Dudhia (2001) reported that a modified version of OSULSM coupled with the PennState/National Center for Atmospheric Research (NCAR) Mesoscale Meteorological Model generation 5 (MM5; Dudhia, 1993; Grell et al., 1994) made an excellent prediction of latent heat flux and predicted sensible heat flux within 100Wm^{-2} accuracy. Visual comparison of Chen et al.'s (1996) figures showing the offline performance for June 4, 5 and 6, 1981 with the results from the coupled simulation for the same days shown in Chen and Dudhia (2001) indicates a decrease in performance for the coupled model of about 3K for temperature, and 85Wm^{-2} for sensible heat fluxes. This example demonstrates that the additional "error" sources introduced by running an LSM and NWP model in a coupled mode requires a re-evaluation of the performance of any LSM when introduced into a coupled model.

This task is addressed in this article for the Hydro-Thermodynamic Soil-Vegetation Scheme (HTSVS; Kramm et al., 1996; Mölders et al., 2003a) that recently was coupled in a two-way mode with MM5 (Mölders, 2000; Mölders and Walsh, 2004). In offline evaluation studies, HTSVS predicted soil temperature within ±2.5K in the short-term (e.g. Kramm, 1995), and the water supply to the atmosphere and groundwater recharge within 15% accuracy as well as daily mean soil temperatures within 1-2 K in the long-term (2050 days simulation; Mölders et al., 2003a, b). Note that besides being used in MM5 for permafrost and snow studies (e.g. Mölders and Walsh, 2004) HTSVS has been used in one-dimensional chemistry models for air quality studies (e.g. Kramm et al.,

1996), and in the GEesthacht SImulation Model of the Atmosphere (GESIMA; Kapitza and Eppel 1992; Eppel et al., 1995) as an alternative LSM (e.g. Mölders and Rühaak, 2002) to the force-restore method including vegetation processes (Claussen, 1988) usually applied. The aim of our study is to evaluate HTSVS coupled to MM5 using soil temperature and snow depth data obtained in the BALTic sea EXperiment (BALTEX; e.g. Raschke et al., 1998) for a five day spring episode.

1.3 Experimental design

1.3.1) Brief Description of HTSVS

HTSVS (Kramm et al., 1996; Mölders et al., 2003a; Mölders and Walsh, 2004) consists of a one-layer canopy model and a multi-layer snow and soil model. The canopy model describes the exchanges of momentum, heat, and moisture at the vegetation-soil-atmosphere interface. It considers micro-scale heterogeneity by a mixture approach, i.e. a grid cell can be partly covered by vegetation (e.g. Deardorff, 1978; Kramm et al., 1996).

The multi-layer snow model follows Fröhlich and Mölders (2002) with the modifications and additions required for the coupling to MM5 described in Mölders and Walsh (2004). Snow depth increases by snowfall, and it decreases by sublimation, outflow of meltwater, windbreak, compaction, settling, meltwater percolation, and freezing. The processes contributing to a snow-depth decrease are denoted snow metamorphism. Like in many other LSMs (e.g. Verseghy, 1991; Loth and Graf, 1998; Bonan et al., 2002) a minimum thickness (2mm) is assumed for each snow model layer to consider snow metamorphism except melting which may occur independent of thickness.

The soil model makes use of the principles of linear thermodynamics of irreversible processes (e.g. de Groot, 1951; Prigogine, 1951), including the Richards equation (e.g. Philip, 1957; Philip and de Vries, 1957; de Vries, 1958; Kramm, 1995; Kramm et al., 1996) and takes into account freezing and thawing of soil (e.g. Mölders et al., 2003a). It also considers the Ludwig-Soret effect (i.e. a temperature gradient contributes to the water flux and changes the soil volumetric water content) and the Dufour effect (i.e. a moisture gradient contributes to the heat flux and alters soil temperature). These so-called cross effects have been found important during freezing/thawing, snowmelt (e.g. Mölders and Walsh, 2004), and when chemicals are involved. For a detailed description of the parameterized algebraic equation sets and the differential equations governing the physical processes in HTSVS for soil temperature, volumetric water and ice content, including phase transition processes and water extraction by roots see Mölders et al. (2003a).

1.3.2) The atmospheric model and simulations

MM5 can be run with various physical parameterizations (Grell et al., 1994). The parameterizations of radiation and cloud microphysical processes can most strongly affect the coupled MM5-HTSVS performance. To elaborate sources of discrepancies between simulated and observed snow depth caused by the radiation scheme we carry out simulations using alternatively the Community Climate Model version 2 (CCM2) radiation scheme with a δ-Eddington method (Briegleb, 1992) and the so-called CLOUD radiation scheme (Stephens, 1978, 1984; Garand, 1983). For simplicity we denote these

radiation schemes as CCM2 and CLOUD scheme, the names under which they are known in the MM5 community.

To assess the impact of the cloud microphysical scheme on snow depth increase we perform simulations using the modified version of Reisner et al.'s (1998) mixed-phase scheme with graupel (Thompson et al., 2004), and alternatively Schultz's (1995) scheme.

In the following, the simulations performed with the Schultz and CCM2 schemes, or alternatively the Reisner and CCM2 schemes, and their results are named SC and RC, respectively. Simulations and their results obtained with the Schultz and CLOUD schemes or alternatively the Reisner and CLOUD schemes are called SL and RL (Tab. 1).

As the grid resolution chosen in our simulations (35km) requires the use of a cumulus convection scheme, we consider Grell et al.'s (1991) cumulus scheme. Boundary layer physics is considered in accordance with Hong and Pan (1996).

1.3.3) Model domain

The model domain encompasses the BALTEX region from the surface to 100hpa with a center at 17.5^{o}E, 60^{o}N (Fig. 1). The horizontal resolution is 35km with 57x45 grid points. Five soil layers are spaced by the same logarithmic increment so that central differences can be used in solving the coupled soil equations by a generalized Crank-Nicholson scheme in combination with a Gauβ-Seidel technique. Since the forecast range of MM5 is generally restricted to several days to a week, soil temperature, volumetric water and ice content are held constant throughout a simulation at the lower boundary of the soil model for simplicity. In the case of snow, there are five snow layers

of equal thickness that get re-divided whenever snow depth changes. The simulations are performed with a time step of 105 seconds.

1.3.4) Synoptic situation

The episode chosen encompasses April 21 0000UT to April 26 0000UT, 2000, and is a typical snowmelt weather situation in the Baltic region in spring. On April 21, the eastern part of the region was influenced by a moderate high-pressure system, while the western part was governed by a trough associated with intensive cyclonic activity, with the center in the northern Atlantic, west of the British Islands. On April 22, most of the region was under high-pressure influence. In the northern part, cyclonic activity cut off from the trough, developed, and moved eastward. On April 23, Estonia, Finland and Latvia were under weak high-pressure influence, whereas Norway, Sweden and Russia were affected by a low-pressure system. The latter lost its energy, while the newly formed system strengthened due to advection of Arctic air. On April 24, a low pressure system moved into northern Finland from the east. Germany and Norway were governed by a northward moving low-pressure system, while the weakened high-pressure system remained over Belarus, Lithuania, and northern Poland. On April 25, the cyclonic activities joined and affected Sweden and Norway, while the high pressure system intensified and moved eastward.

On April 21 air temperatures ranged from -3 to 0^{o}C in Norway, Sweden and Finland, and from 9 to 0^{o}C in Germany, Poland, and Belarus. The warm front moved northward on April 22 followed by a cold wave front entering from the Arctic. On April

23, the cold wave entered the southern part of the model domain, while in the eastern part temperatures still reached up to 9°C. On April 24, the cold wave quickly moved north influencing Norway, Sweden, and Finland with near-surface temperatures between -12 and 0°C. On April 25, warm air with near-surface air temperatures of up to 9°C was advected from Estonia and Latvia towards Sweden and Norway. During the episode near-surface wind speed ranged from 0 to 17m/s.

1.3.5) Initialization

To evaluate the performance of the coupled MM5-HTSVS we ran it continuously without re-initialization for the entire episode. Doing so permits enough time for feedback between the atmospheric and land-surface components of the coupled model. This means we do not use 48h composite runs started every 12h like Ek et al. (2003) in their evaluation of the performance of the National Center for Environmental Prediction (NCEP) model, because (1) such a procedure would reduce the amount of data useable for evaluation by the data needed for re-initialization, and (2) the time for establishing feedback between HTSVS and MM5 would be reduced to 48h.

The initial conditions and boundary conditions for the coupled model are taken from the NCEP and NCAR Reanalysis Project (NNRP). Vegetation fraction is extracted as a weighted combination of April and May mean green vegetation cover data (0.15° resolution) derived from Advanced Very High Resolution Radiometer data (Gutman and Ignatov, 1998). Soil type, terrain elevation and land-use type are derived from the ten-minute resolution United States Geological Survey terrain and vegetation data. Soil type is constant with depth. The soil parameters used are listed in Table 2.

We initialize snow depth and soil temperatures from observation on April 20, 2000 where possible and use interpolated NNRP data elsewhere. Initial total soil moisture is interpolated from NNRP data. Total soil water is partitioned between the solid and liquid phase according to Mölders and Walsh (2004). The soil model used for the reanalysis data uses a simpler approach than HTSVS. Offline studies show no significant change of soil temperature and moisture with time when soil moisture is initialized within the range of the values obtained from the NNRP data. Thus, we can expect that the model results will not be strongly affected by using these soil moisture values. Initial snow temperature is assumed to be equal to initial ground surface temperature. Initial snow density is set equal to 300kg/m^3, a typical value for the Arctic and sub-arctic at this time of year (e.g. Sturm et al., 1997).

1.3.6) Datasets

The data base of the BALTEX Meteorological Data Centre (BMDC) contains snow depth data for 355 sites in our model domain (Fig. 1). Snow depth is reported once a day. Daily averages of soil temperature measured at 0.2, 0.4, 0.8, 1.6, and 3.2m depth are available for five sites in Belarus. At 20 German sites, soil temperatures were recorded at 0.1, 0.2, and 0.5m depth at 0600, 1300 and 2000UT. Precipitation (water equivalent) was available at 344 sites in Sweden and Finland. In total, there are 1000 soil temperature, 1775 snow depth and 1720 precipitation measurements.

1.3.7) Analysis

We evaluate the four simulations (Tab. 1) by reanalysis data of near-surface air temperature, humidity, wind and sea level pressure calculating forecast skills in accord

with Anthes (1983) and Anthes et al. (1989). The performance of the coupled MM5-HTSVS is also evaluated by comparing simulated soil temperatures and snow depths to the respective observations. For comparisons, the locations of the stations are projected on the model domain under the assumption that a site is representative for the grid cell it falls into.

To evaluate the coupled model's ability to predict snow depth changes, we calculate the BIAS scores ($\mathrm{BIAS} = \frac{(N_1 + N_2)}{(N_1 + N_3)}$), and accuracy ($\mathrm{AC} = \frac{N_1 + N_4}{N_1 + N_2 + N_3 + N_4}$). These statistical scores are defined based on contingency tables where N_1 is an observed and simulated event, N_2 denotes an event not observed, but simulated, N_3 represents an event observed, but not simulated, and N_4 indicates an event that is neither observed nor simulated. Each table represents the number of events for which the simulated and observed changes fall into a certain threshold class (1, 2.5, 5, 10mm) for a given time and simulation. The BIAS score measures how the coupled model simulates the frequency of occurrence for a given snow-depth change, with BIAS=1 indicating a perfect simulation. An averaged BIAS>1 or BIAS<1 corresponds to a systematic over- or under-prediction. AC ranges between 0 (only incorrect predictions) and 1 (only correct predictions).

In the model, snow depth increases by snowfall and decreases by outflow of meltwater, windbreak, compaction, settling, and sublimation. Accurate prediction of precipitation is important for simulating snow depth increase. Therefore, we compare the results obtained by simulations using different cloud microphysical schemes to each other

and also to observations, to get insight into how the cloud treatment affects the coupled model's prediction of snow depth changes. Accurate prediction of alterations in the radiation budget and atmospheric cooling/heating rates is important for simulating snow depth decrease. Thus, the results gained by simulations using different radiation parameterization schemes are also compared to each other. Since discrepancies in snow depth may result from malfunctioning of different parts of the coupled model, we calculate the skill scores for decrease in snow depth (DSD) and increase in snow depth (ISD) in addition to the scores for total change in snow depth (CSD) (overall performance). Investigation of CSD evaluates the overall performance of the coupled model. ISD is dominated by the cloud microphysical scheme, and DSD is governed by snow metamorphism and the surface energy budget.

Since the numerical scheme of HTSVS requires equal logarithmic grid-spacing with respect to the soil layers, HTSVS calculates soil temperatures at approximately 0.1m, 0.23m, 0.54m, 1.27m, and 2.95m depth, respectively. For comparison we interpolate predicted soil temperatures to the observational levels using a distance-weighted approach. In the following, soil layers are counted from the surface to the bottom of the soil model, and are addressed with respect to the model, i.e. the uppermost model layer is called layer 1, and the deepest layer is layer 5.

The coupled model's ability to simulate the diurnal cycle of soil temperature is evaluated by the observations at the 20 German sites that record data three times a day. We use all 20 German and all 5 Belarusian sites in the overall evaluation of daily soil temperatures predicted by the coupled model. Root mean square errors (RMSEs) of soil

temperatures are determined for each site at each depth. Considering all sites collectively, the total RMSE is calculated for each day and for the entire episode for the Belarusian and German sites.

1.4 Results and discussions

1.4.1) General remarks

MM5 applies the so-called strategy of dominant land-use and soil type. This means only one vegetation and soil type exists per grid cell. Nevertheless, the model considers heterogeneity on the micro-scale by a so-called mixture approach (e.g. Deardorff, 1978; Kramm et al., 1996), i.e. bare soil and one vegetation type are homogeneously distributed within the grid cell and no extended patches of either one (macro-scale heterogeneity) exist. Subgrid-scale heterogeneity on the macro-scale with respect to different vegetation or soil types and terrain elevation within a grid cell is not considered, nor is subgrid-scale variability of the snow cover taken into account. The latter would require the possibility of three different surface types (vegetation, bare soil, snow) in a grid cell. Consequently errors will arise from the dominant surface type approach, especially in areas of very heterogeneous soil and vegetation distribution and/or complex terrain. Since these errors have been discussed elsewhere in detail, we will not address them here (e.g. Avissar and Pielke, 1989; Leung and Ghan, 1995; Mölders and Raabe, 1996; Giorgi and Avissar, 1997; Boone et al., 2004).

Another source of discrepancies results from comparison of simulated and observed quantities itself. Observed soil temperatures or snow depths namely are point measurements, while simulated soil temperatures and snow depths represent volume

averages ($35x35km^2$ x soil layer thickness) and area averages ($35x35km^2$) for the entire grid cell, respectively. This kind of error is well-known (e.g. Avissar and Pielke, 1989; Seth et al., 1994; Boone et al., 2004; Zhong et al., 2005) and therefore not further examined here.

Primary differences between the simulations using the Schultz and Reisner schemes result from the different parameterization of cloud microphysical processes. Since comparisons of cloud microphysical schemes have been discussed elsewhere in detail (e.g. Mölders et al., 1994; Mölders and Laube, 1994; Kotroni and Lagouvardos, 2001), and our study focuses on evaluation of soil temperature and snow depth predicted by the coupled MM5-HTSVS, we restrict the discussion of the atmospheric part to the aspects important for the surface forcing, i.e. (1) the performance with respect to surface pressure, wind, near-surface air temperature and humidity prediction, and (2) the differences in cloud properties as they affect surface fluxes and states indirectly via absorption, transmission, scattering, and radiative cooling/heating, and directly via precipitation.

In the Schultz scheme, falling ice particles are assumed to be aggregates of non-rimed ice crystals, while they are ice crystals of hexagonal type in the Reisner scheme. Consequently, for the same snow-mixing ratios, snow settles up to $1.55ms^{-1}$ quicker (Fig. 2) and the water load is removed more rapidly in the simulations with the Schultz scheme than with the Reisner scheme. Therefore, the accumulated precipitation distributions predicted by the two schemes differ considerably (e.g. Fig. 3). The altered terminal

velocity also produces differences in cloud thickness and water-particle transport, and hence insolation and soil heat fluxes, which cause slight soil temperature differences.

The two different radiation schemes slightly differ with respect to the assumed profiles of absorbing gases, the spectral bands considered under clear-sky conditions, and the treatment of cloud-radiation interaction under cloudy conditions. These different assumptions primarily cause slight differences in simulated radiative cooling/heating rates. The resulting differences in vertical air temperature profiles affect stability, buoyancy, vertical mixing, and cloud formation/depletion, and finally the energy and water budget at the surface. Precipitation (Fig. 3) and latent heat flux (not shown), for instance, slightly differ in response to the radiation scheme chosen. The two fluxes mentioned affect snow depth changes and soil temperatures.

The major differences between the four simulations are as follows. Maximum accumulated precipitation is higher in the simulations with the Schultz than in those with the Reisner scheme (SC 39.5mm, SL 39.5mm, RC 30mm, RL 37mm). Precipitation starts and stops earlier in SC and SL than RC and RL.

1.4.2) Atmospheric near-surface quantities

All simulations capture well the evolution of the pressure field until the end of the simulation (e.g. Fig. 4). Then, the ridge reaching from the North Sea over the Baltic Sea is slightly overestimated in intensity (~1hPa), but underestimated in eastward extension.

During the entire episode, the coupled model tends to overestimate (underestimate) near-surface air temperatures in the snow-covered (snow-free) areas. Obviously, snow albedo decreases too quickly in MM5-HTSVS. Thus reflected

shortwave radiation is reduced and near-surface air temperatures increase. In MM5-HTSVS, albedo depends on vegetation fraction and soil moisture. Thus, in snow-free areas discrepancies between the assumed 5-year averaged weighted and actual vegetation fraction as well as the assumed mean and actual albedo of the vegetation may cause this underestimate. Moreover, incorrect initial soil moisture may play a role.

Near-surface specific humidity was overestimated (up to 6g/kg) under snowmelt regimes, while the opposite is true under other conditions (e.g. Fig. 4). This means sublimation and evaporation is overestimated during snowmelt. Here the overestimated air temperatures contribute to an overestimation of specific humidity as relatively warm air can take up more water vapor. Over the Baltic Sea near-surface specific humidity is overestimated up to 2.4g/kg for the following reason. MM5 uses a mean sea-ice distribution, under which some areas covered by sea-ice in nature are ice-free in the simulations. Since open water has a much lower albedo (<0.05) than sea-ice (>0.35), and because the surface temperature of open water is usually warmer than that of ice, near-surface air is relatively warmer over the seemingly open water in the model than in nature. Moreover, evaporation requires less energy than sublimation; more moisture can be supplied to the atmosphere over the seemingly nearly ice-free Baltic Sea in the simulations than can be supplied from the respective frozen area in nature.

As it is typical for mesoscale forecasts (e.g. Anthes et al., 1989; Colle et al., 2000, 2003), RMSE and BIAS gradually increase with simulation time (e.g. Fig. 5). In the first layer above ground, the RMSEs of air temperature and u- and v-components of the wind vector are about 11K, 9m/s and 10m/s, respectively, after 120h of simulation for all four

simulations. The simulations using the CLOUD scheme have lower RMSE for air temperature and wind speed than those using the CCM2 scheme (Fig. 5).

All four simulations capture well the area of high precipitation in northern Finland, and the areas of lower precipitation in southern Finland close to the Russian border (around 27°E, 62°N) (Fig. 3). Both cloud microphysical schemes predict snowfall for some Finnish sites located between 60°N and 65°N, 20°E and 25°E, where no snowfall was observed. In this area, they also often predict notable snowfall, when only a trace or slight snowfall was observed. Note that even traces of snowfall can notably affect the surface energy and water budget and hence soil temperature. The higher than observed accumulated precipitation in southern Finland (Fig. 3) results from the aforementioned discrepancies between the real and mean sea-ice distribution.

All simulations have an offset of up to two degrees in the position of the precipitation field in southern Sweden (around 57°5N, 12°, 15°E) (Fig. 3). This offset may be explained by the grid resolution. In the model, the average terrain height within a grid cell represents elevation. Thus, the Scandinavian Ridge is flatter in the model than at its highest points in nature. Therefore, under southwestern flow over the barrier, saturation and snowfall occur later and farther northeastwards in the model than in nature; water vapor is rather supplied to the atmosphere by sublimation and large-scale lifting in the model than by forced lifting at the mountain barrier. Consequently, grid cells corresponding to sites in Sweden often receive no snowfall in the model, although snowfall is actually observed in those locations. Finally this leads to an underprediction

of 120h-accumulated snowfall (Fig. 3). Note that Colle et al. (2000) and Zhong et al. (2005) reported that grid resolution significantly affects the precipitation bias.

1.4.3) Snow depths

Observed snow depth ranges between 0 and 1m in Finland, and between 0 and 1.97m in Sweden. For all four simulations the following behavior is found. On average, accumulated snow depths between 0.4 and 1.2m are overestimated, while the opposite is true for snow depth lower than 0.4m and higher than 1.6m (Fig. 6). On the high extreme of snow depths, no snowfall occurred at these sites for which the underestimate can only result from a too strong metamorphism. On the lower end, snow depth grew by snowfall in nature, while no snowfall is predicted on the first day in many cases due to model spin-up. Note that MM5 starts without clouds and it takes some time for clouds and precipitation to form in the model. Thus, this discrepancy is rather caused by the cloud microphysical schemes than the HTSVS snow model.

Since for the same snow-mixing ratio the Reisner scheme provides a lower terminal velocity (Fig. 2), snow is accumulated farther downstream in the simulations than in the simulations with the Schultz scheme (Fig. 3).

The correlation coefficients for simulated and observed snow depth amounts are 0.96, 0.97, 0.98 and 0.98 for RC, SC, RL and SL, respectively. For all simulations the RMSEs in snow depth increase with time. After the main snowfall event (April 22), averaged absolute differences remain nearly constant for all simulations (Fig. 7). SL followed by RL provides the best prediction of snow depth with respect to the averaged absolute differences and RMSE. Based on the (maximum) absolute differences and

RMSE the coupled model will provide better snow depth predictions if the CLOUD scheme is used instead of the CCM2 scheme.

1.4.3.1) TOTAL Change in SNOW DEPTH

Changes in snow depth encompass the effects of both increase and decrease in snow depth. Comparison of simulated and observed CSD permits assessment of the coupled model's overall performance with respect to snow predictions.

Overall, the number of grid cells with no CSD observed, but predicted (N_2), and CSD observed, but not predicted (N_3), decreases when the simulations are performed with the Reisner scheme (Fig. 8). Note that for SC, RC, SL, and RL N_2 is 8, 8, 8, and 7, and N_3 is 25, 19, 23, and 23, respectively. The reasons for these discrepancies are manifold. The assumption on ice crystal type affects terminal velocity (Fig. 2), for which the timing of precipitation onset and ending differs between the real and model world. The use of a mean sea-ice distribution overestimated precipitation for some Finnish sites, or even predicted precipitation when none occurred. Since HTSVS neglects subgrid-scale heterogeneity with respect to snow, discrepancies between the model and real world occur during snowmelt. In nature, radiative effects enhance snowmelt around obstacles sticking out of the snow. Their low albedos lead to a warming of the ambient air and increased melt rates. Once an area becomes snow-free, appreciable, free convection can be generated in nature, and the different heating rates and near-surface temperatures of snow-free and adjacent snow-covered patches can produce air circulation similar to sea or vegetation breezes (e.g. Baker et al., 1999). This phenomenon explains, for instance, the

N_3 values of SC and RC in the areas from 25° to 30°E around 62° N (Fig. 8). Occasionally, discrepancies also result from blowing snow. In the coupled model re-suspension and re-deposition are assumed to occur in the same grid cell, while in nature the horizontal transport may cause a decrease/increase at a site that falls into another grid cell with respect to the model, i.e. N_2 or N_3 change.

RL and SL only slightly differ with respect to the BIAS for all threshold values of changes in snow depths (Fig. 9). RL (SL) differs notably from RC (SC) that shows slightly higher BIAS than RL (SL) for the 1mm threshold, but much lower BIAS for the 5mm threshold. SL and RL have similar accuracy and accuracy is the highest for low and high thresholds of CSD. Since in SC, snow falls much quicker than in RC, no precipitation is falsely predicted for sites downwind of the main precipitation area, for which SC provides the highest accuracy for the total changes of intermediate thresholds of CSD. Overall RC shows the weakest performance.

1.4.3.2) INCREASE IN SNOW DEPTH

A decrease of snow depth by snow metamorphism is usually superimposed on any snow depth increase by snowfall. Thus, discrepancies in ISD may result from snowfall incorrectly predicted by the cloud microphysical scheme plus incorrect simulation of metamorphism processes by the HTSVS snow model.

For the reasons discussed before, snowfall is predicted in Finland in areas where none or only traces were observed (Fig. 3). This error is the most prominent for SC and the least for RC. Obviously, the Reisner scheme represents the snow-crystal type

occurring in this event better than the Schultz scheme, and hence captures better the precipitation distribution and amount, and consequently ISD.

Generally, the BIAS of ISD is greater for low (1 or 2.5mm) than high (5 or 10mm) thresholds (Fig. 9), because a slight precipitation event is much harder to predict than a notable one. In accord with findings by various authors (e.g. Chaumerliac et al., 1991; Mölders et al., 1995; Rassmussen et al., 2002), the onset of precipitation strongly differs depending upon the assumptions made about ice crystal type and microphysical processes. Therefore, the BIAS of low ISD is dominated by these systematic errors from the cloud microphysical scheme. The generally high BIAS for 1mm thresholds for SL and SC, which is slightly higher than that for RL, indicates that often precipitation begins too early due to the high terminal velocities in the Schultz scheme. Obviously RC provides the highest BIAS for ISD, while the other simulations perform similarly, broadly speaking. For intermediate thresholds of ISD the BIAS of RC is approximately twice as high as for the other simulations, with SC having the lowest BIAS. Note that ISD results from precipitation reduced by sublimation that is weaker than the precipitation. Obviously, RC overestimates sublimation for which the BIAS is high for low thresholds of ISD.

All simulations provide similar accuracy for threshold values greater than 10mm ISD (Fig. 9). ISD of this magnitude can only be achieved if cloud thickness is great and precipitation is strong because then differences in sublimation become comparatively small to the overall increase. Generally RC has the lowest, and SC the highest accuracy for ISD. RL and SL only slightly differ in accuracy. According to our findings the

inaccuracy in predicting ISD by the coupled model is caused by the cloud microphysical schemes rather than the feedback of processes simulated by HTSVS.

1.4.3.3) DECREASE IN SNOW DEPTH

Overestimation/underestimation of snowfall, clouds that are too thick (thus reducing incoming radiation, and hence sublimation), and overestimation of snow metamorphism are potential reasons for false prediction of DSD. Generally, great (absolute) snow depth decreases correspond to thick snow packs where compaction and settling dominate. The coupled model underestimates snow depth for great values of snow depth (Fig. 6), i.e. it overestimates snow metamorphism. Sensitivity studies show that an overestimate of initial snow density may be the reason. The rate of DSD by compaction depends on the weight of the overlying snow pack. An initial snow density that is too low consequently yields a DSD that is too large (Fig. 10) and can explain the differences found in our study. Note that the relative DSD (change in snow depth normalized with the total snow depth) is greater in thin than thick snow packs.

In thin snow packs, the contribution of sublimation can be of the same order of magnitude as compaction and settling, or greater. This means predicted DSD is more sensitive to incorrect prediction of the surface energy budget for thin snow packs than thick snow packs. Thin snow packs are also more sensitive to incorrectly predicted traces of snowfall because the relative change in snow depth is higher than for thick snow packs. As already mentioned, the coupled model predicts snowfall at some sites in

Finland where none was observed. This shortcoming will propagate to incorrectly predicted DSD.

As the threshold for DSD approaches 5mm, the BIAS of SC, RL, and SL approaches 1 indicating a nearly perfect prediction (Fig. 9). All four simulations slightly overestimate DSD for thresholds higher than 5mm. Since the process of snow metamorphism is well captured by HTSVS for the intermediate range of DSD, we may conclude that initialization of thick snow packs with a snow density of 300kg/m^3 is inappropriate. As can be derived from Fig. 10, higher initial values of snow density provide lower DSD and should be favored for initialization of thick snow packs.

The accuracy for DSD is the highest for SC and the lowest for RC for all thresholds (Fig. 9). Accuracy increases with increasing threshold of snow depth decrease. A slight decrease in snow is hard to capture. In RC, snow crystals sediment slower than in SC and sometimes traces of snowfall are predicted superimposed on a decrease by snow metamorphism when there is no snow falling in nature.

Generally high DSD rates coincide with low cloudiness or no clouds. Thus, at high thresholds of DSD, differences in accuracy decrease among the simulations using the different cloud microphysical schemes (Fig. 9). Sublimation depends, among other things, on solar radiation reaching the ground, which can be appreciably reduced by clouds. Thus, the slow removal of the hydrometeor load with the higher water supply to the atmosphere in RC is responsible for the lower accuracy at small thresholds as compared to the other simulations. Around 5mm DSD, RL, SC and SL show similar accuracy.

1.4.4) Soil temperature

Since no three-dimensional data sets on soil type are available at the resolution of NWP models, these models assume the same soil parameters for the entire soil column. Thus, the comparison performed here evaluates the typical practice in NWP modeling. Some of the discrepancies found between simulated and observed soil temperatures stem from this assumption. In the southern Baltic region, layers of different soil material frequently occur because most soils are sediments deposited during the ice ages.

For most of the 25 sites available, the coupled model tends to slightly underestimate soil temperatures (Fig. 11). Here the underestimate of near-surface air temperatures is the main reason. Correlation coefficients of simulated and observed soil temperatures are 0.917, 0.936, 0.955, and 0.949 for RC, SC, RL, and SL, respectively.

RMSE (Tab. 3) and differences between simulated and observed soil temperatures are the highest in the uppermost layer because variability is greater close beneath the surface than deeper in the soil and is hence more difficult to predict (Mölders et al., 2003b). Also, the uppermost layer can be strongly affected by incorrectly simulated atmospheric forcing. Furthermore, the chances that the soil temperature field is affected by the sensor installation are higher close beneath the surface than deeper in the soil. The impact of the atmospheric forcing and the diurnal variability decrease with depth, as do the differences between simulated and observed soil temperatures and RMSEs on average.

Generally, RMSEs and differences slightly increase with time. Over all soil temperature sites, RMSEs will be appreciably lower (up to 0.7K) if the CLOUD scheme is chosen. For the weather situation in our study, there is no obvious advantage for any

cloud microphysical scheme. However, our finding that radiation has a greater impact than cloud microphysical scheme on soil temperature prediction may be due to the fact that no precipitation occurred at the soil temperature sites. If snow occurred at the soil temperature sites, the accuracy of the snowfall prediction would influence the insulation and the heat flux into the soil, finally affecting soil temperature prediction. Note that a 10% error in snow depth alters RMSE by ± 0.1K, on average, over an entire winter (Mölders and Romanovsky, 2005), while a delay of snow cover onset by 10 days, for instance, can decrease maximum soil temperature by 9, 2.9, 2 and 1.1K at 0, 0.5, 1 and 2m depth (Ling and Zhang, 2003).

At the five Belarusian sites, daily soil temperatures averages are predicted correctly within -1K to 1.4K. In layers 2 to 5, RMSE are about 0.3K. At the 20 German sites, soil temperatures are underestimated by about 0.5-1K and 2K in layer 2 and 3, respectively.

At some of the 25 sites discrepancies are greater in layer 3 and 4 than at other layers. These discrepancies may result from assuming vertically constant soil characteristics in HTSVS, while in nature the soil characteristics may vary with depth at these sites. At some sites, RMSEs and differences remain greater in the lowermost layer than in the layer above. This behavior has to be considered as a model artifact that results from the constant soil temperature boundary condition at the bottom of the soil model. Sensitivity studies performed with a zero-flux boundary condition showed lower RMSE in layer 5 than the simulations using constant temperature and moisture conditions.

1.4.4.1) Diurnal course

According to the observations at the 20 German sites for which soil temperatures were reported at 0600, 1300, and 2000UT, the coupled model acceptably captures the diurnal course of soil temperature (e.g. Fig. 12). RMSE and absolute differences are higher at noon than early in the morning or evening. On average, all simulations slightly underestimate soil temperature for layer 2 at 0600UT, and the value at 1300UT is underestimated at most by 2.5K, while the value at 2000UT is predicted almost exactly. The simulations with the CLOUD scheme capture the nighttime minimum soil temperatures better than those with the CCM2 scheme.

1.5 Conclusions

The aim of our study is to evaluate HTSVS coupled to MM5 using soil temperature, snow depth and precipitation data obtained during a snow-melt episode of the BALTEX. Since snow depth changes depend, among other things, on the accurate prediction of precipitation and radiation, sensitivity studies are performed alternatively using two different radiation and cloud microphysical schemes.

Generally, discrepancies result from the assumption of a mean sea-ice distribution and coarse grid resolution. Water assumed to be open in the model, while being ice-covered in nature, increases the atmospheric water supply and finally leads to an overestimate of snowfall in the lee of the Baltic Sea and incorrect changes in snow depth. The resolution-dependent discrepancies between the terrain in the model and real world lead to snowfall where none or only traces occurred and consequently incorrect input for the HTSVS snow model, and incorrect changes in snow depth.

The main differences in performance with respect to snow depth changes occurring between the simulations with the Reisner and Schultz schemes are related to differences in simulated onset and end of precipitation. Once an area is influenced by high pressure, the radiation scheme will gain importance.

The simulation using the Reisner and CLOUD schemes shows the best overall performance. The accuracy of the forecast of low snow depth changes (1 or 2.5mm) is considerably higher for the Schultz and CCM2 radiation scheme than for all other combinations. The performance of the coupled model in predicting great snow depth changes (10mm) is nearly independent of the cloud microphysical and radiation schemes used. For thick snow-packs accuracy of snow depth decrease by metamorphism strongly depends on the initial value of snow density.

Generally, the BIAS for snow depth increase is greater for low (1 or 2.5mm) than high (5 or 10mm) thresholds, and much greater than for a decrease in snow depth. This means the BIAS of low snow depth changes is dominated by systematic errors from the cloud microphysical scheme.

Generally, the discrepancies in simulated and observed soil temperatures decrease with soil depth. The decrease rate is not of the same order for the bottom layer as for the other layers, because soil temperature and moisture are kept constant at the bottom of the model. Thus, a flux boundary condition should be used in long-term simulations like climate studies.

The coupled model tends to underestimate daily soil temperatures (up to 2.5K), because MM5 underestimates near-surface air temperatures slightly in Belarus, and

noticeably in Germany. It successfully captures the diurnal courses of soil temperatures, the increase of soil temperature with time, and temperature behavior with depth. The simulations with the CLOUD radiation scheme better predict the minima and maxima of diurnal soil temperature cycle than those with the CCM2 scheme. We have to expect that soil temperature prediction may be more strongly affected by the cloud microphysical schemes in snow-covered areas because snowfall prediction errors in MM5 will have a greater impact for locations with little or no snow. Such investigations should be carried out as soon as a great data base of soil temperature measurements under snow with concurrently measured snow depth become available during BALTEX.

1.6 Acknowledgements

We thank U. Bhatt, F. Chen, J. Dudhia, A. Ebel, H. Elbern, M. Jankov, A. Klioutchnikova, G. Kramm, Z. Li, F. Toussiant, J.E. Walsh and the anonymous reviewers for fruitful discussions and helpful comments. BMBF and NSF financially supported this study under contracts 01LD0036 and OPP-0327664. Narapusetty was financially supported by a graduate research scholarship of the University of Alaska Fairbanks' Graduate School. NCAR provided computational support.

1.7 REFERENCES

Anthes, R. A., 1983: Regional models of the atmosphere in middle latitudes. *Mon. Wea. Rev*., **111,** 1306-1335.

Anthes, R.A., Y.H. Kuo, E.Y. Hsie, S. Low-Nam, and T.W. Bettge, 1989: Estimation of skill and uncertainty in regional numerical models. *Quart. J. Roy. Meteorol. Soc*., **111,** 763-806.

Avissar, R. and R.A. Pielke, 1989: A parameterization of heterogeneous land surface for atmospheric numerical models and its impact on regional meteorology. *Mon. Wea. Rev.,* **117**, 2113-2136.

Baker, J.M., K.J. Davis, and G.C. Liknes, 1999: Surface energy balance and boundary layer development during snow melt. *J. Geophys. Res*., **104D,** 19611-19621.

Bonan, G. B., 1994: Comparison of two land surface process models using prescribed forcings. *J. Geophys. Res*., **99,** 25803-25818.

Bonan, G.B., K.W. Oleson, M. Vertenstein, S. Levis, X. Zeng, Y. Dai, R.E. Dickinson, and Z.-L. Yang, 2002: The Land Surface Climatology of the Community Land Model coupled to the NCAR Community Climate Model. *J. Climate*, **15,** 1115-1130.

Boone, A., F. Habets, J. Noilhan, D. Clark, P. Dirmeyer, S. Fox, Y. Gusev, I. Haddeland, R. Koster, D. Lohmann, S. Mahanama, K. Mitchell, O. Nasonova, G.-Y. Niu, A. Pitman, J. Polcher, A.B. Shmakin, K. Tanaka, B. van den Hurk, S. Vérant, D. Verseghy, P. Viterbo, and Z.-L. Yang, 2004: The Rhône-aggregation land surface scheme intercomparison project: an overview. *J. Clim*., **17**, 187-208.

Briegleb, B. P., 1992: Delta-Eddington approximation for solar radiation in the NCAR community climate model. *J. Geophys. Res*., **97**, 7603-7612.

Chaumerliac, N., E. Richard, and R. Rosset, 1991: Impact of two microphysical schemes upon gas scavenging and deposition in a mesoscale meteorological model. *J. Appl. Meteor*., **30**, 88-97.

Chen, F., K. Mitchell, J. Schaake, Y. Xue, H.-L. Pan, V. Koren, Q.Y. Duan, M. Ek, and A. Betts, 1996: Modeling of land surface evaporation by four schemes and comparison with FIFE observations. *J. Geophys. Res*., **101D**, 7251-7268.

Chen, T.H., A. Henderson-Sellers, P.C.D. Milly, A.J. Pitman, A.C.M. Beljaars, J. Polcher, F. Abramopoulos, A. Boone, S. Chang, F. Chen, Y. Dai, C.E. Desborough, R. E. Dickinson, L. Dümenil, M. Ek, J.R. Garratt, N. Gedney, Y.M. Gusev, J. Kim, R. Koster, E.A. Kowalczyk, K. Laval, J. Lean, D. Lettenmaier, X. Liang, J.-F. Mahfouf, H.-T. Mengelkamp, K. Mitchell, O.N. Nasonova, J. Noilhan, A. Robock, C. Rosenzweig, J. Schaake, C. A. Schlosser, J.-P. Schulz, Y. Shao, A.B. Shmakin, D.L. Verseghy, P. Wetzel, E.F. Wood, Y. Xue, Z.-L. Yang, and Q. Zeng, 1997: Cabauw experimental results from the Project for Intercomparison of Land-Surface Parameterization Schemes. *J. Climate*., **10**, 1194-1215.

Chen, F., and J. Dudhia, 2001: Coupling an advanced land surface hydrology model with the Penn State/NCAR MM5 modeling system. Part 1: Model description and implementation. *Mon. Wea. Rev.,* **129**, 569-586.

Clapp, R.B., and G.M. Hornberger, 1978: Empirical equations for some soil hydraulic properties. *Water Resour. Res*., **14**, 601-604.

Claussen, M., 1988: On the surface energy budget of coastal zones with tidal flats. *Contr. Phys. Atmos.*, **61**, 39-49.

Colle, B.A., C.F. Mass, and K.J. Westrick, 2000: MM5 precipitation verification over the Pacific northwest during the 1997-99 cool seasons. *Wea. Forecast*., **15**, 730-744.

Colle, B.A., J.B. Olson, and J.S. Tongue, 2003: Multiseasonal verification of the MM5. Part II: Evaluation of high-resolution precipitation forecasts over the United States. *Wea. Forecast*., **18**, 458-480.

Cosby, B.J., G.M. Hornberger, R.B. Clapp, and T.R. Ginn, 1984: A statistical exploration of the relationships of soil moisture characteristics to the physical properties of soils. *Water Resour. Res*. **20**, 682-690.

Deardorff, J.W., 1978: Efficient prediction of ground surface temperature and moisture, with inclusion of a layer of vegetation. *J. Geophys. Res*., **84C**, 1889-1903.

de Groot, S.R., 1951: *Thermodynamics of irreversible processes*. New York. Intersci. Publ., 242 pp.

de Vries, D.A., 1958: Simultaneous transfer of heat and moisture in porous media. *T. Amer. Geophys. Union*., **39,** 909-916.

Dudhia, J., 1993: A non-hydrostatic version of the Penn State NCAR mesoscale model: validation tests and simulation of an Atlantic cyclone and cold front. *Mon. Wea. Rev*., **121,** 1493-1513.

Ek, M.B., K.E. Mitchell, Y. Lin, E. Rogers, P. Grunmann, V. Koren, G. Gayno, and J.D. Tarley, 2003: Implmentation of Noah land surface model advances in the National

Ceneters for Environmental Prediction operational mesoscale Eta model. *J. Geophys. Res*. **108**, D22, 8851, doi:10.1029/2002JD3296.

Eppel, D.P., H. Kapitza, M. Claussen, D. Jacob, W. Koch, L. Levkov, H.T. Mengelkamp, and N. Werrmann, 1995: The non-hydrostatic mesoscale model GESIMA: Part II. Parameterizations and applications. *Contrib. Atmos. Phys*., **68,** 15-41.

Fröhlich, K., and N. Mölders, 2002: Investigations on the impact of explicitly predicted snow metamorphism on the micro climate simulated by a meso-β/γ-scale non-hydrostatic model. *Atmos. Res*., **62,** 71-109.

Garand, L., 1983: Some improvements and complements to the infrared emissivity algorithm including a parameterization of the absorption in the continuum region. *J. Atmos. Sci.*, **40**, 230-244.

Giorgi, F., and R. Avissar, 1997: Representation of heterogeneity effects in earth system modeling: Experience from land surface modeling. *Rev. Geophys*. **35**, 413-438.

Grell, G., Y.-H. Kuo, and R. J. Pasch, 1991: Semi-prognostic tests of cumulus parameterization schemes in the middle latitudes. *Mon. Wea. Rev*., **119**, 5-31.

Grell, G., J. Dudhia, and D. Stauffer, 1994: A description of the Fifth-Generation Penn State/NCAR Mesoscale Model (MM5) NCAR/TN. 398 + STR.

Gutman G., A. Ignatov, 1998: The derivation of the green vegetation fraction from NOAA/AVHRR data for use in numerical weather prediction models. *Int. J. Rem. Sens.*, **19**, 1533-1543.

Henderson-Sellers, A., Z.-L. Yang, and R.E. Dickinson, 1993: The project for intercomparison of Land-surface Parameterization Schemes. *Bull. Amer. Meterol. Soc.,* **74,** 1335-1349.

Henderson-Sellers, A., J. Verner, and A.J. Pitman 1995: Comprehensibility of PIPLS (Project for the Intercomparison of Land surface Parameterization Schemes) codes. *J. Climate.,* **8,** 1043-1059.

Hong, S.-Y., and H.-L. Pan, 1996: Nonlocal boundary layer vertical diffusion in a medium-range forecast model. *Mon. Wea. Rev.,* **124,** 2322-2339.

Kapitza, H., and D.P. Eppel, 1992: The non-hydrostatic mesoscale model GESIMA: Part I. Dynamical equations and tests. *Contrib. Phys. Atmos*., **65,** 129-146.

Kongoli, C.E., and W.L. Bland, 2000: Long-term snow depth simulations using a modified atmosphere-land exchange model. *Agric. For. Meteorol*., **104,** 273-287.

Kotroni, V., and K. Lagouvardos, 2001: Precipitation forecast skill of different convective parameterization and microphysical schemes: application for the cold season over Greece. *Geophysical Research Letters*, **20**, 1977-1980.

Kramm, G., 1995: *Zum Austauch von Ozon und reaktiven stickstoffverbindungen zwischen Atmospheare und Biosphäre*. Frankfurt, Maraun-Verlag, p 268.

Kramm, G., N. Beier, T. Foken, H. Müller, P. Schroeder, and W. Seiler, 1996: A SVAT scheme for NO, NO_2, and O_3 – model description. *Meteorol. Atmos. Phys*., **61,** 89-106.

Leung, L.R., and S.J. Ghan, 1995: A subgrid parameterization of orographic precipitation. *Theoret. Appl. Met.,* **47**, 95-118.

Ling, F., and T. Zhang, 2003: Impact of the timing and duration of seasonal snow cover on the active layer and permafrost in the Alaskan Arctic. *Permafrost Periglac. Process.*, **14**, 141-150.

Loth, B., and H.-F. Graf, 1998: Modeling the snow cover in climate studies 1. Long-term integrations under different climatic conditions using a multilayered snow-cover model. J. Geophys. Res, **103D**, 11313-11327.

Lou, L., A. Robock, K.Y. Vinnakov, C.A. Schlosser, A.G. Slater, A. Boone, H. Braden, P. Cox, P. De Rosnay, R.E. Dickinson, Y. Dai, Q. Duan, P. Etchevers, A. Henderson-Sellers, N. Gedney, Y.M. Gusev, F. Habets, J. Kim, E. Kowalczyk, K. Mitchell, O.N. Nasonova, J. Nilhan, A.J. Pitman, J. Schaake, A.B. Shmakin, T.G. Smirnova, P. Wetzel, Y. Xue, Z.-L. Yang, and Q.-C. Zeng, 2003: Effects of frozen soil on soil temperature, spring infiltration, and runoff: Results from the PILPS 2(d) experiment at Valdai, Russia. *J. Hydrometeorol*., **4,** 334-351.

Mölders, N., H. Hass, H.J. Jakobs, M. Laube, and A. Ebel, 1994: Some effects of different cloud parameterizations in a mesoscale model and a chemistry transport model. *J. Appl. Meteor.*, **33**, 527-545.

Mölders, N., and M. Laube, 1994: A numerical study on the influence of different cloud treatment in a chemical transport model on gas phase distribution. *Atmos. Res.*, **32**, 249-272.

Mölders, N., M. Laube, and G. Kramm, 1995: On the parameterization of ice microphysics in a mesoscale α weather forecast model. *Atmos. Res*., **38**, 207-235.

Mölders, N., and A. Raabe, A., 1996. Numerical investigations on the influence of subgrid-scale surface heterogeneity on evapotranspiration and cloud processes. *J. Appl. Meteor.* **35**, 782-795.

Mölders, N., 2000: HTSVS – A new land-surface scheme for MM5. In *The tenth PSU/NCAR Mesoscale model users' workshop*., 33-35 (available from NCAR, P.O. Box 3000, Boulder, CO 80307, USA or http://www.mmm.ucar.edu/mm5/mm5.html)

Mölders, N., 2001: On the uncertainty in mesoscale modeling caused by surface parameters. *Meteor. Atmos. Phys*. **76**, 119-141.

Mölders, N., and W. Rühaak, 2002: On the impact of explicitly predicted runoff on the simulated atmospheric response to small-scale land-use changes – an integrated modeling approach. *Atmos. Res*., **63,** 3-38.

Mölders, N., U. Haferkorn, J. Döring, and G. Kramm, 2003a: Long-term investigations on the water budget quantities predicted by the hydro-thermodynamic soil vegetation scheme (HTSVS) – Part I: Description of the model and impact of long-wave radiation, roots, snow and soil frost. *Meteorol. Atmos. Phys*., **84,** 15-135.

Mölders, N., U. Haferkorn, J. Döring, and G. Kramm, 2003b: Long-term investigations on the water budget quantities predicted by the hydro-thermodynamic soil vegetation scheme (HTSVS) – Part II: Evaluation, sensitivity, and uncertainty. *Meteorol. Atmos. Phys*., **84,** 137-156.

Mölders, N., and J.E. Walsh, 2004: Atmospheric response to soil frost and snow in Alaska in March. *Theor. Appl. Climatol*., **77,** 77-115.

Mölders, N., and V.E. Romanovsky, 2005: Long-term evaluation of HTSVS' frozen ground/permafrost component using observations at Barrow, Alaska, IARC cooperative agreement quarterly report to NSF.

Pielke, R.A. 1984. *Mesoscale Meteorological Modellin*g. Academic Press, Inc., London, p. 612

Philip, J.R., 1957: Evaporation, and moisture and heat fields in the soil. *J. Meteorol*., **14,** 354-366.

Philip, J.R., and D.A. de Vries, 1957: Moisture in porous materials under temperature gradients. *Trans. Amer. Geophys. Soc*., **18,** 222-232.

Prigogine, I., 1951: Introduction to thermodynamics of irreversible processes. *Intersci. Publ. New York, London*, 242 pp.

Raschke, E., U. Karstens, R. Nolte-Holube, R. Brandt, H.-J. Isemer, D. Lohmann, M. Lobmeyer, B. Rockel and R. Stuhlmann, 1998: The Baltic sea experiment BALTEX: a brief overview and some selected results of the authors. *Geophysics*, **19**, 1-22.

Rassmussen, R.M., I. Geresdi, G. Thompson, K. Manning, and E. Karplus, 2002: Freezing drizzle formation in stably stratified layer clouds: the role of radiative cooling of cloud droplets, cloud condensation nuclei, and ice initiation. *J. Atmos. Sci*.**, 59**, 837-860.

Reisner, J., R.J. Rasmussen, and T. Bruintjes, 1998: Explicit forecasting of supercooled liquid water in winter storms using the MM5 mesoscale model. *Quart. J. Roy. Meteorol. Soc*., **124B,** 1071-1107.

Robock, A., K.Y. Vinnikov, and C.A. Schlosser, 1997: Evaluation of land-surface parameterization schemes using observations. *J. Climate*, **10**, 377-379.

Schlosser, C.A., A.G. Slater, A. Robock, A.J. Pitman, Y.V. Konstantin, A. Henderson-Sellers, N.A. Speranskaya, and K. Mitchell, 2000: Simulation of a Boreal Grassland Hydrology at Valdai, Russia. PLPS Phase 2(d), *Mon. Wea. Rev*., **128**, 301-321.

Schultz, P., 1995: On explicit cloud physics parameterization for operational numerical weather prediction. *Mon. Wea. Rev*., **123,** 3321-3343.

Sellers, P., Y. Mintz, Y. Sud, and A. Dalcher, 1986: A simple Biosphere (SiB) for use within General Circulation Models. *J. Atmos. Sci.*, **43,** 505-531

Seth, A., F. Giorgi, and R.E. Dickinson, 1994: Simulating fluxes from heterogeneous land surfaces: explicit subgrid method employing the biosphere-atmosphere transfer scheme (BATS). *J. Geophys. Res.,* **99** D9, 18651-18667.

Slater, A.G., A.J. Pitman, and C.E. Desborough, 1998: The validation of a snow parameterization designed for use in general circulation models. *Int. J. Climatol*., **18,** 595-617.

Stephens, G.L., 1978: Radiation profiles in extended water clouds, Part II. Parameterization schemes. *J. Atmos.Sci.,* **35,** 2123-2132.

Stephens, G.L., 1984: The parameterization of radiation for numerical weather predication and climate models. *Mon. Wea. Rev.,* **114,** 1330-1339.

Sturm, M., J. Holmgren, M. König, and K. Morris, 1997: The thermal conductivity of seasonal snow. *J. Glaciology*, **43**, 26-41.

Thompson, G., R.M. Rasmussen, and K. Manning, 2004: Explicit forecasts of winter precipitation using an improved bulk microphysics scheme. Part I: Description and sensitivity analysis. *Mon. Wea. Rev*., **132**, 519-542.

Verseghy, D.L., 1991: CLASS – A Canadian land surface scheme for GCMs. I. Soil model. *Int. J. Climatol*., **11**, 111-133.

Wood, E.F., D.P. Lettenmaier, X. Liang, D. Lohmann, A. Boone, S. Chang, F. Chen, Y. Dai, R.E. Dickinson, Q. Duan, M. Ek, Y.M. Gusev, F. Habets, P. Iraanejad, R. Koster, K.E. Mitchel, O.N. Nasonova, J. Noilhan, J. Schaake, A. Schlosser, Y. Shao, A.B. Shmakin, D. Verseghy, K. Warrach, P. Wetzel, Y. Xue, Z.-L. Yang, and Q.-C. Zeng, 1998: The Project for Intercomparison of Land-surface Parameterization Schemes (PILPS) Phase 2(c) Red-Arkansas river basis experiment: 1. Experiment description and summary intercomparisons. *Global and Planetary Change*, **19**, 115-135.

Yang, Z.L., R.E. Dickinson, A. Robock, and K.Y. Vinnikov, 1997: On validation of the snow sub-model of the Biosphere-Atmosphere Transfer Scheme with Russian snow cover and meteorological observational data. *J. Climate*, **10,** 353-373.

Zhong, S., H.-J. X. Bian, J. Charney, W. Heilman, and B. Potter, 2005: Evaluation of real-time high-resolution MM5 predictions over the Great Lakes region. *Mon. Wea. Rev*., **20**, 63-81.

1.8 Figure captions

Fig. 1. Terrain data as used in the model and schematic view of model domain location as well as location of snow sites indicated by * and soil temperature sites in Belarus (53-57^{o}N, 25-30^{o}E) indicated by gray dots, and in Germany (50-55^{o}N; 5-15^{o}E) indicated by black dots used for evaluation. Contour lines of elevation are at 0, 200, 600 and 1000m, respectively.

Fig. 2. Comparison of terminal velocity as obtained by the Schultz and Reisner schemes at various snow-mixing ratios.

Fig. 3. Comparison of observed (gray dots) and predicted (contour lines) 120h accumulated precipitation given as water equivalent (mm) as obtained by (a) SC, (b) RC, (c) SL, and (d) RL. Light gray: 0mm, medium gray: greater than 0 but less than 1mm, dark gray: greater than or equal to 1 but less than 2mm, and black: equal to or greater than 2mm. White areas mean that there were no precipitation data available.

Fig. 4. Comparison of (a) sea level pressure distribution (hPa), (b) surface air temperature distribution (K), and (c) specific humidity (g/kg) as obtained for RL (solid lines) and from reanalysis (dashed lines) on April 26 0000UT. Note that distributions for SC, RC, and SL look similar.

Fig. 5. Temporal evolution of RMSE for (a) air temperature and (b) wind speed in the first layer above ground as obtained for the four simulations.

Fig. 6. Comparison of simulated and observed snow depth as obtained for RL. Note that scatter plots for SC, RC, and SL hardly differ from this figure.

Fig. 7. Temporal evolution of RMSE and average absolute difference in simulated and observed snow depth as obtained by the four simulations. Note that scores for water equivalents are about one order less than those of snow depth shown in the graphs.

Fig. 8. Event scores of CSD determined over the entire episode as obtained for (a) SC, (b) RC, (c) SL, and (d) RL. In the legend, the first and second logical correspond to the observations and the simulations, respectively. Yes-yes means change in snow depth is observed and simulated (N_1), no-yes not observed, but simulated (N_2), yes-no observed, but not simulated (N_3), and no-no not observed and (correctly) not simulated (N_4).

Fig. 9. BIAS and accuracy of total change in snow depth (upper part), increase in snow depth (middle), and decrease in snow depth (lower part) as obtained for the four simulations.

Fig. 10. Temporal decrease of snow depth by compaction and settling only as obtained for various initial snow densities of a 2m thick snow pack.

Fig. 11. Comparison of simulated and observed daily averaged soil temperatures as obtained with RL. Results for SL, RL and RC marginally differ from the ones shown here. Note that the relatively higher temperatures correspond to soil layers close beneath the surface, while relatively lower temperatures occur deeper in the soil.

Fig. 12. Comparison of simulated and observed diurnal pattern of soil temperatures averaged over all 20 German stations as obtained by (a) SC and (b) RL. Note that figures for RC and SL look similar to SC and RL, respectively.

1.9 Table captions

Table 1. Summary of the parameterization and initialization methods used in the different simulations of this study.

Table 2. Soil characteristics assumed in our study. Here, k_s, η_s, b, ψ_s and $c_S\rho_S$ are the saturated hydraulic conductivity, volumetric water content at saturation (porosity), pore-size distribution index, water potential at saturation, and volumetric heat capacity of the dry soil material. Parameters are from Clapp and Hornberger (1978), Cosby et al. (1984), Pielke (1984), and Chen and Dudhia (2001).

Table 3. RMSE as obtained for the various simulations. Results include the 20 German (three observations per site per day) and five Belarusian (daily average per site each day) sites. RMSEs are valid for the 5d episode.

Figures

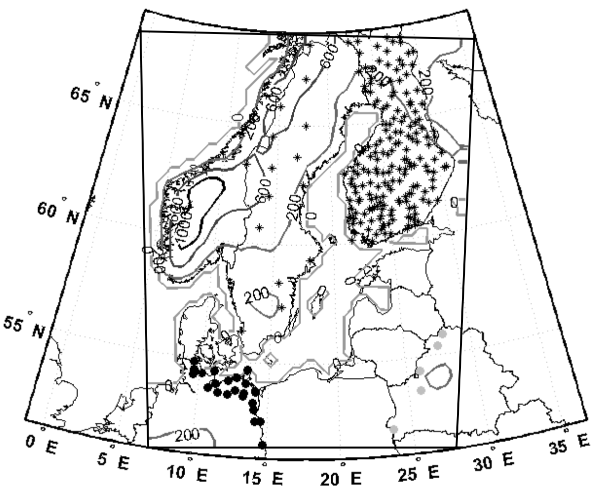

Figure 1. Terrain data as used in the model and schematic view of model domain location as well as location of snow sites indicated by * and soil temperature sites in Belarus (53-57°N, 25-30°E) indicated by gray dots, and in Germany (50-55°N; 5-15°E) indicated by black dots used for evaluation. Contour lines of elevation are at 0, 200, 600 and 1000m, respectively.

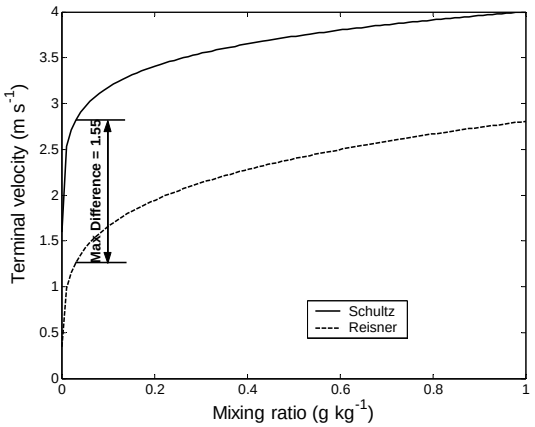

Figure 2. Comparison of terminal velocity as obtained by the Schultz and Reisner scheme at various snow-mixing ratios.

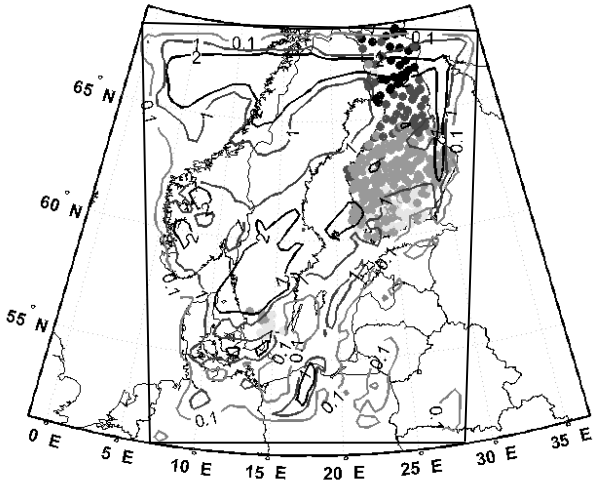

Figure 3. Comparison of observed (gray dots) and predicted (contour lines) 120h accumulated precipitation given as water equivalent (mm) as obtained by (a) SC, (b) RC, (c) SL, and (d) RL. Light gray: 0mm, medium gray: greater than 0 but less than 1mm, dark gray: greater than or equal to 1 but less than 2mm, and black: equal to or greater than 2mm. White areas mean that there were no precipitation data available.

(a)

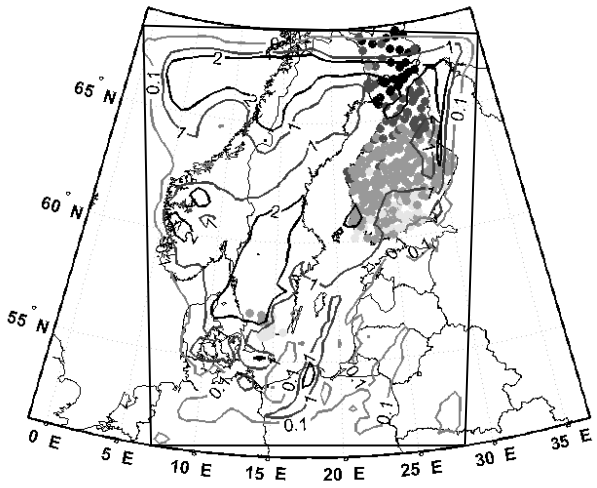

(b)

Fig. 3 continued

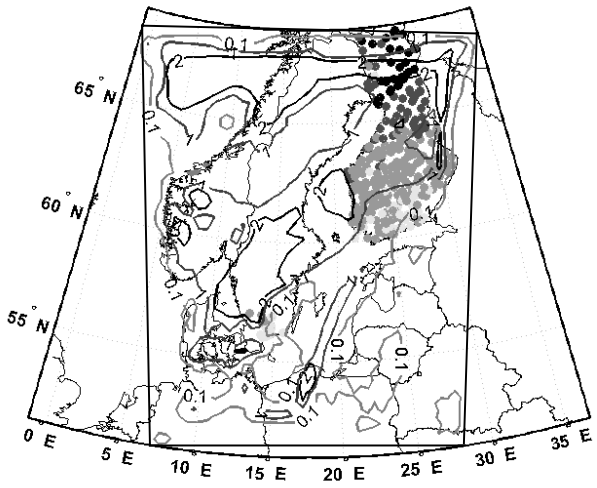

(c)

Fig. 3 continued

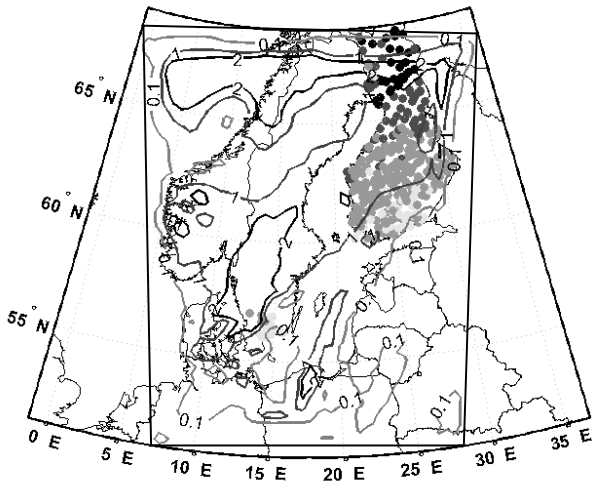

(d)

Fig. 3 continued

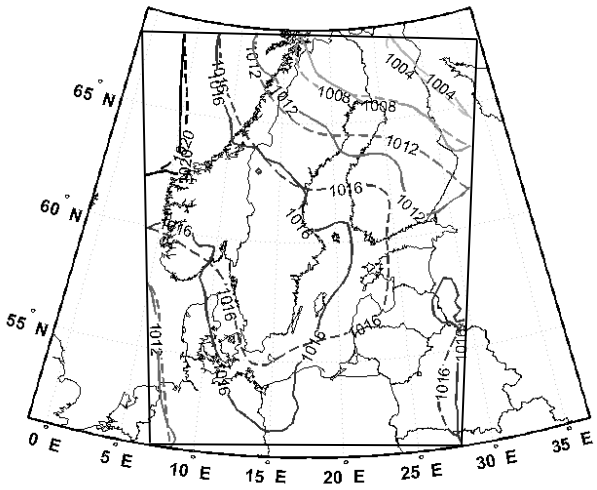

Figure 4. Comparison of (a) sea level pressure distribution (hPa), (b) surface air temperature distribution (K), and (c) specific humidity (g/kg) as obtained for RL (solid lines) and from reanalysis (dashed lines) on April 26 0000UT. Note that distributions for SC, RC, and SL look similar.

(a)

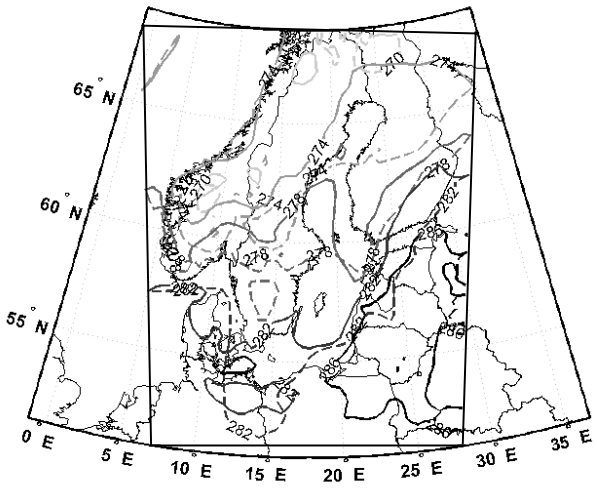

(b)

Fig. 4 continued

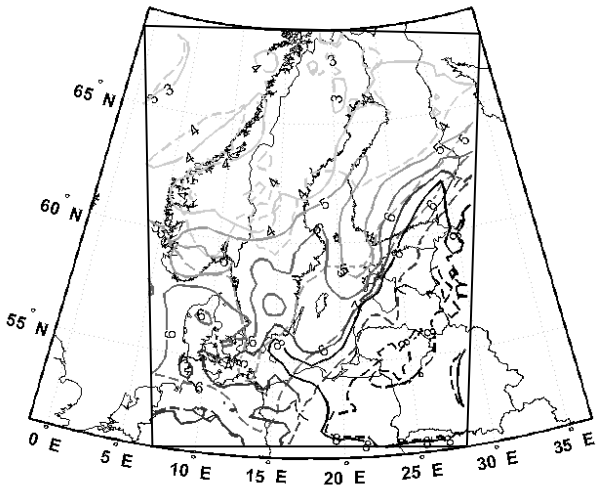

(c)

Fig. 4 continued

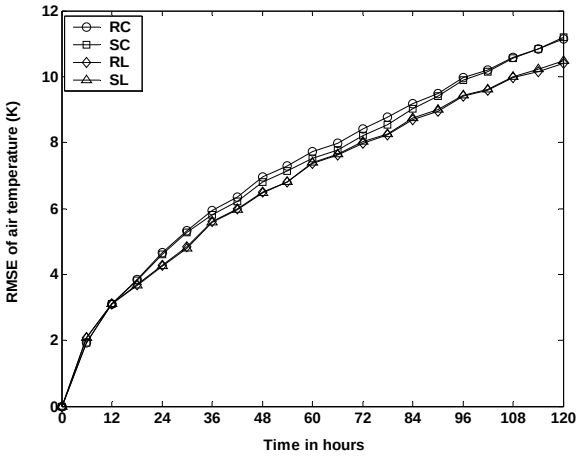

Figure 5. Temporal evolution of RMSE for (a) air temperature and (b) wind speed in the first layer above ground as obtained for the four simulations.

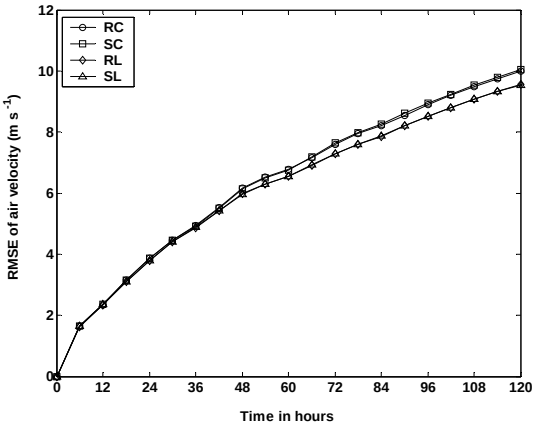

(b)

Fig. 5 continued

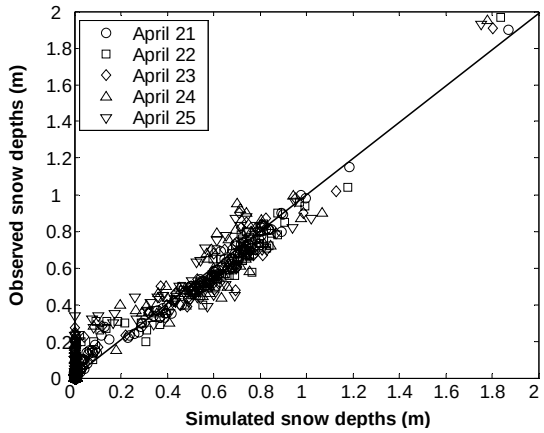

Figure 6. Comparison of simulated and observed snow depth as obtained for RL. Note that scatter plots for SC, RC, and SL hardly differ from this figure.

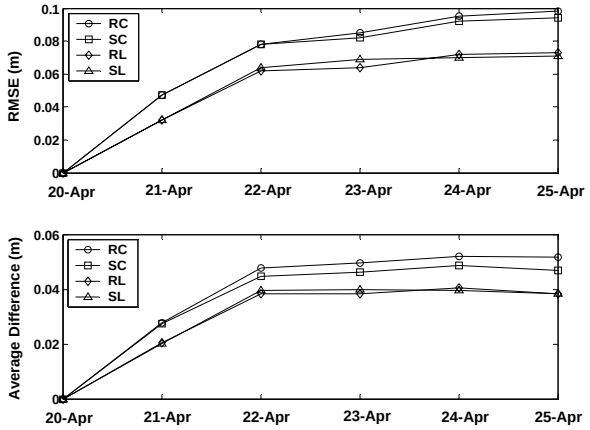

Figure 7. Temporal evolution of RMSE and average absolute difference in simulated and observed snow depth as obtained by the four simulations. Note that scores for water equivalents are about one order less than those of snow depth shown in the graphs.

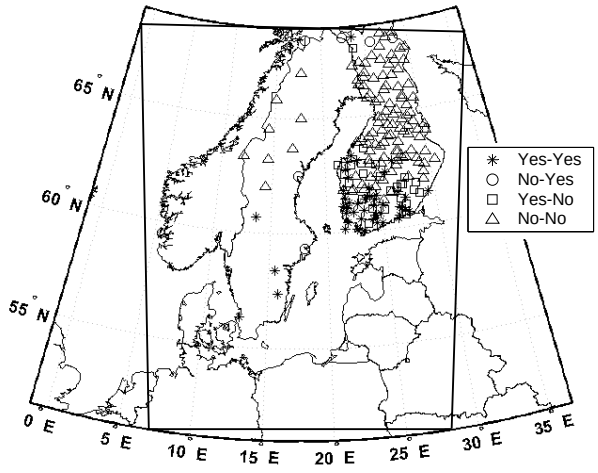

Figure 8. Event scores of CSD determined over the entire episode as obtained for (a) SC, (b) RC, (c) SL, and (d) RL. In the legend, the first and second logical correspond to the observations and the simulations, respectively. Yes-yes means change in snow depth is observed and simulated (N_1), no-yes not observed, but simulated (N_2), yes-no observed, but not simulated (N_3), and no-no not observed and (correctly) not simulated (N_4).

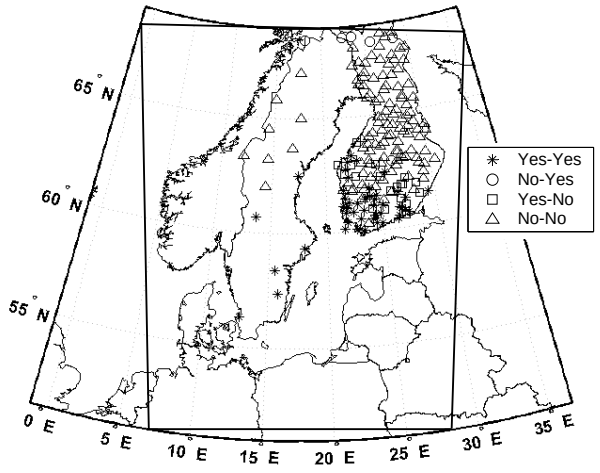

(b)

Fig. 8 continued

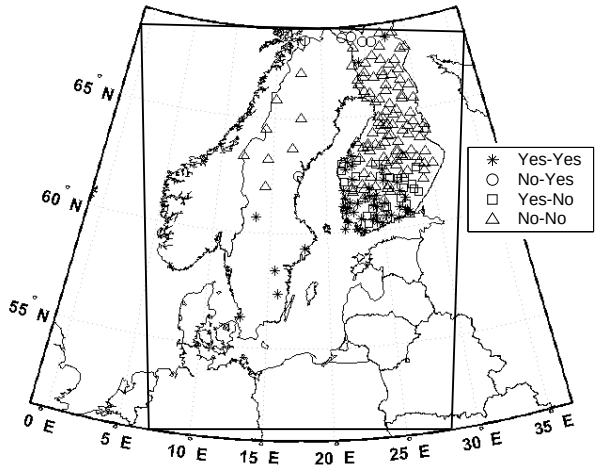

(c)

Fig. 8 continued

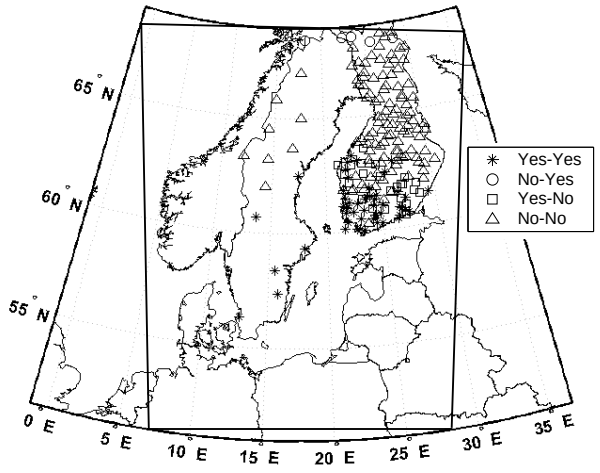

(d)

Fig. 8 continued

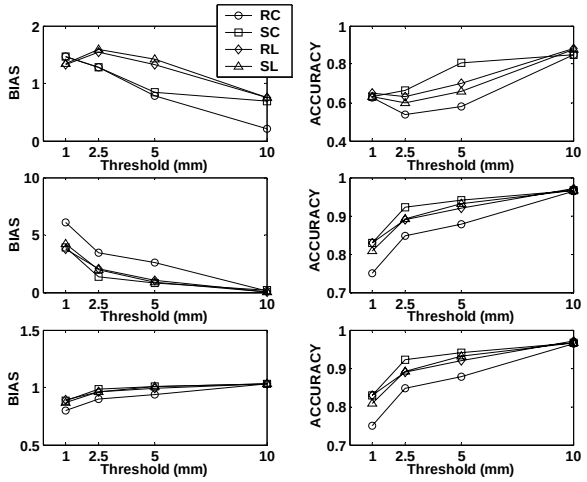

Figure 9. BIAS and accuracy of total change in snow depth (upper part), increase in snow depth (middle), and decrease in snow depth (lower part) as obtained for the four simulations.

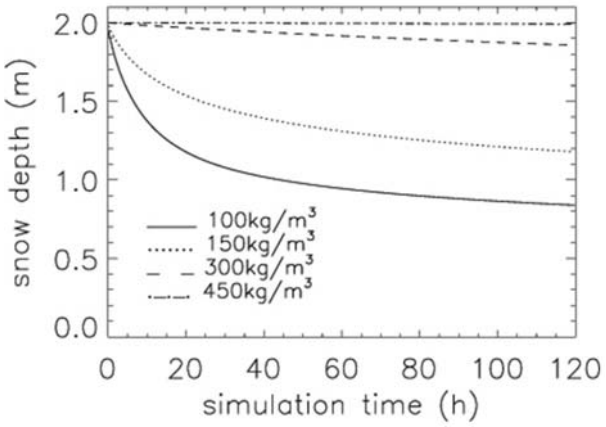

Figure 10. Temporal decrease of snow depth by compaction and settling only as obtained for various initial snow densities of a 2m thick snow pack.

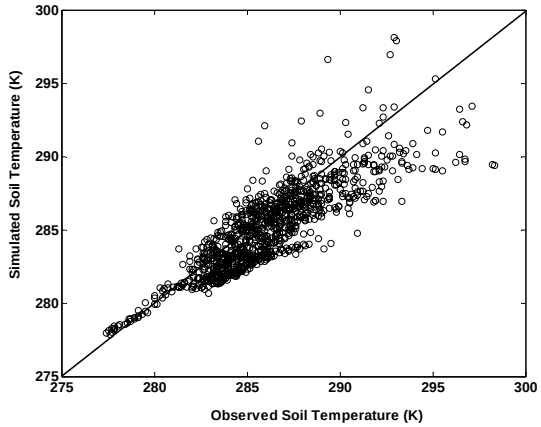

Figure 11. Comparison of simulated and observed daily averaged soil temperatures as obtained with RL. Results for SL, RL and RC marginally differ from the ones shown here. Note that the relatively higher temperatures correspond to soil layers close beneath the surface, while relatively lower temperatures occur deeper in the soil.

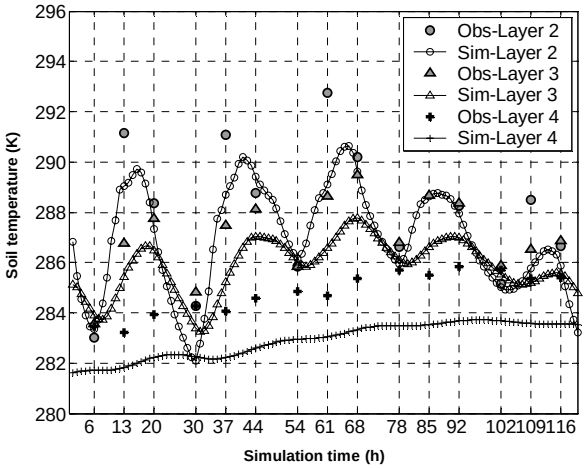

Figure 12. Comparison of simulated and observed diurnal pattern of soil temperatures averaged over all 20 German stations as obtained by (a) SC and (b) RL. Note that figures for RC and SL look similar to SC and RL, respectively.

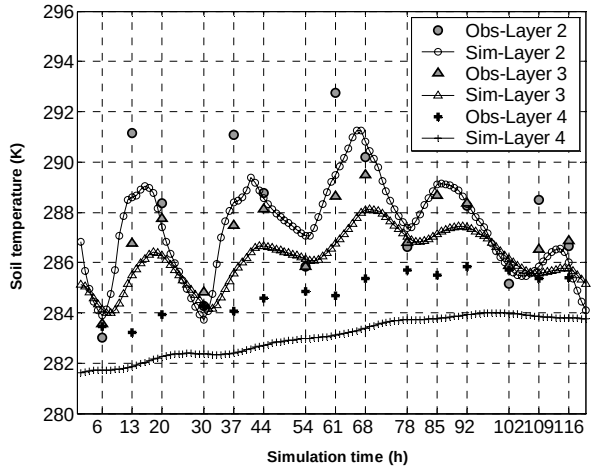

(b)

Fig. 12 continued

Tables

Simulation Name	Reisner	Schultz	CCM2	CLOUD
SC		**X**	**X**	
RC	**X**		**X**	
SL		**X**		**X**
RL	**X**			**X**

Table 1. Summary of the parameterization and initialization methods used in the different simulations of this study.

Soil-type	k_s 10^{-4} m/s	η_s m^3/m^3	b -.-	ψ_s m	$c_S\rho_S$ $10^6 Jm^{-3}K^{-1}$	ε_g -.-
loamy sand	1.563	0.410	4.38	-0.090	1.41	0.95
sandy loam	0.341	0.435	4.90	-0.218	1.34	0.95
loam	0.070	0.451	5.39	-0.478	1.21	0.95

Table 2. Soil characteristics assumed in our study. Here, k_s, η_s, b, ψ_s and $c_S\rho_S$ are the saturated hydraulic conductivity, volumetric water content at saturation (porosity), pore-size distribution index, water potential at saturation, and volumetric heat capacity of the dry soil material. Parameters are from Clapp and Hornberger (1978), Cosby et al. (1984), Pielke (1984), and Chen and Dudhia (2001).

	Root Mean Square Errors (K)					
	layer 1	layer 2	layer 3	layer 4	layer 5	All layers
RC	2.2	1.7	1.6	0.3	0.3	1.2
SC	2.0	1.4	1.5	0.5	0.2	1.1
RL	1.5	1.0	1.3	0.3	0.3	0.9
SL	1.5	1.1	1.3	0.5	0.2	0.9

Table 3. RMSE as obtained for the various simulations. Results include the 20 German (three observations per site per day) and five Belarusian (daily average per site each day) sites. RMSEs are valid for the 5d episode.

Chapter 2

Implementation of a Galerkin Weak Finite Element scheme for the soil model of the Hydro-Thermodynamics Soil Vegetation Scheme (HTSVS)

2.1 Abstract

Galerkin Weak Finite Element (GWFE) scheme has been implemented into the Hydro-Thermodynamic Soil-Vegetation scheme (HTSVS)'s soil model to be used alternatively to the existing Crank-Nicholson Finite Difference (CNFD) scheme. The new numerical method has been evaluated by data from three sites around Council, Alaska and its performance has been compared with that of CNFD. The re-written Partial Differential Equations (PDEs) of HTSVS' soil model is used to recognize the cell Peclet values, by which advection and diffusion regimes in the soil layers are distinguished. Cell Peclet values ranged from 0.01 to 1.0 characterizing former as diffusion and later as moderately advection regimes. The new numerical scheme's performance strongly depends on the soil regime and the starting time of the simulations. The GWFE method well captures the soil temperatures in relatively higher Peclet regimes with right phase of temperature peaks, non-diffused and non-oscillatory nature compared with CNFD. The acceptable results obtained by CNFD under the diffusion dominated regimes and the lower CPU times as compared to GWFE suggest that the former method is acceptable for lower cell Peclet number soil regimes. CNFD scheme underestimates the soil moisture in the advection regimes and hence further diffuse the resultant soil temperatures due to the coupling of cross effects presented between volumetric water content and temperature in the soil model, while GWFE gains particular advantage in this situation. It is found that

during later days of spring season, the cell Peclet gains relatively higher than during winter and summer.

2.2 Introduction

In mid latitude winter, at high elevation and in the active layer of Arctic and sub Arctic soils, freezing and thawing occur seasonally. The freezing/thawing processes mean a discontinuity of soil water content. Frozen ground has a direct effect on infiltration and an indirect effect on heat transfer in the soil beneath (e.g. Cherkauer and Lettenmaier, 1999), and hence freezing/thawing also effect soil heat and moisture fluxes.

Accurate prediction of the earth's surface state variables, soil temperature and moisture is a key component of agrimeteorological applications and climate system modeling (e.g. Robock et al., 1997). These conditions are typically described by soil models embedded in the climate or agrimeteorological models (e.g. Dickinson et al., 1993; Robock et al., 1995; Huang et al., 1996). Soil models usually consist of algebraic and partial differential equations (PDEs) of the physical processes use accepted theories that are solved by numerical schemes (e.g. Jacobson, 1999; Pielke, 2001). Therefore, it is necessary to incorporate the high order accurate and non-oscillatory numerical schemes for the soil physical equations to be solved.

During the freeze-thaw cycles, there exist many discontinuities in the soil with respect to frozen ground and liquid water, because of the fact that the soil ice and liquid water may coexist. In a typical Arctic/ sub Arctic region, in summer the freezing line typically shows a strong diurnal cycle in the active layer, and accurate prediction of the freezing line may play a key role in determining soil temperatures and soil moistures as

well as surface energy and water fluxes (e.g. Montaldo and Albertson, 2001; Lou et al., 2003). The interface frozen ground versus unfrozen ground means a steep discontinuity with respect to soil liquid water content and soil water fluxes. At this interface, great temperature changes occur due to release of latent heat or consumption of heat.

The project of intercomparison of land surface schemes (PILPS) (e.g. Shao and Henderson-Sellers, 1996; Luo et al., 2003) illustrated the difficulties and limitations of current state-of-the-art soil models in the treatment of nonlinear coupled partial differential equations to strike the balance between the complexity of the algorithms, parameterizations, and predictability. Results show an average uncertainty of 200 mm in soil moisture simulations among the schemes tested. This study and other studies (e.g., Wetzel and Boone, 1995) concluded to favor the more physically based models. Capturing the depth of the freezing front is important because temperature variations diminish throughout a great extent in the soil below (Luo et al., 2003). Another difficulty in soil modeling is the appropriate usage of a suitable numerical scheme to discretize the PDEs. Typically finite differences (FD) schemes are used (e.g. McCumber and Pielke, 1981; Kramm et al., 1996). It is well known that such schemes often have difficulties at discontinuities like the freeze-thaw line (e.g. Mölders and Romonovsky, 2005). Once frozen ground is thawed it acts as porous media and allows water to percolate. The advection of water enhances the soil heat capacity, and thus one has to consider advection-diffusion PDE to estimate for soil water content. Hence modeling frozen ground can be seen as a two-fold problem, namely to correctly predict the depth of the

freezing line, and calculate soil heat and water fluxes when the ground nearly turns into a porous media.

Thus, recently a physically advanced algorithm is implemented into the multi-layer soil model of the Hydro-Thermodynamic Soil-Vegetation Scheme (HTSVS; Kramm et al., 1996) is enlarged by a component to component soil freezing/thawing to predict the soil temperatures and moistures more accurately in freezing and thawing soils(e.g. Mölders et al., 2003a). Evaluation studies showed that HTSVS successfully predicts surface fluxes and soil conditions (e.g., Kramm, 1995; Mölders, 2000; Narapusetty and Mölders, 2005), the water supply to the atmosphere and ground water recharge on the long-term as well as soil temperatures, even if frozen ground occurs (e.g. Mölders et al. 2003a, 2003b). Discrepancies around the freeze-thaw line are about 2-4K (e.g. Mölders and Romonovsky, 2005). Soil water advection lowers during freeze and rises along a thaw process. Hence a numerical scheme which can capture the low and high advection dominated advection-diffusion regime is needed to capture the soil temperatures and moistures during the freeze-thaw processes. A moderately advection dominated regime can be well captured without excessive computational burden using Galerkin-based finite element spatial approximation with suitable high order time discretization schemes, on the other hand, centered FD spatial approximation generates spurious oscillations in the numerical solution (e.g. Donea and Huerta, 2003). The applicability of FE for strong advection dominated regimes can be achieved by stabilization schemes such as streamline-upwind/Petrov-Galerkin (e.g. Hughes et al., 1987; Brooks and Hughes, 1982), Galerkin/least-squares (e.g. Hughes and Hulbert, 1988;

Shakib 1988; Hughes et al., 1989). However, the FE interpolation functions are discontinuous in time and hence prompt to solve the variables for one time-space slab each time, so it involves more computational burden than FE schemes (e.g. Tezduyar, 1992). Because of its relatively good computational efficiency a Galerkin- type of FE method (e.g. Oden 1972; Fletcher, 1984; Johnson, 1987) is implemented to solve the PDEs in the HTSVS's soil model. The usage of FD scheme to solve the PDEs when simulating the seasonally frozen soil is also compared against the FE scheme to document the advantages using this method.

2.3 Method

2.3.1) Short description of the soil model

HTSVS makes use of the principles of linear thermodynamics of irreversible processes, including the Richards-equation (e.g. Kramm et al., 1996) also considers the Ludwig-Soret and Dufour effects, which are important during freezing/thawing and snowmelt, and if chemical processes are involved and is recently enlarged to consider the effects of seasonally frozen soil and water uptake by roots (e.g. Mölders et al., 2003a, Mölders and Walsh, 2004). A detailed description of the parameterized algebraic equation sets, and the PDEs governing physical processes in HTSVS are given in Mölders et al. (2003a). The soil heat and moisture balance equations are given by (e.g. Philip and de Vries, 1957; de Vries 1958; Kramm, 1995; Kramm et al., 1996; Mölders et al. 2003a)

$$\frac{\partial \eta}{\partial t} = \frac{\partial}{\partial z}\left(\left(D_{\eta,v} + D_{\eta,w} \right) \frac{\partial \eta}{\partial z} + D_{T,v} \frac{\partial T_S}{\partial z} + K_W \right) - \frac{\chi}{\rho_W} - \frac{\rho_{ice}}{\rho_W} \frac{\partial \eta_{ice}}{\partial t} \qquad (1)$$

$$C\frac{\partial T_S}{\partial t} = \frac{\partial}{\partial z}\left(\left(\lambda + L_v\rho_W D_{T,v}\right)\frac{\partial T_S}{\partial z} + L_v\rho_W D_{\eta,v}\frac{\partial \eta}{\partial z}\right) + L_f\rho_{ice}\frac{\partial \eta_{ice}}{\partial t} \qquad (2)$$

Where η is volumetric water content, T_S is soil temperature, $D_{\eta,v}$, $D_{\eta,w}$ and $D_{T,v}$ are the transfer coefficients with respect to water vapor, water, and heat respectively. $K_W = K_{WS}W^c$ is the hydraulic conductivity, where K_{WS} is the saturated hydraulic conductivity, c = 2b+3 is the pore-disconnectness index and W= η/η_S is the relative volumetric water content with η_S being the porosity of the non-frozen soil. χ is the water uptake by roots per soil volume. The thermal conductivity λ is a function of water potential, parameterized in accordance with McCumber and Pielke (1981). For $T_S \le T_0$, a mass weighted thermal conductivity is calculated depending on the liquid and ice volumetric water content using the value obtained by the aforementioned equation of the liquid water, and a value of 2.31$Jm^{-1}s^{-1}K^{-1}$ for the pure ice fraction. L_f and L_v are the latent heat of fusion and vaporization, respectively. $C = (1-\eta_S)\rho_S c_S + \eta\rho_W c_W + \eta_{ice}\rho_{ice}c_{ice} + (\eta_S - \eta - \eta_{ice})\rho_a c_p$ is the volumetric heat capacity of moist soil, where $\rho_S, \rho_W, \rho_{ice}, c_S, c_W$ and c_{ice} are the density and specific heat of the dry soil material, water, and ice, respectively.

2.3.2) Original numerical scheme

The coupled PDEs (1) and (2) are solved using Crank-Nicholson scheme based on finite differences (CNFD) numerical scheme, in conjunction with a Gauss-Seidel iterating technique (e.g. Kramm, 1995; Kramm et al., 1996). A logarithmic coordinate

transformation is required for equal spacing of the grid to use a centered finite difference scheme. This means soil temperature and volumetric water content are predicted on a logarithmic grid with increasing spacing depth.

$$\frac{\eta^{j+1}-\eta^{j}}{\Delta t}=\Theta\left\{\vartheta_{11}\frac{\left[\eta_{,i+1}-2\eta_{,i}+\eta_{,i-1}\right]^{j+1}}{\Delta Z^{2}}+\vartheta_{12}\frac{\left[T_{S,i+1}-2T_{S,i}+T_{S,i-1}\right]^{j+1}}{\Delta Z^{2}}+\vartheta_{12}\frac{\left[K_{W,i+1}-K_{W,i-1}\right]^{j+1}}{2\Delta Z}\right\}$$
$$+(1-\Theta)\left\{\vartheta_{11}\frac{\left[\eta_{,i+1}-2\eta_{,i}+\eta_{,i-1}\right]^{j}}{\Delta Z^{2}}+\vartheta_{12}\frac{\left[T_{S,i+1}-2T_{S,i}+T_{S,i-1}\right]^{j}}{\Delta Z^{2}}+\vartheta_{12}\frac{\left[K_{W,i+1}-K_{W,i-1}\right]^{j}}{2\Delta Z}\right\}$$
$$+S_{1} \qquad (3),$$

and

$$\frac{T_{S}^{\,j+1}-T_{S}^{\,j}}{\Delta t}=\Theta\left\{\vartheta_{21}\frac{\left[T_{S,i+1}-2T_{S,i}+T_{S,i-1}\right]^{j+1}}{\Delta Z^{2}}+\vartheta_{22}\frac{\left[\eta_{,i+1}-2\eta_{,i}+\eta_{,i-1}\right]^{j+1}}{\Delta Z^{2}}\right\}$$
$$+(1-\Theta)\left\{\vartheta_{21}\frac{\left[T_{S,i+1}-2T_{S,i}+T_{S,i-1}\right]^{j}}{\Delta Z^{2}}+\vartheta_{22}\frac{\left[\eta_{,i+1}-2\eta_{,i}+\eta_{,i-1}\right]^{j}}{\Delta Z^{2}}\right\}$$
$$+S_{2} \qquad (4)$$

where $\vartheta_{11}=\left(D_{\eta,v}+D_{\eta,w}\right)$, $\vartheta_{12}=D_{T,v}$, $\vartheta_{21}=\frac{\left(\lambda+L_{v}\rho_{w}D_{T,v}\right)}{C}$, $\vartheta_{22}=\frac{L_{v}\rho_{w}D_{\eta,v}}{C}$,

$S_{1}=-\frac{\chi}{\rho_{W}}-\frac{\rho_{ice}}{\rho_{W}}\frac{\partial\eta_{ice}}{\partial t}$ and, $S_{2}=L_{f}\rho_{ice}\frac{\partial\eta_{ice}}{\partial t}$

Eqs. (3) and (4) are solved using Gauß-Seidel iteration technique with the convergence criteria imposed being 0.0001 m^3/m^3 on soil water content.

2.3.3) Proposed numerical scheme

To capture the discontinuities associated with freezing line during the freeze-thaw cycles, we incorporate a computationally advanced algorithm, the Galerkin finite element approach with linear elements. In doing so, equations (1) and (2) are re-written to resemble the standard transient convection-diffusion (TCD) equation (e.g. Tannehill et al., 1997),

$$\frac{\partial \Phi}{\partial t} + a\frac{\partial \Phi}{\partial z} - \vartheta\frac{\partial^2 \Phi}{\partial z^2} = S \tag{5}$$

Herein, Φ is any solution variable and, a, ϑ and, S are the advection velocity, viscosity coefficient, and source terms, respectively. The different advection and diffusion regimes within each element are recognized with a non dimensional cell Peclet number ($Pe = a * h/2\vartheta$), which compares the advection to diffusion regime (e.g. Donea and Huerta, 2003). Thus we obtain for volumetric water content

$$\frac{\partial \eta}{\partial t} + \left(-\frac{\partial}{\partial z}\left(D_{\eta,v} + D_{\eta,w}\right) - \frac{c}{\eta}K_w \right)\frac{\partial \eta}{\partial z} - \left(D_{\eta,v} + D_{\eta,w}\right)\frac{\partial^2 \eta}{\partial z^2} - \frac{\partial}{\partial z}\left(D_{T,v}\frac{\partial T_S}{\partial z} \right) = -\frac{\chi}{\rho_w} - \frac{\rho_{ice}}{\rho_w}\frac{\partial \eta_{ice}}{\partial t} - W^c\frac{\partial K_{ws}}{\partial z} - K_w \ln(W)\frac{\partial c}{\partial z} + K_w\frac{c}{\eta_S}\frac{\partial \eta_S}{\partial z} \tag{6}$$

with the advection velocity $a = \left(-\frac{\partial}{\partial z}\left(D_{\eta,v} + D_{\eta,w}\right) - \frac{c}{\eta}K_w \right)$, viscosity coefficients $\vartheta_{11} = \left(D_{\eta,v} + D_{\eta,w}\right)$ and, $\vartheta_{12} = D_{T,v}$, and, the source term

$$S_3 = -\frac{\chi}{\rho_w} - \frac{\rho_{ice}}{\rho_w}\frac{\partial \eta_{ice}}{\partial t} - W^c\frac{\partial K_{ws}}{\partial z} - K_w \ln(W)\frac{\partial c}{\partial z} + K_w\frac{c}{\eta_S}\frac{\partial \eta_S}{\partial z}.$$

Therefore, in the compact form Eq. (6) reads,

$$\frac{\partial \eta}{\partial t} + a\frac{\partial \eta}{\partial z} - \vartheta_{11}\frac{\partial^2 \eta}{\partial z^2} - \vartheta_{12}\frac{\partial^2 T_S}{\partial z^2} = S_3 \tag{7}$$

Analogously, the soil temperature equation reads

$$\frac{\partial T_S}{\partial t} - \frac{\partial}{\partial z}\left(\vartheta_{21}\frac{\partial T_S}{\partial z}\right) - \frac{\partial}{\partial z}\left(\vartheta_{22}\frac{\partial \eta}{\partial z}\right) = S_4 \tag{8}$$

where $S_4 = L_f \rho_{ice}\frac{\partial \eta_{ice}}{\partial t}$ is the source term. Note that we approximate the change of volumetric heat capacity with soil depths ($\partial C/\partial Z$) as constant, when determining the transfer coefficients and source terms from the Eqs. (4) and (6). The error associated with this assumption remains negligibly small even along soil type discontinuities as the volumetric heat capabilities of the various minerally soils only slightly differ.

The quantities η and, T_S over a general discretized element can be approximated as

$$\eta \approx \begin{bmatrix} N_1 & N_2 \end{bmatrix}\begin{pmatrix} \eta_1 \\ \eta_2 \end{pmatrix} = N\eta^a \text{ and } T_S \approx \begin{bmatrix} N_1 & N_2 \end{bmatrix}\begin{pmatrix} T_{S1} \\ T_{S2} \end{pmatrix} = NT_S{}^a$$

where η_1, η_2 and T_{S1}, T_{S2} are the approximated values at nodes of the linear element on the numerical grid, through so-called shape functions N_1 and N_2. The approximated values of η and T_S are shown as η^a and $T_S{}^a$, and the associated source terms of Eqs. (7) and (8) are referred as S_3^a and S_4^a, respectively.

Thus one can discretize Eqs. (7) and (8) as,

$$\frac{\partial}{\partial t}\left(N\eta^{a}\right)+a\frac{\partial}{\partial z}\left(N\eta^{a}\right)-\vartheta_{11}\frac{\partial^{2}}{\partial z^{2}}\left(N\eta^{a}\right)-\vartheta_{12}\frac{\partial^{2}}{\partial z^{2}}\left(N\eta^{a}\right)=S_{3}^{a} \tag{9}$$

and, $$\frac{\partial}{\partial t}\left(NT_{S}^{a}\right)-\vartheta_{21}\frac{\partial^{2}}{\partial z^{2}}\left(NT_{S}^{a}\right)-\vartheta_{22}\frac{\partial^{2}}{\partial z^{2}}\left(NT_{S}^{a}\right)=S_{4}^{a} \tag{10},$$

respectively. Now the specific task is to find appropriate approximations for η^{a} and T_{S}^{a} using a generic FE analysis for Eqs. (9) and (10). This is achieved by multiplying Eqs. (9) and (10) with a test function N^{b} and, integrating over the entire vertical soil column (e.g. Gallagher et al., 1974; Hinton and Owen, 1977; Smith and Griffiths, 1988)

$$\sum_{i=1}^{n}\left(\begin{aligned}&\int_{i}\left(N*\frac{\partial}{\partial t}\left(N\eta^{a}\right)\right)dz+\int_{i}\left(N*a\frac{\partial}{\partial z}\left(N\eta^{a}\right)\right)dz-\int_{i}\left(N*\vartheta_{11}\frac{\partial^{2}}{\partial z^{2}}\left(N\eta^{a}\right)\right)dz\\&\qquad-\int_{i}\left(N*\vartheta_{12}\frac{\partial^{2}}{\partial z^{2}}\left(NT_{S}^{a}\right)\right)dz-\int_{i}\left(N*S_{3}^{a}\right)dz\end{aligned}\right)=\{0\} \tag{11}$$

Where n stands for the total number of grid elements. To obtain the solution for η^{a}, a wide range of approximations exist to postulate the test function N^{b}, for example, collocation, subdomain, least squares and, Galerkin method (e.g. Crandall, 1956). We apply Galerkin method (e.g. Finlayson 1972; Smith and Griffiths, 1988), $N^{b}=\frac{\partial}{\partial\eta^{a}}\left(N\eta^{a}\right)=N$, to solve Eq. (11), i.e., the test function and trial function coincide. Furthermore, the requirement for the order of shape function is reduced by applying Green's theorem, and this yields so called weak formulation. Thus equation (11) written in the Galerkin Weak Finite Element (GWFE) Method reads,

$$\sum_{i=1}^{n}\left(\begin{array}{l}\dfrac{d\eta}{dt}\int_i\left(N*N^T\right)dz+a\int_i\left(N*\dfrac{\partial N^T}{\partial z}\left\{\eta^a\right\}\right)dz+\vartheta_{11}\int_i\left(\dfrac{\partial N}{\partial z}*\dfrac{\partial N^T}{\partial z}\left\{\eta^a\right\}\right)dz\\ \qquad\qquad+\vartheta_{12}\int_i\left(\dfrac{\partial N}{\partial z}*\dfrac{\partial N^T}{\partial z}\left\{T_S^a\right\}\right)dz-\int_i\left(N*N^T\left\{S_3^a\right\}\right)dz\end{array}\right)=\{0\} \tag{12},$$

where N^T is the transpose of the shape functions vector for the vector multiplication purpose over the linear element. By applying the concept of isoparametric elements associated with five-point Gauß-Legendre quadrature integration and by matrix operations (e.g. Hinton and Owen, 1977) one obtains,

$$[M]\frac{d\eta}{dt}+[aC+\vartheta_{11}D]\{\eta^a\}+[\vartheta_{12}D]\{T_S^a\}-[M]\{S_3^a\}=\{0\} \tag{13}$$

Where **M**=$\int_1^n\left(N*N^T\right)dz$, **C**=$\int_1^n\left(N*\dfrac{\partial N^T}{\partial Z}\right)dz$ and, **D**= $\int_1^n\left(\dfrac{\partial N}{\partial Z}*\dfrac{\partial N^T}{\partial Z}\right)dz$ are known as global mass, convection and diffusion matrices (e.g. Donea and Huerta, 2003).

Similarly the GWFE discretization of the soil temperature balance equation (10) can be written as

$$[M]\frac{dT_S}{dt}+[\vartheta_{21}D]\{T_S^a\}+[\vartheta_{22}D]\{\eta^a\}-[M]\{S_4^a\}=\{0\} \tag{14}$$

where, $\eta=N\{\eta^a\}$ and $T_S=N\{T_S^a\}$ are consistent with the generic FE approximation.

Eqs. (13) and (14) represent the spatial GWFE dicretization. The temporal terms $\frac{d\eta}{dt}$ and $\frac{dT_S}{dt}$ are discretized in the framework of the so-called Θ-family methods, in particular using a second order implicit Padé approximation (e.g. Donea and Huerta, 2003), Eqs. (13) and (14) yield

$$[M]\left\{\frac{\eta^{j+1}-\eta^{j}}{\Delta t}\right\} = \Theta\left[\left(-a[C]-\vartheta_{11}[D]\right)\{\eta^{j+1}\}-\vartheta_{12}[D]\{T_S{}^{j+1}\}+[M]\{S_3^{j+1}\}\right]+ \\ (1-\Theta)\left[\left(-a[C]-\vartheta_{11}[D]\right)\{\eta^{j}\}-\vartheta_{12}[D]\{T_S{}^{j}\}+[M]\{S_3^{j}\}\right] \quad (15)$$

and,

$$[M]\left\{\frac{T_S{}^{j+1}-T_S{}^{j}}{\Delta t}\right\} = \Theta\left[\left(-\vartheta_{21}[D]\right)\{T_S{}^{j+1}\}-\vartheta_{22}[D]\{\eta^{j+1}\}+[M]\{S_4^{j+1}\}\right]+ \\ (1-\Theta)\left[\left(-\vartheta_{11}[D]\right)\{T_S{}^{j}\}-\vartheta_{12}[D]\{\eta^{j}\}+[M]\{S_4^{j}\}\right] \quad (16)$$

where Δt is the simulation time step, Θ and $(1-\Theta)$ are the weights given for the present, and past time step spatial GWFE approximations, respectively like in the CNFD scheme. We apply Gauß-Seidel iteration technique for solving the equations (15) and (16), solving them simultaneously for a convergence criterion imposed on soil volumetric water content as 0.0001 m^3/m^3.

2.4 Experimental design

2.4.1) Site and data description

The data sets used in this study are obtained from various sites around Council, Alaska. One of these sites (Hinzmann 2002; 64°50.47' N, 163°38.61' W, and 140 m ASL) is typical for warm permafrost in the tundra regions being formed through the

transitions from boreal forests. Its current vegetation type is tussock tundra on moss. Romonovsky (2005, Personal Communication) provided soil temperature data for two other Council sites, specifically, a warm permafrost and a non permafrost sites. The warm permafrost site is close to Hinzmann's site (64°50.499' N, 163°41.591' W, 56m ASL) and the non-permafrost site is categorized as forest (64°54.456' N, 163°40.469' W, 96m ASL). For brevity, we refer to Hinzmann's datasets of the years 1999, 2000, 2001, 2002 as H99, H00, H01 and H02, and Romonovsky's tundra datasets as R99T, R00T, R01T, and R02T, and the measurements taken at few meters away in the same region as R01TN and R02TN. Analogously, we refer Romonovsky's forest datasets as R01F, R02F for years 2001 and 2002. At the tundra site, the soil vertical profile is moss from surface to 0.12m, dead moss from 0.12 to 0.22m, peat from 0.22 to 0.30m, and silt from 0.30 to 15m. The same soil vertical profile exist at the forest site but soil layer thicknesses from surface to 0.08m, 0.08 to 0.25m, 0.25 to 0.65m, 0.65 to 5m, respectively. The soil physical parameters determined for Council are listed in Tab. 1. We use the same soil vertical profile for Hinzmann's site. For some sites limited soil moisture data are available at different layers than soil temperature. Table 2 summarizes the data availability for the various sites.

2.4.2) Simulations

We perform simulations with HTSVS's soil model alternatively the CNFD and, GWFE for the episodes listed in Tab. 2. In doing so, we drive the soil model with the uppermost and lowermost values of observed soil temperatures as upper and lower boundary conditions, and evaluate the respective scheme's performance comparing the

simulated and observed values between the top and bottom layer. As soil moisture is not consistently recorded, we drive the model with soil saturated volumetric water content (porosity) at the upper and lower most soil layer for all the layers. We initialize soil temperature from interpolated soil temperature observations and soil moisture is set equal to the porosity at each layer. This approach guarantees that both schemes always have the same boundary conditions. Note that permafrost soils are typically saturated or close to saturation. The results of the simulations are addressed by the names of the datasets discussed in section (a).

2.4.3) Analysis

To have equal increments in the numerical grid for well-appropriate FD solution, logarithmic coordinate transformation is applied (e.g. Kramm et al., 1996). The resulting depths are interpolated to the observational depths for comparison, while GEFE is performed on z- coordinates, with no transformation incorporated. Root Mean Square Errors (RMSEs) are calculated to evaluate the discrepancies between the simulated and observed. Since R01TN data is taken at different depths and a few meters away from R01T datasets, these data may serve to examine the effect of spatial soil heterogeneity. The calculations pf the GWFE are performed at the scheme for easy comparison of the schemes. The simulated soil temperature and moisture values are interpolated to the depths of the observations for direct comparison to determine RMSEs. CPU time differences are documented for comparison of the computational burden of the numerical schemes (Tab. 3).

2.5 Results and discussions

2.5.1) General remarks

Generally computational time increases 1.6 to 2.4 times if the GWFE scheme is used instead of the CNFD scheme (see Tab. 3). Despite the different terms in the equations are weighed better using GWFE method, memory requirements, and additional matrix operations such as multiplication, successive elimination of variables to solve the linear system using decomposition of system matrix into upper and lower triangular matrices (known as LU decomposition), and back substitution procedures involving global matrices M, C, and D discussed in section 3.c impose the increased computational burden. Note that the maximum soil layers in our simulations are 11, and in such case we deal with 11X11 global matrices at each time step (60 minutes). However for short term simulations, the additional accuracy in determining the soil state variables and fluxes, with encouraging convergence properties make the method at least attractive.

R99T, R00T, R01F, and R02F are episodes characterized by high Peclet numbers (Fig. 2); while H00, H01 and R01T show very low Peclet numbers.

2.5.2) CNFD Vs. observations

CNFD requires some days for spin-up in the deeper soil layers (e.g. Fig. 5). In the following, results after spin-up are discussed. CNFD captures the changes in the soil temperatures relatively well for the episodes starting in spring (H00,H01, R00T, R02TN, R00F) than in summer when soils are warmer (H99, R99T, H01, R01T, R01TN, R01F, R02F). Note that in spring soil temperatures are still below the freezing point. If the

frozen ground thaws RMSEs are higher than in periods where no thawing of the ground occurs. RMSEs reach up to 2.8K and 1.5K during thawing and else wise, respectively.

As soil ice thaws cell Peclet values increase and as the CNFD-scheme is diffusive soil temperature simulations loose quality around the 0^{o}C-isotherm (Fig. 3a, 4a). However, for the diffusion dominated regimes, i.e. low Peclet values, CNFD produces acceptable results.

As the frozen ground thaws, the results show a phase shift in the peak temperature compared to the observations (Fig. 5). The maximum phase shift found for our sites amounts 5 days. As the thawing of the active layer progresses oscillations may occur along the freezing line. Obviously, the diffusive nature of the scheme triggers alternating thawing and cooling followed by freezing and warming (e.g. Fig. 6).

2.5.3) GWFE Vs. observations

GWFE captures soil temperatures relatively well for H99, H02, R02F. Particularly during the R02F episode, when cell Peclet values are relatively high (Fig. 2), the scheme leads to moderate RMSEs (up to 1.3K) and well captures the temporal evolution of soil temperatures, i.e. the phase of the temperature peaks (e.g. Fig. 3b, 4b). The R01F, R02F episodes have consistently high Peclet value regimes and low RMSEs (Figs. 1, 2). The freezing line is well captured (e.g. Fig. 4b).

The scheme also shows a stable nature when the episodes starts in spring when soil temperatures are below freezing. It does not exhibit excessive diffusion, but when the episode starts in spring with relatively colder temperatures and a quick rise in temperature occurs, particularly in the upper layers beneath the soil of the model, the

scheme overestimates the soil temperature. Nevertheless it still reproduces the peaks in the temperatures maxima and minima correctly (Fig. 6). Quick temperature rises are captured well in the upper layers, but in the lower levels considerable underprediction with slight diffusion is noticed (Fig. 7).

2.5.4) Performance evaluation of CNFD and GWFE

As pointed out above, both CNFD and GWFE simulate the soil temperatures acceptably, at all depths for all episodes tested. However, the main advantages of the GWFE scheme over CNFD are that it (1) captures the right phase for the temperature peaks (e.g. Fig. 5), (2) generate non-diffusive solutions (e.g. Fig. 7), and (3) is able to handle high cell Peclet value regimes relatively well (e.g. Figs. 5, 7). Moreover, GWFE better captures the position and variability of the freezing line than CNFD (e.g. Fig. 4c). On average, the RMSEs are comparably lower for the GWFE than the CNFD scheme, particularly for high Peclet regimes (Fig. 1). All the model soil layers show diffusive flow for the H00 episode (Fig. 2a).

The major disadvantage of GWFE is the much higher computational burden as compared to CNFD. Generally, GWFE seems to overestimate the peaks in diffusion-dominated regimes during the simulation periods (e.g. Fig. 6).

In most cases, soil water content simulated by CNFD and GWFE differ about $0.1 m^3/m^3$ (Fig. 8). The same is true for soil ice content. However, along the freezing line volumetric water content may differ considerably (up to $0.3 m^3/m^3$) when oscillations occur in the CNFD (e.g. Fig. 7). There also exist phase shifts in the onset time of thawing

of up to 10 days. Moreover, the time differs slightly that is needed to complete thawing of a model layer (e.g. Fig. 7).

If in frozen soil at temperatures close to the freezing line, soil temperature increases rapidly, GWFE is able to well capture this behavior, while CNFD scheme produces oscillations. Note that in nature such sudden increases in soil temperature often occur in the upper 15 or 20cm beneath the surface after the insulating snow-pack melts.

While CNFD requires equal grid spacing for well appropriate solution, GWFE show consistent results on any staggered grid. In principle, logarithmic grids like used in HTSVS' soil model are favorable. However, for evaluation studies a free choice of the model layer depths may be desired as it can be easily performed with GWFE.

2.6 Conclusions

Crank-Nicholson finite difference and Galerkin weak finite element schemes are tested with in HTSVS' soil model and evaluated using soil temperature datasets from Council, Alaska. The results obtained by CNFD show excessive diffusion and phase shifts in peak temperatures for moderately advection dominated soil regimes; while those gained by GWFE are still relatively well in phase with the observations even under soil regimes with relatively high Peclet numbers. However, GWFE generally slightly overestimates the peaks under diffusion-dominated soil regimes. The GWFE scheme seems to have no obvious advantage over CNFD for a diffusion dominated regime, in particular, to simulate the soil temperatures in the colder seasons.

Simulations with the GWFE produce up to 1.2 K lower RMSEs than those with CNFD scheme. GWFE better captures the position and variability of the freezing line

than CNFD and therefore is well suitable for soil modeling in Arctic and subarctic regions. The much shorter spin-up time required for GWFE than CNFD makes the former scheme attractive for short-term applications in these regions. The improvement indices indicate that uncertainty in modeling frozen ground can be reduced by GWFE.

Except along the freezing line soil water content simulated by CNFD and GWFE marginally differ. The same is true for soil ice content. Along the freezing line, CNFD and GWFE may differ up to 10 days in the onset thawing. When using CNFD strong increases in soil temperature, e.g. after vanishing of the insulating snow-pack, cause oscillations in simulated soil temperature, water and ice content. During such sudden warming of frozen ground great discontinuities in soil water content and ice content distribution occur that GWFE well captures, while CNFD scheme produces oscillations.

The increase in computational burden associated with GWFE depends on the number of model layers. In our case studies, it ranged between nearly doubling (5 layer) to as much as 8.8 times (11 layers) the CPU-time needed for CNFD. Therefore application of GWFE in climate modeling has to be postponed to the future. However, it should be considered in soil models of regional numerical weather prediction models when used in the subarctic/Arctic regions or in agricultural applications where soil frost may play a role. Here typically the intended simulation episode covers only several days and the increased accuracy and shorter spin-up time of GWFE out-weight the disadvantage of the increased computational burden. The overall RMSEs (averaged over an entire episode and all depths) only differ by 1K. This result suggests that in climate

modeling CNFD will provide acceptable soil temperatures, if seasonal averages are considered.

2.7 Acknowledgements

We thank U. Bhatt, G. Kramm, V.E. Romanovsky and J.E. Walsh for helpful comments and fruitful discussion. We also thank V.E. Romanovsky and L.D. Hinzmann for providing their data. NSF financially supported this study under contract OPP-0327664. Narapusetty was partly financially supported by a University of Alaska Fairbanks graduate school scholarship.

2.8 REFERENCES

Brooks, A. N., and T. J. R. Hughes, 1982: Streamline-upwind/Petrov-Galerkin formulations for convection dominated flows with particular emphasis on incompressible Navier-Stokes equations. *Comput. Meth. Appl. Mech. Eng.,* **32,** 199-259.

Cherkauer, K. A., and D. P. Lettenmaier, 1999: Hydrologic effects of frozen soils in the upper Mississippi River basin. *J. Geophys. Res.,* **104D,** 19611-19621.

Crandall, S. H., 1956: Engineering Analysis. McGraw-Hill, New York.

Dickinson, R.E., A. Henderson-sellers, and P.J. Kennedy, 1993: Biosphere Atmosphere Transfer Scheme (BATS) version 1e as coupled to the NCAR Community Climate Model. NCAR Technical Note, NCAR/TN-378 + STR.

Donea, J., and A. Huerta, 2003: Finite element Methods for Flow Problems. John Wiley & Sons *Ltd*.

Fletcher, C. A. J., 1984: Computational Galerkin Methods. Springer-Verlag New York *Inc.*

Gallagher, R.H., J. T. Oden, C. Taylor, and O.C. Zienkiewicz,1974: Finite elements in Fluids-*Volume 1*.John Wiley & Sons *Ltd.*

Hinton, E., and D. R. J. Owen, 1977: Finite Element Programming. ACADEMIC PRESS *INC.*

Hinzman, L.D., 2002, Climate data for the Arctic Transitions in the Land-Atmosphere System (ATLAS) project. *URL:http://www.uaf.edu/water/projects/atlas.*

Huang, J., H.M. Van Den Dool, and K.P. Georgakakos, 1996: Analysis of Model-Calculated Soil Moisture over the United States(1931-1993) and Applications to Long-Range Temperature Forecasts, *J. Climate*, **9,** 1350-1362.

Hughes, T.J.R., L.P. Franca, and M. Mallet, 1987: A new finite element formulation for computational fluid dynamics: VI. Convergence analysis of the generalized SUPG formulation for linear time-dependent multi-dimensional advective-diffusive systems, *Comp. Methods Appl. Mech. Eng.,* **63**, 173-189.

Hughes, T.J.R., L.P. Franca, and G.M. Hulbert, 1989: A new finite element formulation for computational fluid dynamics: VIII The Galerkin/least squares method for advective-diffusive equations, *Comp. Methods Appl. Mech. Eng.,* **73**, 173-189.

Hughes, T.J.R., and G. M. Hulbert, 1988: Space-time finite element methods for elastodynamics: Formulations and error estimates, *Comp. Methods Appl. Mech. Eng.,* **66**, 339-363.

Jacobson, M. Z., 1999: Fundamentals of atmospheric modeling. Cambridge University Press. New York , pp. 656

Johnson, A., 1987: Numerical solution of partial differential equations by the finite element method. Cambridge University Press.

Kramm, G., 1995: Zum Austauch von Ozon und reaktiven stickstoffverbindungen zwischen Atmospheare und Biosphaere. *Frankfurt, Maraun-Verlag*, p 268.

Kramm, G., N. Beier, T. Foken, H. Müller, P. Schroeder, and W. Seiler, 1996: A SVAT scheme for NO, NO_2, and O_3 – model description. *Meteorol. Atmos. Phys*., **61,** 89-106.

Luo, L., A. Robock, K.Y. Vinnakov, C.A. Schlosser, A.G. Slater, A. Boone, H. Braden, P. Cox, P. De Rosnay, R.E. Dickinson, Y. Dai, Q. Duan, P. Etchevers, A. Henderson-Sellers, N. Gedney, Y.M. Gusev, F. Habets, J. Kim, E. Kowalczyk, K. Mitchell, O.N. Nasonova, J. Nilhan, A.J. Pitman, J. Schaake, A.B. Shmakin, T.G. Smirnova, P. Wetzel, Y. Xue, Z.-L. Yang, and Q.-C. Zeng, 2003: Effects of frozen soil on soil temperature, spring infiltration, and runoff: Results from the PILPS 2(d) experiment at Valdai, Russia. *J. Hydrometeorol*., **4,** 334-351.

McCumber, M.C., and R.A. Pielke, 1981: Simulation of the effects of surface fluxes of heat and moisture in a mesoscale numerical model - Part 1: Soil layer. *J. Geophys. Res.,* **86**, 9929-9938.

Mölders, N., 2000: HTSVS – A new land-surface scheme for MM5. In *The tenth PSU/NCAR Mesoscale model users' workshop*., 33-35 (available from NCAR, P.O. Box 3000, Boulder, CO 80307, USA or http://www.mmm.ucar.edu/mm5/mm5.html)

Mölders, N., U. Haferkorn, J. Döring, and G. Kramm, 2003a: Long-term investigations on the water budget quantities predicted by the hydro-thermodynamic soil vegetation scheme (HTSVS) – Part I: Description of the model and impact of long-wave radiation, roots, snow and soil frost. *Meteorol. Atmos. Phys*., **84,** 15-135.

Mölders, N., U. Haferkorn, J. Döring, and G. Kramm, 2003b: Long-term investigations on the water budget quantities predicted by the hydro-thermodynamic soil vegetation scheme (HTSVS) – Part II: Evaluation, sensitivity, and uncertainty. *Meteorol. Atmos. Phys*., **84,** 137-156.

Mölders, N., and J.E. Walsh, 2004: Atmospheric response to soil frost and snow in Alaska in March. *Theor. Appl. Climatol*., **77,** 77-115.

Montaldo, N., and J.D. Albertson, 2001: On the use of the force-restore SVAT model formulation for stratified soils. *J. Hydrometeor*. **2**, 571-578.

Narapusetty, B., and Mölders, N., 2005: Evaluation of snow depth and soil temperatures predicted by the Hydro Thermodynamic Soil Vegetation Scheme (HTSVS) coupled with the PennState/NCAR Mesoscale Meteorological Model version 5 (MM5). *J. App. Meteorol.* (*in press*)

Oden, J. T., 1972: Finite elements of nonlinear continua. McGraw-Hill, New York

Pielke, R.A., 2001: Influence of the spatial distribution of vegetation and soils on the prediction of cumulus convective rainfall. *Rev. Geophys.,* **39**, 151-177.

Robock, A., Y.V. Konstantin, C.A. Schlosser, A.S. Nina, and X.Yongkang, 1995: Use of midlatitude soil moisture and meteorological observations to validate soil moisture simulations with biosphere and bucket models. *J. Climate,* **8,** 15-35.

Robock, A., K.Y. Vinnikov, and C.A. Schlosser, 1997: Evaluation of land-surface parameterization schemes using observations. *J. Climate*, **10**, 377-379.

Shao, Y.P., and A. Henderson-Sellers, 1996: Validation of soil moisture simulation in land-surface parameterization schemes with HAPEX data. *Global Planetary Change.,* **13,** 11-46.

Shakib, F., 1988: Finite element analysis of the compressible Euler and Navier-Stokes equations. *Ph.D. Thesis*, Stanford University.

Smith I. M., and D. V. Griffiths, 1988: PROGRAMMING THE FINITE ELEMENT METHOD, Second Edition. John Wiley & Sons *Ltd.*

Tezduyar, T.E., 1992: Stabilized Finite Element Formulations for Incompressible Flow Computations, *Adv. in Appl. Mech.*, **28**,1-44.

Wetzel, P.J., and A. Boone, 1995: A parameterization for Land-Atmosphere-Cloud-Exchange (PLACE): Documentation and testing of a detailed process model of the partly cloudy boundary layer over heterogeneous land. *J. Climate,* **8,** 1810-1837.

2.9 Table captions

Table 1. Soil physical parameters used in our study. Here, η_s, b, k_s, ψ_s and $c_S\rho_S$ are the volumetric water content at saturation (porosity), pore-size distribution index, saturated hydraulic conductivity, water potential at saturation, and volumetric heat capacity of the dry soil material.

Table2. Duration of the simulations for different episodes

Table3. CPU time in seconds as obtained with CNFD and GWFEM simulations

2.10 Figure captions

Figure 1. Comparison of simulated and observed soil temperature RMSEs using CNFD and GWFEM as obtained for (a) H99, H00, H01 and H02 in clockwise direction (b) R99T, R00T from top left, R01T, R01TN (grey shade) on the bottom right figure and R02TN on the bottom left (c) R01F and R02F

Figure 2. Averaged cell Peclet values for (a) H99 and H00 (b) R99T, R00T, R01T, and R02T and (c) R01F, R02F

Figure 3. Comparison of simulated and observed soil temperatures for H99 as obtained for (a) CNFD (b) GWFE and (c) differences in CNFD-GWFE

Figure 4. Comparison of simulated and observed soil temperatures for H00 as obtained for (a) CNFD (b) GWFE and (c) differences in CNFD-GWFE

Figure 5. Soil temperatures obtained using CNFD and GWFE for R00T 5^{th} layer.

Figure 6. Soil temperatures obtained using CNFD and GWFE for R01T 3^{rd} layer.

Figure 7. Soil temperatures obtained using CNFD and GWFE for R01TN (a) 3^{rd} layer and (b) 4^{th} layer.

Figure 8. Soil water content (m^3/m^3) as obtained with H99

Soil type	η_s m^3/m^3	b -.-	ψ_s m	k_s 10^{-6} m/s	$c_S\rho_S$ $10^6 Jm^{-3}K^{-1}$
Moss	0.8	10.18	-0.388	1.13	0.851
Peat	0.7075	7.75	-0.356	8.0	0.84
Silt	0.5	2.54	-0.396	2.49	0.97

Table 4. Soil physical parameters used in our study. Here, η_s, b, k_s, ψ_s and $c_S\rho_S$ are the volumetric water content at saturation (porosity), pore-size distribution index, saturated hydraulic conductivity, water potential at saturation, and volumetric heat capacity of the dry soil material. Parameters are from Clapp and Hornberger (1978), Cosby et al. (1984), Pielke (1984), and Chen and Dudhia (2001).

Episodes	Episodes used for simulations	Depths at which soil temperature observations are recorded (in meters)
H99	07/29 to 10/01 (65)	0, 0.05, 0.1, 0.15, 0.25, 0.35, 0.6, 0.85, 1.10
H00	05/14 to 09/23 (133)	0, 0.05, 0.1, 0.15, 0.25, 0.35, 0.6, 0.85, 1.10
H01	04/08 to 07/10 (94)	0, 0.05, 0.1, 0.15, 0.25, 0.35, 0.6, 0.85
H02	08/06 to 12/31 (148)	0, 0.05, 0.1, 0.15, 0.25, 0.4
R99T	07/29 to 10/01 (65)	0.01, 0.04, 0.122, 0.2, 0.276, 0.35, 0.432, 0.506, 0.655, 0.81, 1.015
R00T	05/14 to 09/23 (133)	0.01, 0.04, 0.122, 0.2, 0.276, 0.35, 0.432, 0.506, 0.655, 0.81, 1.015
R01T	04/08 to 08/16 (131)	0.01, 0.04, 0.122, 0.2, 0.276, 0.35, 0.432, 0.506, 0.655, 0.81, 1.015
R01TN	06/01 to 10/07 (129)	0.031, 0.105, 0.187, 0.261, 0.41, 0.565, 0.77
R02TN	08/06 to 12/31 (148)	0.031, 0.105, 0.187, 0.261, 0.41, 0.565, 0.77
R01F	R01FN: 07/19 to 10/07 (81)	0, 0.072, 0.149, 0.226, 0.301, 0.377, 0.453, 0.53, 0.685, 0.834, 1.04
R02F	R02FN: 08/06 to 12/31 (148)	0, 0.072, 0.149, 0.226, 0.301, 0.377, 0.453, 0.53, 0.685, 0.834, 1.04

(a)

Table 5. Duration of the simulations for different episodes along with the information of representative depths of (a) Soil temperature (b) Soil moisture observations

Episodes used for simulations	Depths at which soil moisture observations are recorded (in meters)	Depths at which soil moisture observations are recorded (in meters)
H99	07/29 to 10/01 (65)	0.05, 0.1, 0.15, 0.2, 0.3
H00	05/14 to 09/23 (133)	0.05, 0.1, 0.15, 0.2, 0.3
H01	04/08 to 07/10 (94)	0.05, 0.1, 0.15, 0.2, 0.3
H02	08/06 to 12/31 (148)	0.05, 0.1, 0.15, 0.2
R99T	07/29 to 10/01 (65)	0.15, 0.26, 0.36
R00T	05/14 to 09/23 (133)	0.15, 0.26, 0.36
R01T	04/08 to 08/16 (131)	0.15, 0.26, 0.36
R01TN	06/01 to 10/07 (129)	0.15, 0.26, 0.36
R02TN	08/06 to 12/31 (148)	0.15, 0.26, 0.36
R01F	R01FN: 07/19 to 10/07 (81)	0.15, 0.31, 0.54
R02F	R02FN: 08/06 to 12/31 (148)	0.15, 0.31, 0.54

(b)

Simulation	CPU time in seconds		Increase in CPU requirement	Averaged Improvement Index (RMSE of GWFE to RMSE of CNFD)
	CNFD	GWFE		
H99	54	88	1.6	0.96
H00	50	120	2.4	0.85
H01	73	114	1.6	0.53
H02	72	113	1.6	0.82
R99T	57	97	1.7	0.84
R00T	56	154	2.7	0.43
R01T	89	177	1.9	1.24
R01TN	46	104	2.3	0.77
R02TN	75	148	1.9	1.03
R01F	69	144	2.1	0.82
R02F	83	184	2.2	0.68

Table 6. CPU time in seconds as obtained with CNFD and GWFE simulations

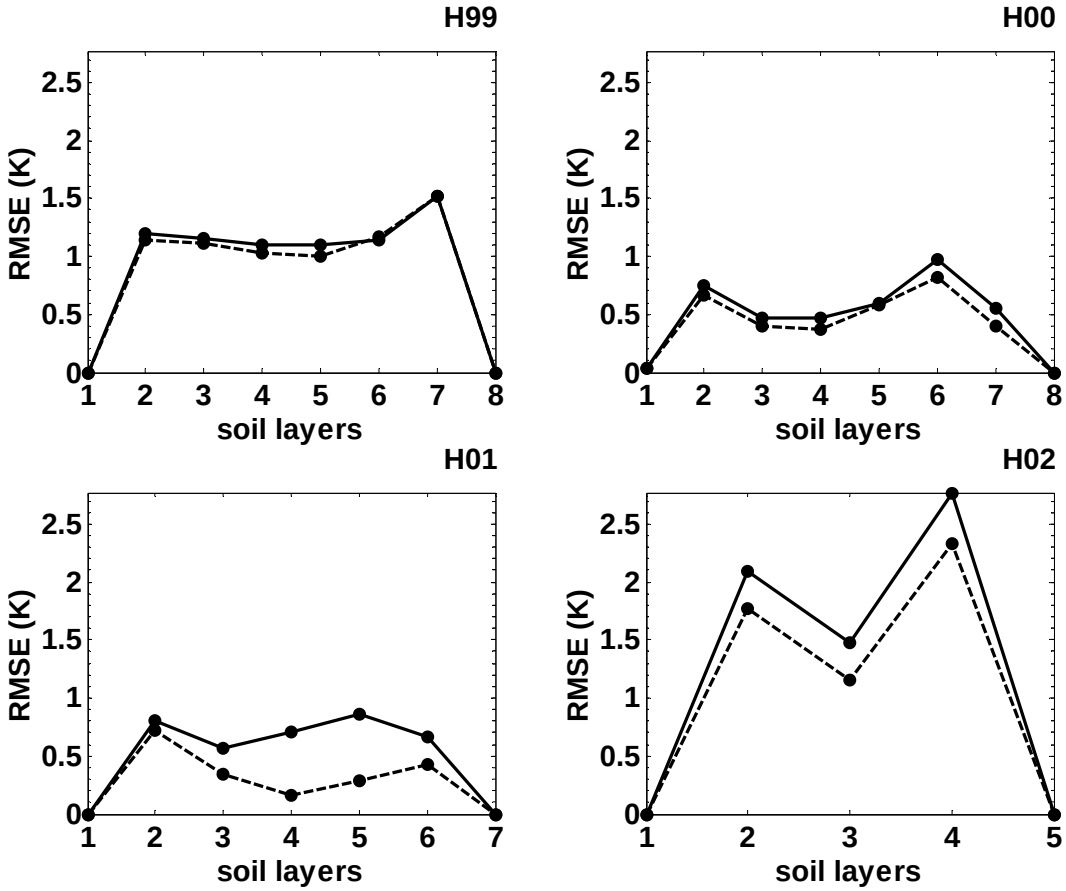

(a)

Figure 13. Comparison of simulated and observed soil temperature RMSEs using CNFD and GWFE schemes as obtained for various sites. The solid line shows the results obtained with CNFD scheme and dashed line indicates the same obtained with GWFE scheme.

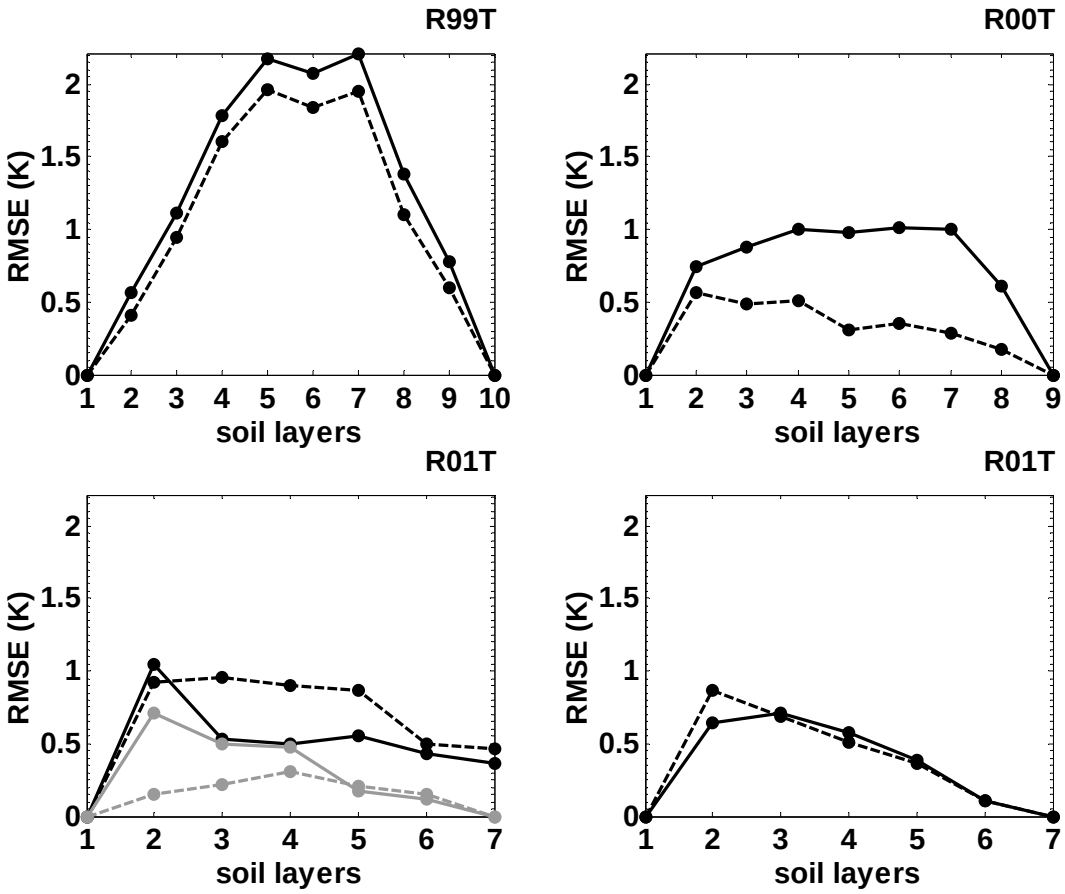
R99T
R00T
R01T
R01T
RMSE (K)
soil layers
0
0.5
1
1.5
2
1 2 3 4 5 6 7 8 9 10
1 2 3 4 5 6 7 8 9
1 2 3 4 5 6 7

(b)

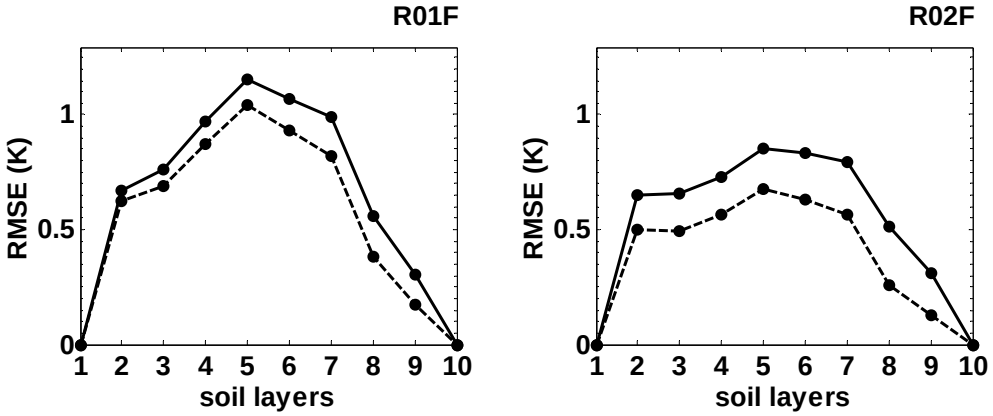

(c)

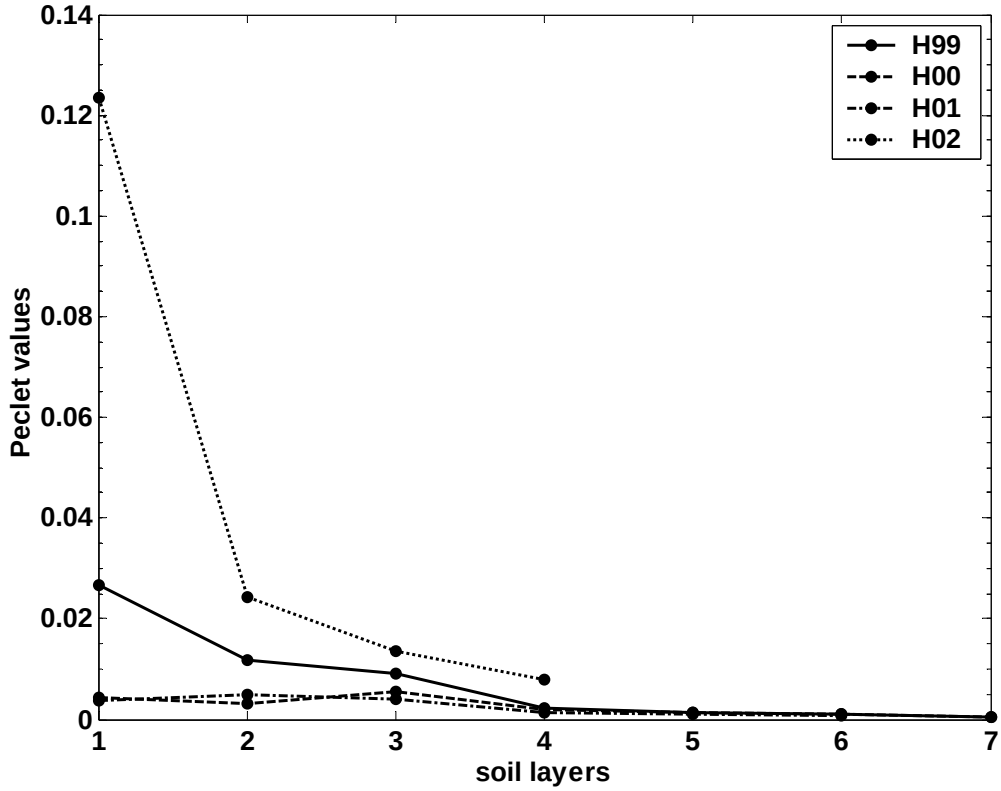

Figure 2. Averaged cell Peclet values for (a) H99 and H00 (b) R99T, R00T, R01T, and R02T and (c) R01F, R02F

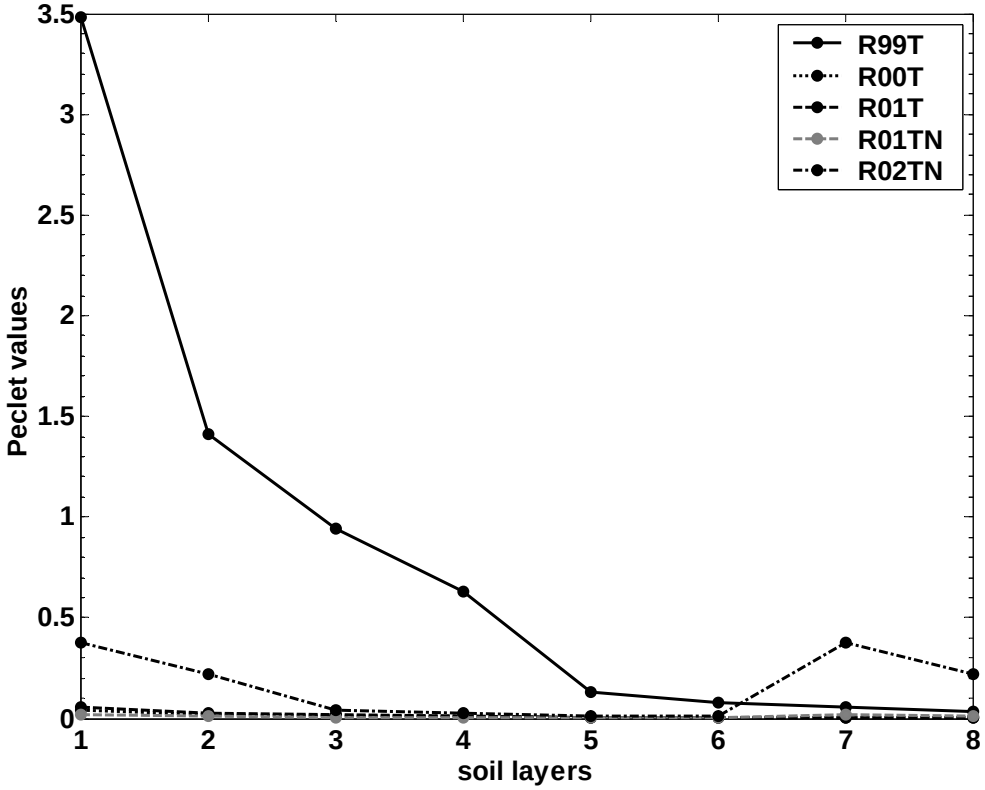
R99T
R00T
R01T
R01TN
R02TN
Peclet values
soil layers
3.5
3
2.5
2
1.5
1
0.5
0
1
2
3
4
5
6
7
8

(b)

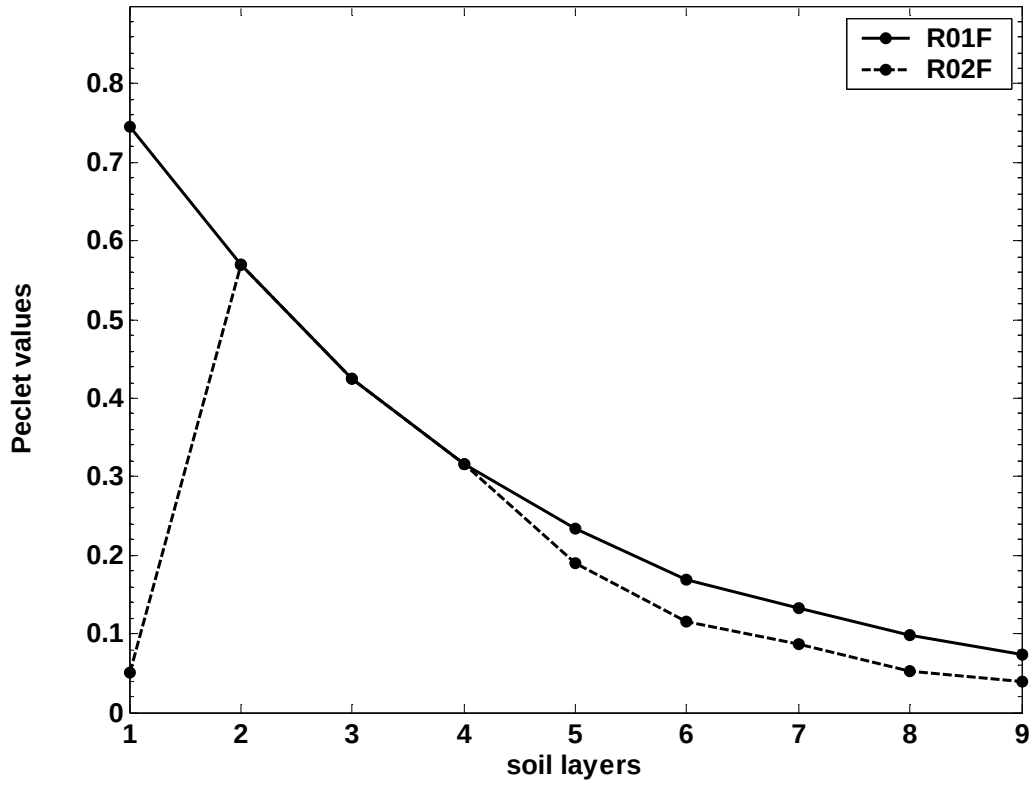
R01F
R02F
Peclet values
soil layers
0
0.1
0.2
0.3
0.4
0.5
0.6
0.7
0.8
1
2
3
4
5
6
7
8
9

(c)

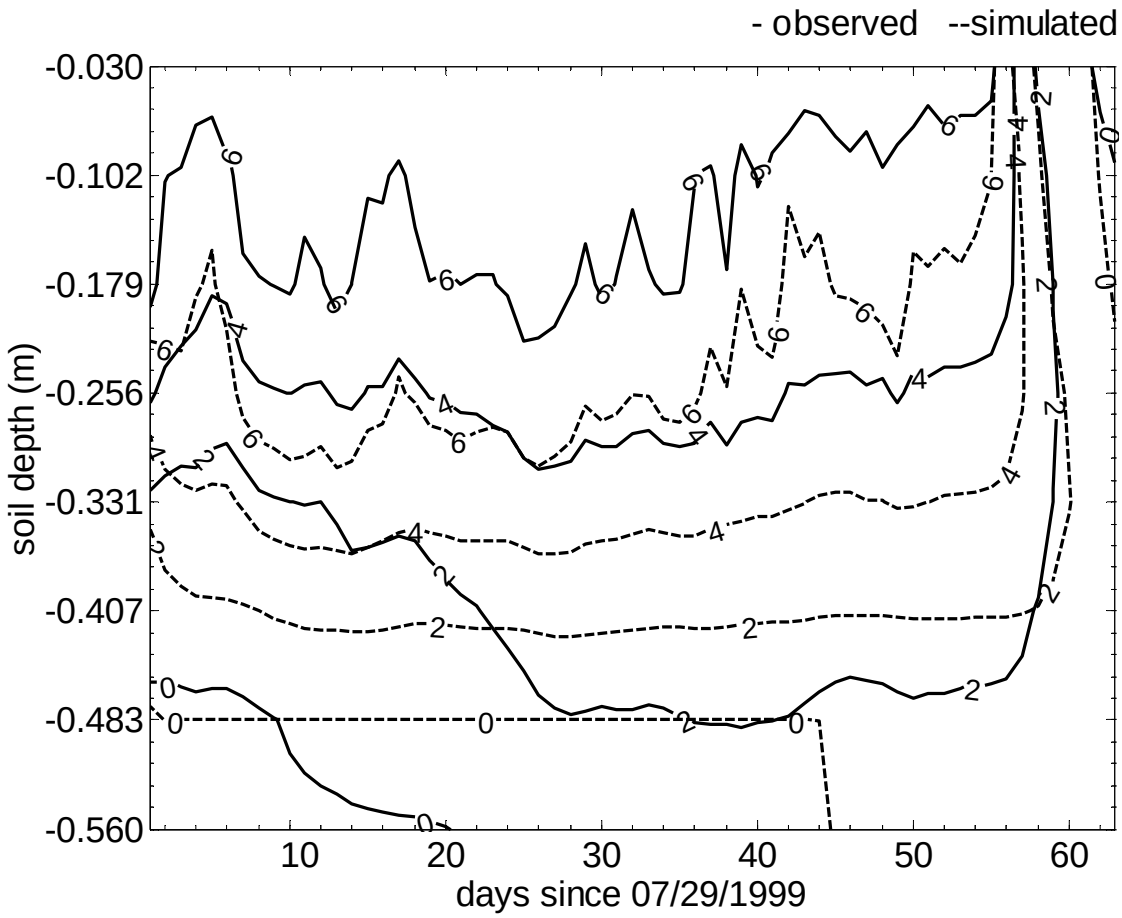

(a)

Figure 3. Comparison of simulated and observed soil temperatures for H99 as obtained for (a) CNFD (b) GWFE and (c) differences in CNFD-GWFE

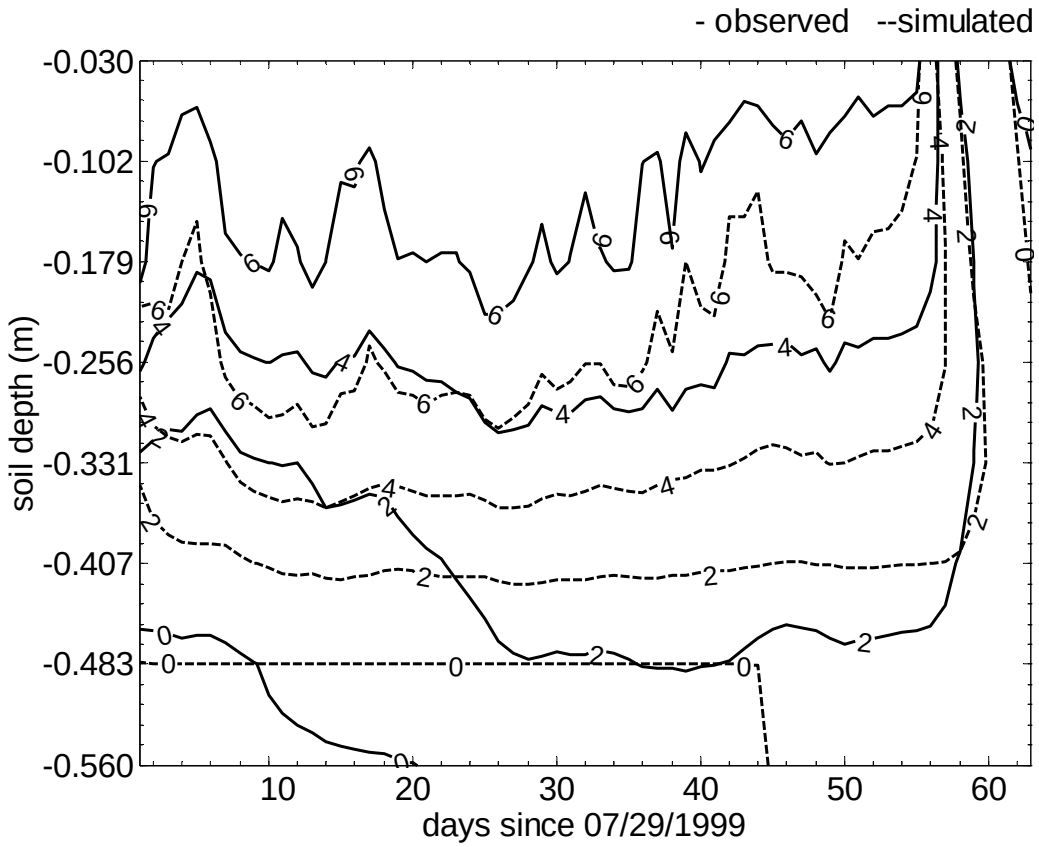
- observed --simulated
soil depth (m)
-0.030
-0.102
-0.179
-0.256
-0.331
-0.407
-0.483
-0.560
10
20
30
40
50
60
days since 07/29/1999

(b)

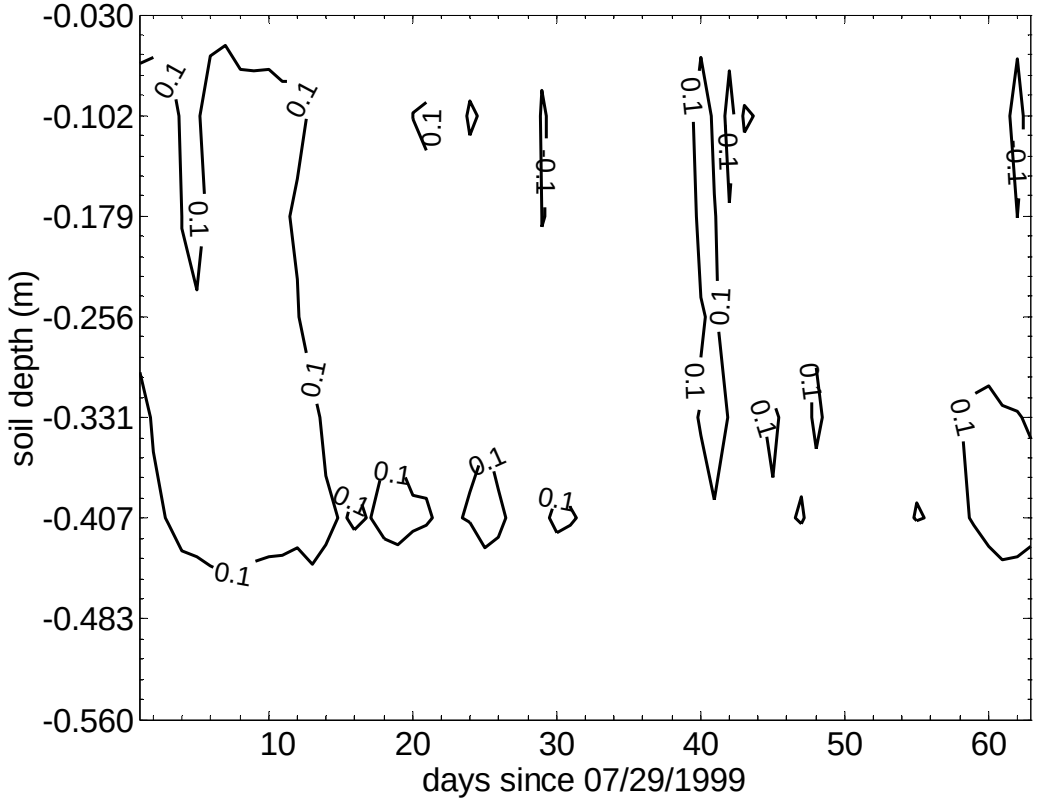
-0.030
-0.102
-0.179
-0.256
-0.331
-0.407
-0.483
-0.560
soil depth (m)
10
20
30
40
50
60
days since 07/29/1999
0.1

(c)

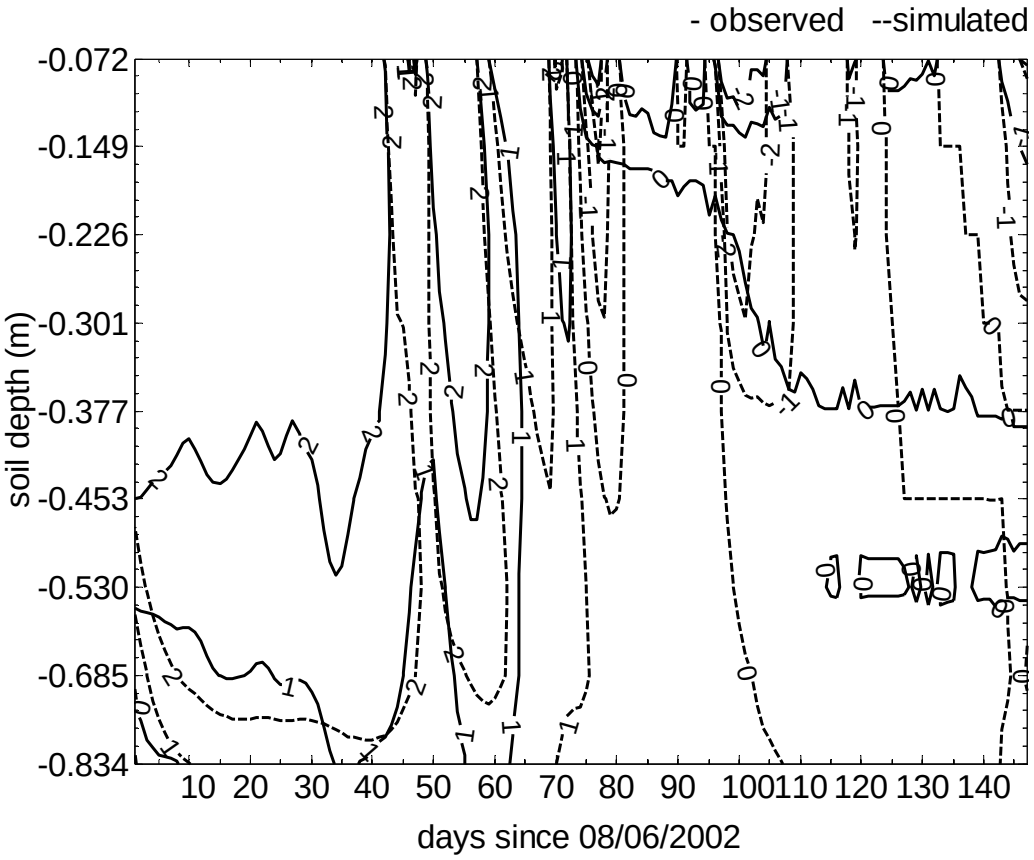

(a)

Figure 4. Comparison of simulated and observed soil temperatures for R02F as obtained for (a) CNFD (b) GWFE and (c) differences in CNFD-GWFE

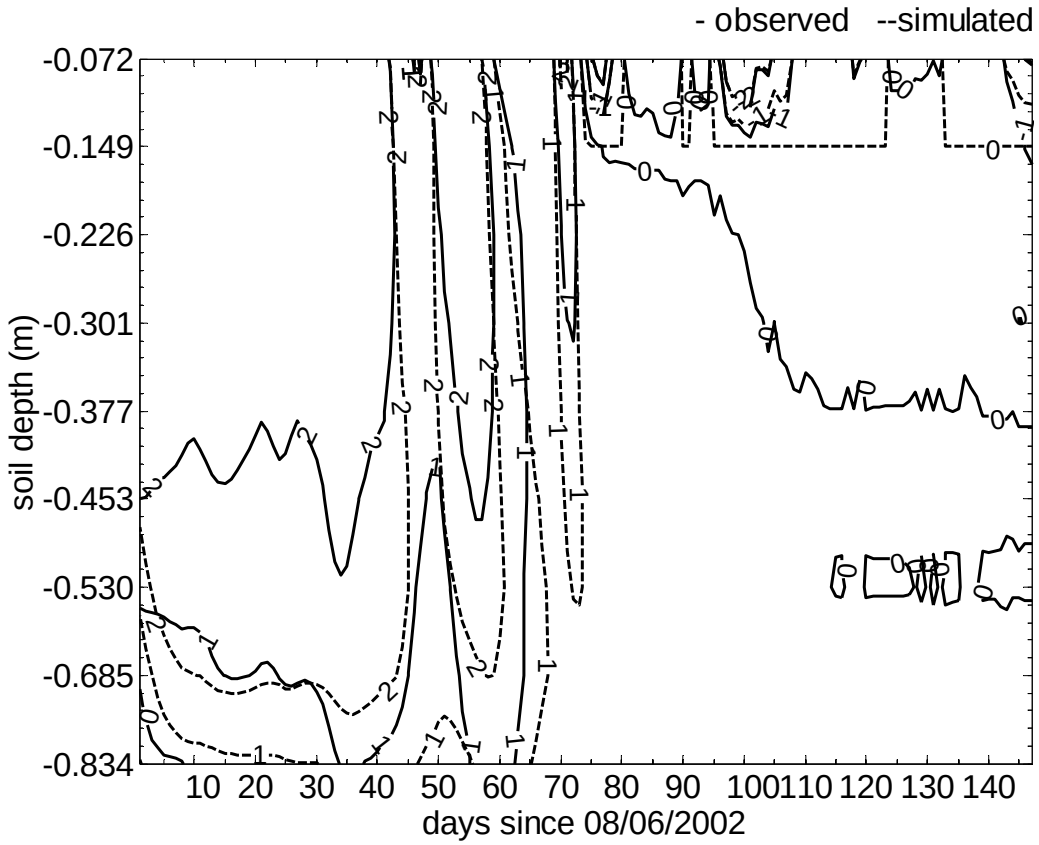
- observed --simulated
soil depth (m)
-0.072
-0.149
-0.226
-0.301
-0.377
-0.453
-0.530
-0.685
-0.834
10 20 30 40 50 60 70 80 90 100 110 120 130 140
days since 08/06/2002

(b)

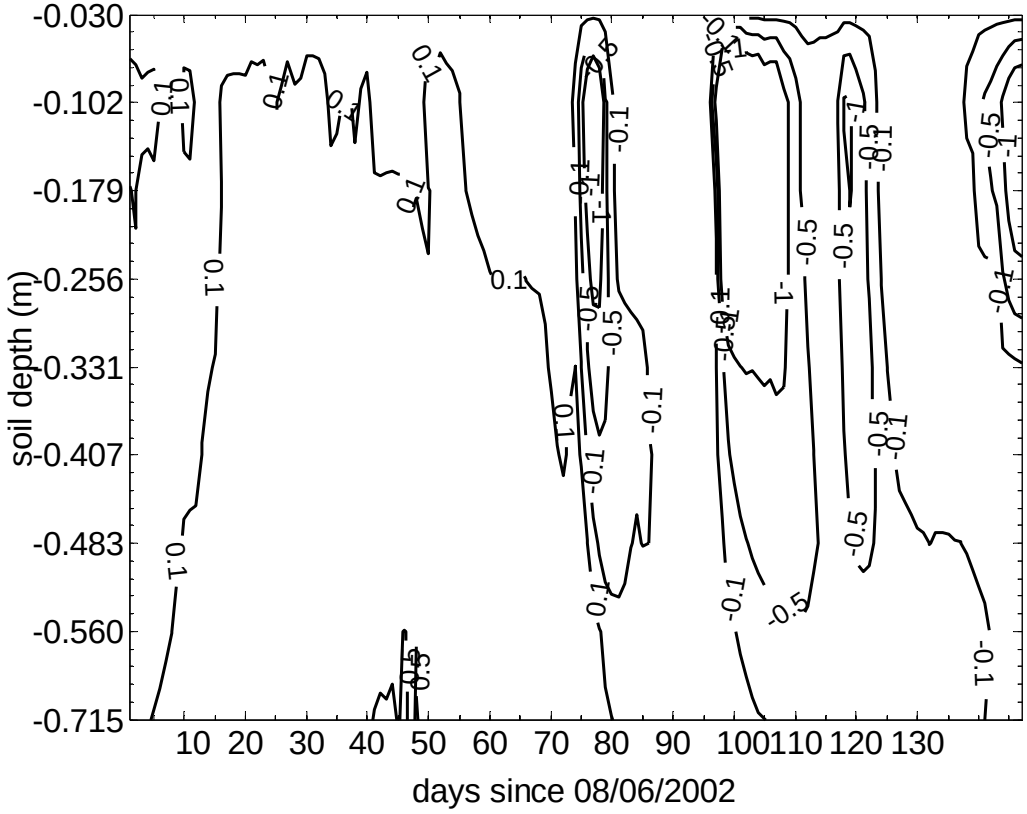
-0.030
-0.102
-0.179
-0.256
-0.331
-0.407
-0.483
-0.560
-0.715
soil depth (m)
10 20 30 40 50 60 70 80 90 100 110 120 130
days since 08/06/2002

(c)

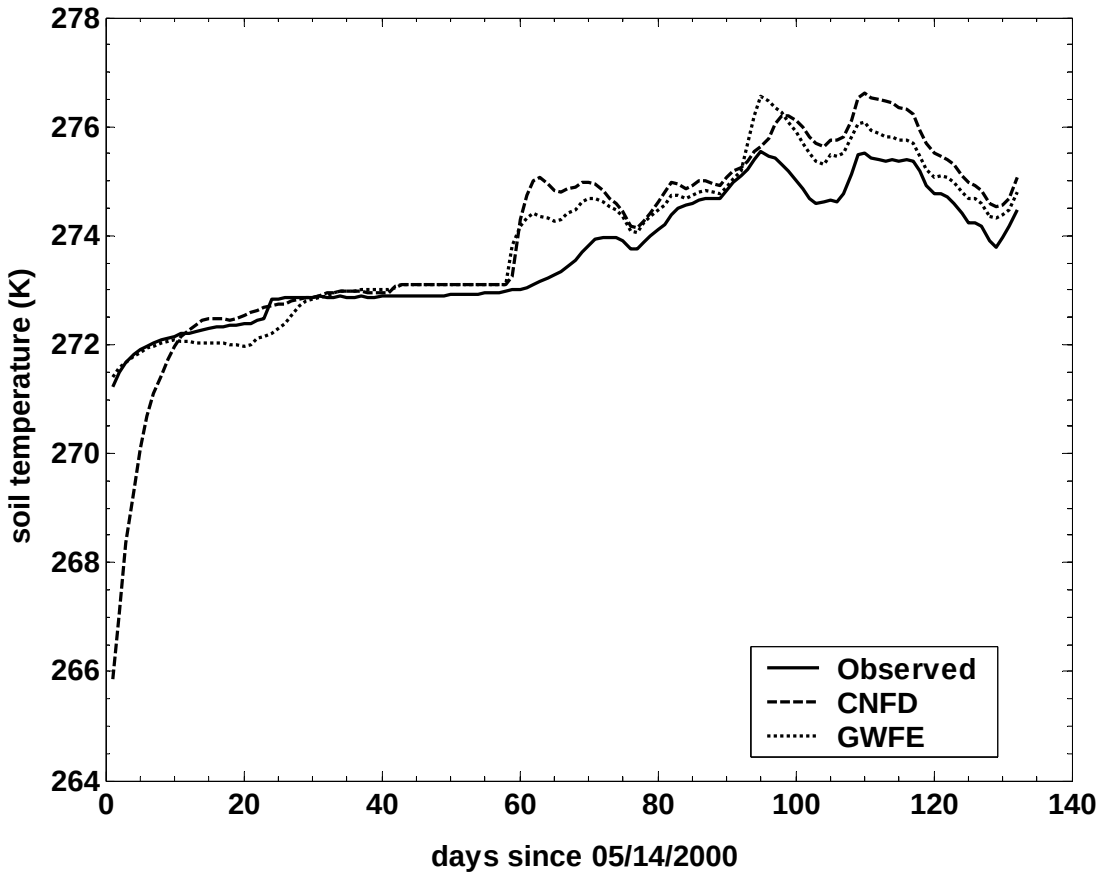

Figure 5. Soil temperatures obtained using CNFD and GWFEM for R00T 5th layer.

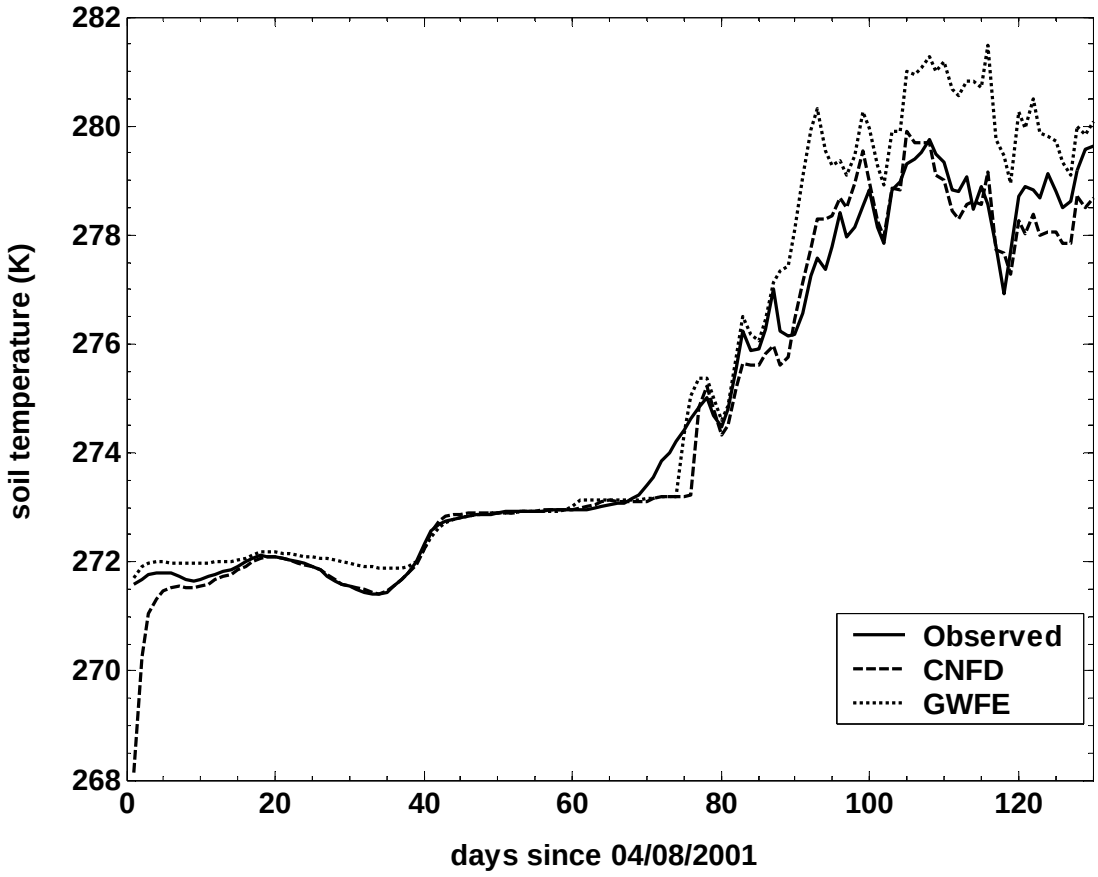

Figure 6. Simulation results for R01T 3rd layer show soil temperatures

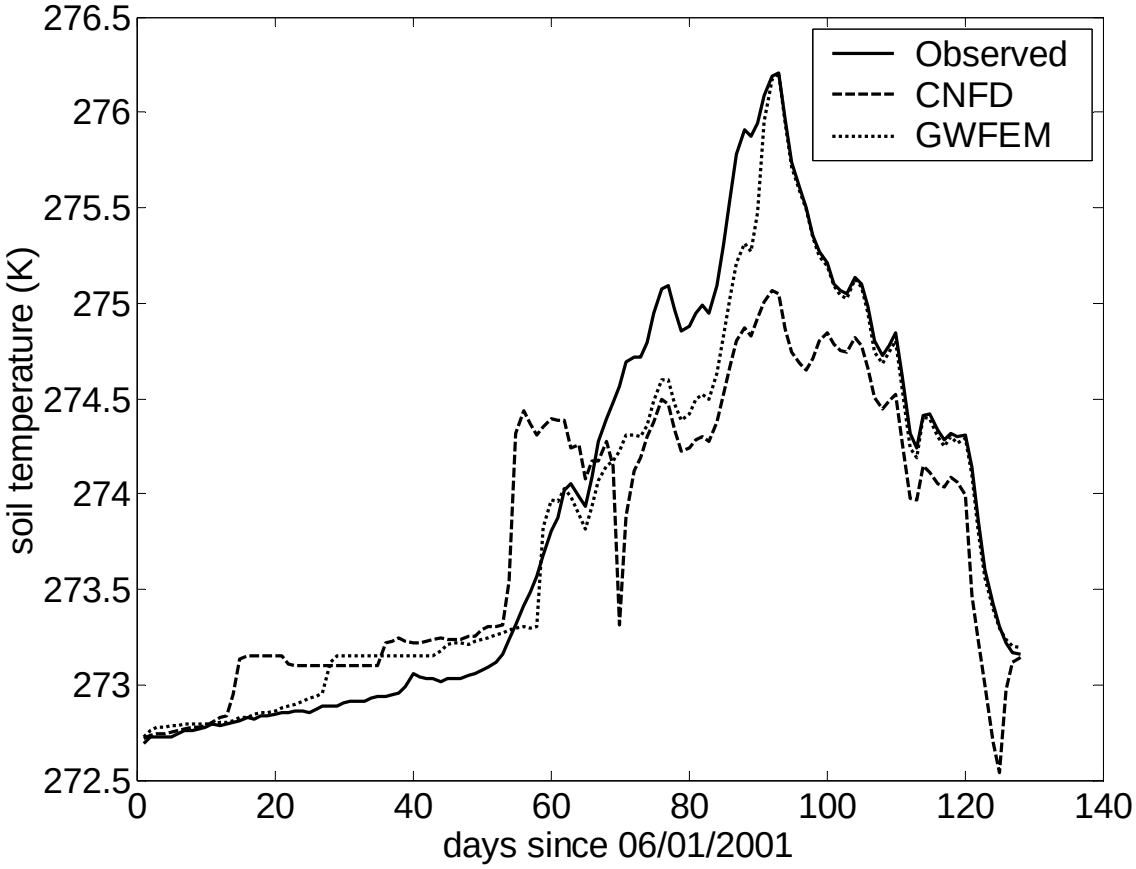

Figure 7. Soil temperatures obtained using CNFD and GWFE for R01TN (a) 3rd layer and (b) 4th layer, and soil moistures obtained using CNFD and GWFE for (c) 3rd layer and (d) 4th layer.

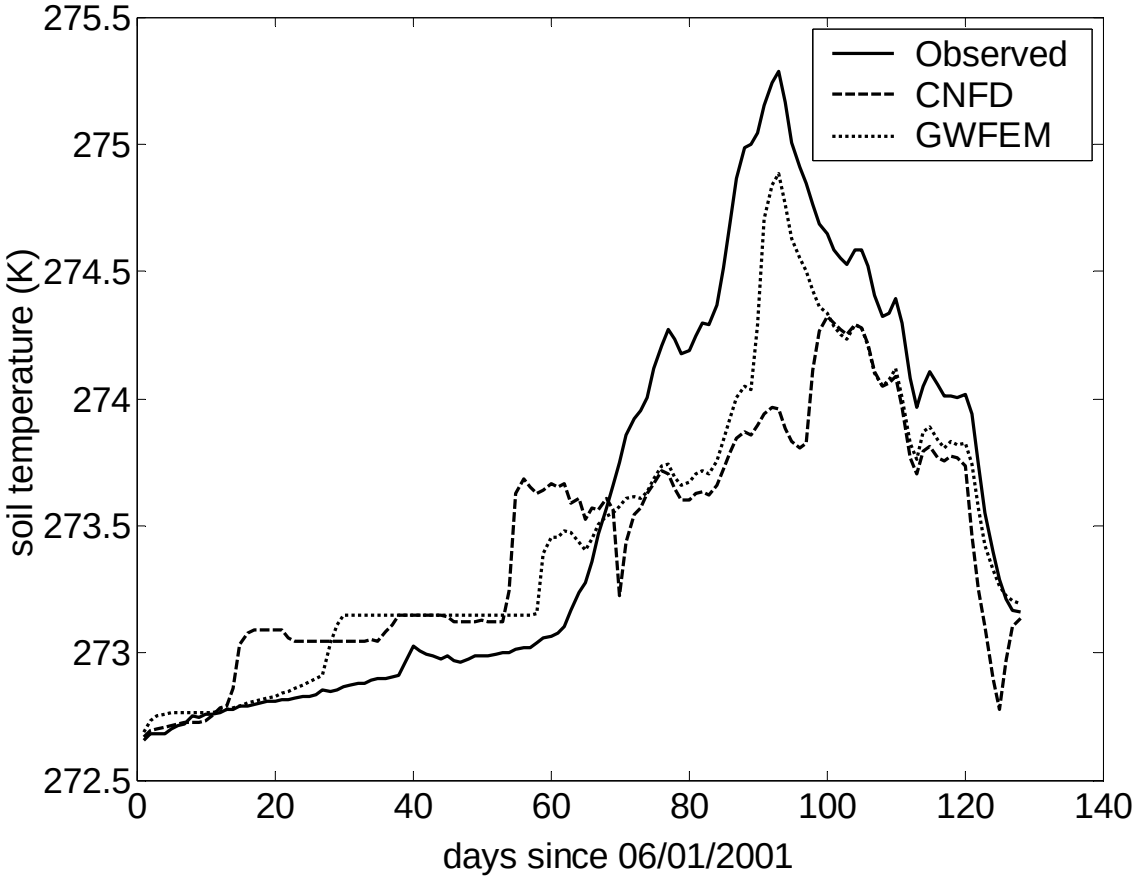
Observed
CNFD
GWFEM
soil temperature (K)
days since 06/01/2001
275.5
275
274.5
274
273.5
273
272.5
0
20
40
60
80
100
120
140

(b)

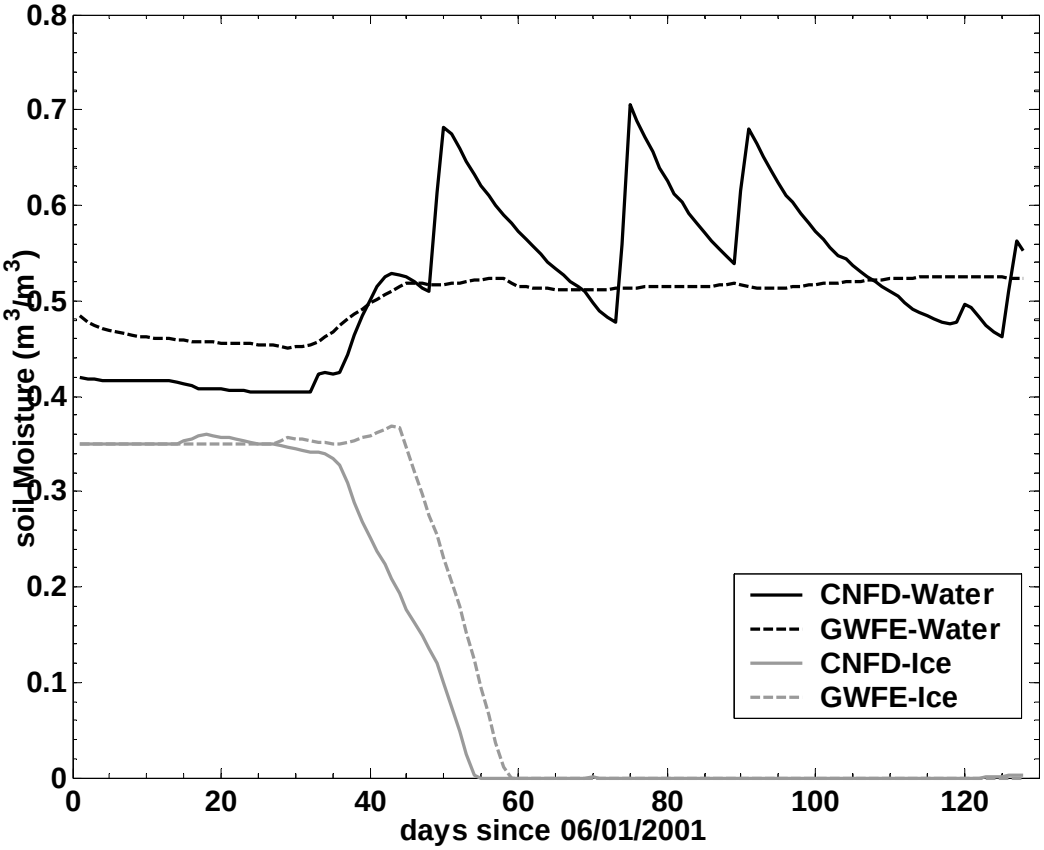
0.8
0.7
0.6
0.5
0.4
0.3
0.2
0.1
0
soil Moisture (m3/m3)
0
20
40
60
80
100
120
days since 06/01/2001
CNFD-Water
GWFE-Water
CNFD-Ice
GWFE-Ice

(c)

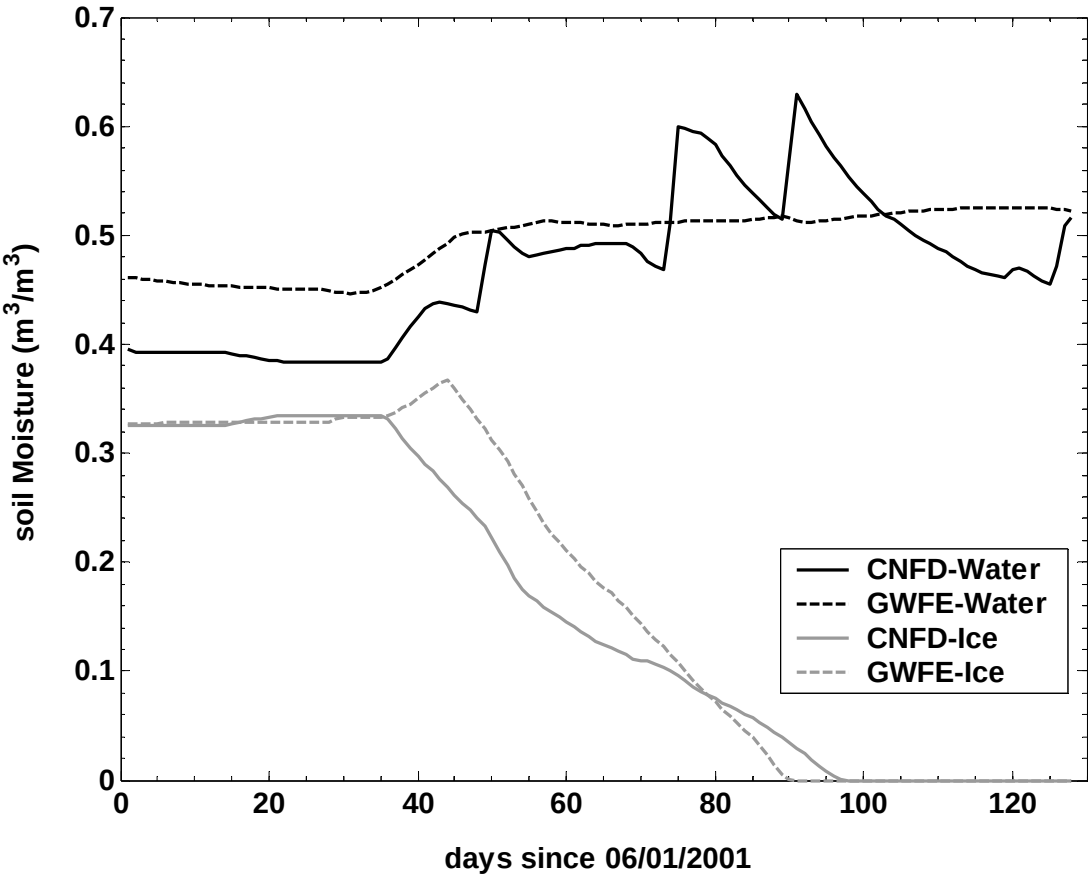
0.7
0.6
0.5
0.4
0.3
0.2
0.1
0
soil Moisture (m3/m3)
0
20
40
60
80
100
120
days since 06/01/2001
CNFD-Water
GWFE-Water
CNFD-Ice
GWFE-Ice

(d)

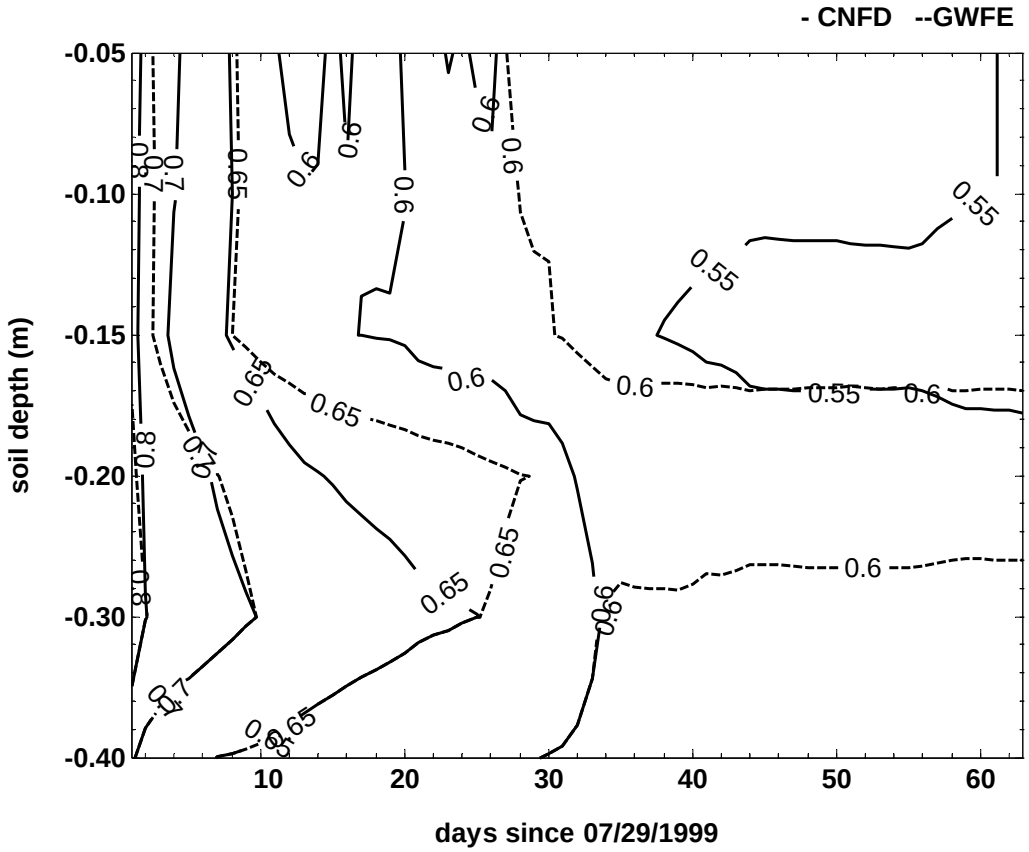

Figure 8. Soil water content (m^3/m^3) as obtained with H99